

Nanosponges for advanced drug delivery

by

Asanka Sajini Yapa

B.Sc. (Hons), University of Colombo, Sri Lanka, 2010

AN ABSTRACT OF A DISSERTATION

submitted in partial fulfillment of the requirements for the degree

DOCTOR OF PHILOSOPHY

Department of Chemistry  
College of Arts and Sciences

KANSAS STATE UNIVERSITY  
Manhattan, Kansas

2017

## Abstract

A novel type of supramolecular aggregate, named “nanosponge” was synthesized through the interaction of novel supramolecular building blocks with trigonal geometry. The cholesterol-(K/D)<sub>n</sub>DEVDGC)<sub>3</sub>-trialeimide unit consists of a trigonal maleimide linker to which homopeptides (either K or D) of variable lengths (n = 5, 10, 15, 20) and a consensus sequence for executioner caspases (DEVDGC) are added via Michael addition. Upon mixing in aqueous buffer, cholesterol-(K)<sub>n</sub>DEVDGC)<sub>3</sub>-trialeimides, as well as a 1:1 mixture of cholesterol-(K/D)<sub>n</sub>DEVDGC)<sub>3</sub>-trialeimides form stable nanosponges, whereas cholesterol-(D)<sub>n</sub>DEVDGC)<sub>3</sub>-trialeimide is unable to form supramolecular aggregates by itself. The structure of the novel nanosponges was revealed through explicit solvent and then coarse-grained molecular dynamics (MD) simulations. The nanosponges are between 80nm and several micrometers in diameters and virtually non-toxic to monocyte/macrophage-like cells.

Furthermore, the structure of novel binary nanosponges consisting of cholesterol-(K/D)<sub>n</sub>DEVDGC)<sub>3</sub>-trialeimide units possessing a trigonal maleimide linker, to which either lysine (K)<sub>20</sub> or aspartic acid (D)<sub>20</sub> are tethered, has been elucidated by means of TEM. A high degree of agreement between these findings and structure predictions through explicit solvent and then coarse-grained molecular dynamics (MD) simulations has been found. Based on the nanosponges' structure and dynamics, caspase-6 mediated release of the model drug 5(6)-carboxyfluorescein has been demonstrated. Moreover, the binary (DK20) nanosponges have been found virtually non-toxic in cultures of neural progenitor cells. Additionally, DK20 nanosponges were taken up efficiently by leucocytes (WBC) in peripheral blood within 3h of exposure. The percentage of live cells among the WBC was not significantly decreased by the

DK20 nanosponges. Therefore, this novel material holds great promise for improved cell-mediated therapy.

Two different nanosponges loaded with the anticancer agent perillyl alcohol (POH) were developed to test the suitability of nanosponges for cell-based cancer therapy. Drug-loaded nanoshuttles featuring trigonal supramolecular building blocks, type (D-POH)<sub>10</sub>K<sub>20</sub> and (D-POH)<sub>10</sub>R<sub>20</sub> were synthesized, purified, and characterized by Dynamic Light Scattering (DLS) and Atomic Force Microscopy (AFM). They were then tested in cell cultures of murine glioma cells (GL26) and murine neural progenitor cells (NPC). The two nanosponges exhibited significantly different biophysical properties (size distribution and zeta potentials). Consequently, different efficacies in killing GL26 and NPC were observed in both, serum free and serum containing culture media. The results from these experiments confirmed that type (D-POH)<sub>10</sub>K<sub>20</sub> nanosponge is an excellent candidate for the cytototherapy of glioblastoma.

Nanosponges for advanced drug delivery

by

Asanka Sajini Yapa

B.Sc. (Hons), University of Colombo, Sri Lanka, 2010

A DISSERTATION

submitted in partial fulfillment of the requirements for the degree

DOCTOR OF PHILOSOPHY

Department of Chemistry  
College of Arts and Sciences

KANSAS STATE UNIVERSITY  
Manhattan, Kansas

2017

Approved by:

Major Professor  
Prof. Stefan H. Bossmann

# **Copyright**

© Asanka Sajini Yapa 2017.

## Abstract

A novel type of supramolecular aggregate, named “nanosponge” was synthesized through the interaction of novel supramolecular building blocks with trigonal geometry. The cholesterol-(K/D)<sub>n</sub>DEVDGC)<sub>3</sub>-trialeimide unit consists of a trigonal maleimide linker to which homopeptides (either K or D) of variable lengths (n = 5, 10, 15, 20) and a consensus sequence for executioner caspases (DEVDGC) are added via Michael addition. Upon mixing in aqueous buffer, cholesterol-(K)<sub>n</sub>DEVDGC)<sub>3</sub>-trialeimides, as well as a 1:1 mixture of cholesterol-(K/D)<sub>n</sub>DEVDGC)<sub>3</sub>-trialeimides form stable nanosponges, whereas cholesterol-(D)<sub>n</sub>DEVDGC)<sub>3</sub>-trialeimide is unable to form supramolecular aggregates by itself. The structure of the novel nanosponges was revealed through explicit solvent and then coarse-grained molecular dynamics (MD) simulations. The nanosponges are between 80nm and several micrometers in diameters and virtually non-toxic to monocyte/macrophage-like cells.

Furthermore, the structure of novel binary nanosponges consisting of cholesterol-(K/D)<sub>n</sub>DEVDGC)<sub>3</sub>-trialeimide units possessing a trigonal maleimide linker, to which either lysine (K)<sub>20</sub> or aspartic acid (D)<sub>20</sub> are tethered, has been elucidated by means of TEM. A high degree of agreement between these findings and structure predictions through explicit solvent and then coarse-grained molecular dynamics (MD) simulations has been found. Based on the nanosponges' structure and dynamics, caspase-6 mediated release of the model drug 5(6)-carboxyfluorescein has been demonstrated. Moreover, the binary (DK20) nanosponges have been found virtually non-toxic in cultures of neural progenitor cells. Additionally, DK20 nanosponges were taken up efficiently by leucocytes (WBC) in peripheral blood within 3h of exposure. The percentage of live cells among the WBC was not significantly decreased by the

DK20 nanosponges. Therefore, this novel material holds great promise for improved cell-mediated therapy.

Two different nanosponges loaded with the anticancer agent perillyl alcohol (POH) were developed to test the suitability of nanosponges for cell-based cancer therapy. Drug-loaded nanoshuttles featuring trigonal supramolecular building blocks, type (D-POH)<sub>10</sub>K<sub>20</sub> and (D-POH)<sub>10</sub>R<sub>20</sub> were synthesized, purified, and characterized by Dynamic Light Scattering (DLS) and Atomic Force Microscopy (AFM). They were then tested in cell cultures of murine glioma cells (GL26) and murine neural progenitor cells (NPC). The two nanosponges exhibited significantly different biophysical properties (size distribution and zeta potentials). Consequently, different efficacies in killing GL26 and NPC were observed in both, serum free and serum containing culture media. The results from these experiments confirmed that type (D-POH)<sub>10</sub>K<sub>20</sub> nanosponge is an excellent candidate for the cytototherapy of glioblastoma.

# Table of Contents

List of Figures .....	xi
List of Tables .....	xvi
Acknowledgements .....	xvii
Dedication .....	xviii
Chapter 1 - Rationally Designed Peptide Nanosponges for Cell-Based Cancer Therapy .....	1
1.1 Abstract .....	1
1.2 Background .....	2
1.2.1 Classic Liposomes and Peptide Vesicles .....	2
1.2.2 The EPR Effect Works Well in Mice, but Not in Humans .....	3
1.2.3 Peptide Nanosponges .....	4
1.3 Methods .....	6
1.3.1 Trimaleinimide Scaffold Synthesis .....	6
1.3.2 Peptide Synthesis .....	6
1.3.3 Cholesterol-Peptide-Trimaleimide Adduct Formation .....	7
1.3.4 Nanosponge Formation and DLS Characterization .....	7
1.3.5 AFM Characterization .....	8
1.3.6 TEM Characterization .....	8
1.3.7 Force Field Calculations .....	9
1.3.8 Entrapment of PKH26 within Peptide Nanosponges .....	10
1.3.9 Cell Experiments and MTT Assays .....	11
1.4 Results .....	12
1.4.1 DLS Characterization of the Nanosponges .....	12
1.4.2 CMC of the Nanosponges .....	13
1.4.3 AFM Characterization .....	15
1.4.4 TEM Characterization .....	16
1.4.5 Force Field Calculations .....	16
1.4.5.1 Force Fields .....	17
1.4.6 Uptake of PKH26-containing Nanosponges by RAW264.7 Cells .....	20
1.4.7. Cell Toxicity of the Peptide Nanosponges .....	21

1.5 Discussion.....	23
1.6 Summary.....	25
1.7 References.....	26
Chapter 2 - Peptide Nanosponges Designed for Rapid Uptake by Stem Cells and Leukocytes ..	31
2.1 Abstract.....	31
2.2 Background.....	32
2.3 Methods .....	36
2.3.1 Synthesis and Characterization of the Nanosponges .....	36
2.3.2 TEM Characterization.....	36
2.3.3 Nanosponge Formation and DLS Characterization .....	36
2.3.4 Carboxyfluorescein Encapsulation .....	37
2.3.5 Caspase-6 Triggered Dye Release .....	38
2.3.6 Cell Experiments and MTT Assays .....	38
2.3.7 Cell Uptake from Peripheral Blood .....	39
2.4 Results.....	41
2.4.1 TEM-Analysis of the Nanosponge Structure.....	41
2.4.2 Caspase-6 Triggered Carboxyfluorescein Release .....	42
2.4.3 TEM-Analysis of Caspase-6 Activation .....	44
2.4.4 Cell Toxicity of the Peptide Nanosponges.....	46
2.4.5 Nanosponge-Uptake Kinetics by Leucocytes in Peripheral Blood.....	47
2.5 Discussion.....	50
2.6 Summary.....	52
2.7 References.....	53
Chapter 3 - Peptide Nanosponges Designed for the Cytotherapy of Gliomas.....	58
3.1 Abstract.....	58
3.2 Background.....	59
3.2.1 Nanosponge-based Delivery Platforms for Perillyl Alcohol (POH).....	64
3.3 Methods .....	67
3.3.1 Materials .....	67
3.3.2 Peptide Synthesis and Biotin Coupling.....	67

3.3.3 Synthesis of Type D <sub>10</sub> K <sub>20</sub> and D <sub>10</sub> R <sub>20</sub> Nanosponges via Michael Addition of D <sub>10</sub> K <sub>20</sub> DEVDGC or D <sub>10</sub> R <sub>20</sub> DEVDGC to Trimaleimide .....	68
3.3.4 Perillyl Alcohol Loading to (Biotin-D <sub>10</sub> K <sub>20</sub> DEVDGC) <sub>3</sub> -trimaleimide.....	68
3.3.5 Perillyl Alcohol Loading to (Biotin-D <sub>10</sub> R <sub>20</sub> DEVDGC) <sub>3</sub> -trimaleimide .....	68
3.3.6 Nanosponge Formation and DLS Characterization .....	69
3.3.7 AFM Characterization .....	69
3.3.8 Cell Experiments and MTT Assays .....	70
3.4 Results.....	72
3.4.1 DLS Characterization of the Nanosponges.....	72
3.4.2 Atomic Force Microscopy of Type (D-POH) <sub>10</sub> K <sub>20</sub> and type (D-POH) <sub>10</sub> R <sub>20</sub> Nanosponges .....	75
3.4.3 Cell Experiments and MTT Assays .....	76
3.5 Discussion.....	83
3.6 Summary.....	86
3.7 References.....	87
Appendix A - For Chapter 1 .....	92
Appendix B - For Chapter 2.....	107
Appendix C - For Chapter 3.....	109
References.....	123

## List of Figures

Figure 1.1 Tri-maleimide based peptide structures: components for the spontaneous formation of nanosponges. A: lysine-based materials, n = 5, 10, 15, 20; B: aspartic acid-based materials, n = 5, 10, 15, 20 .....	5
Figure 1.2 Correlation curves (C(t)) of dynamic light scattering measurements of cholesterol-(D) <sub>20</sub> DEV DGC) <sub>3</sub> -trimaleimide (D), cholesterol-(K) <sub>20</sub> DEV DGC) <sub>3</sub> -trimaleimide (K), and mixture (1/1 molar ratio) of both nanosponge components (DK). .....	14
Figure 1.3 AFM (amplitude, phase, and 3D) images of type DK15 and type DK20 nanosponges. ....	15
Figure 1.4 A: TEM image of type DK20 nanosponges on graphite with uranyl acetate as positive staining. B: Histogram of the size distribution of the larger nanosponges, obtained by using Image J .....	16
Figure 1.5 A: Final structures obtained from the AA (top) and CG (bottom) simulations of cholesterol-(D) <sub>20</sub> DEV DGC (left) and cholesterol-(K) <sub>20</sub> DEV DGC (right). B: Initial and final (4μs) structures obtained from the CG simulation of (cholesterol-(K) <sub>20</sub> DEV DGC) <sub>3</sub> -trimaleimide and (cholesterol-(D) <sub>20</sub> DEV DGC) <sub>3</sub> -trimaleimide. ....	18
Figure 1.6 Expanded view of the final structure obtained from the CG MD simulations.....	20
Figure 1.7 A: RAW264.7 cells (control); B: RAW264.7 cells after 2h of incubation with 50 μM of PKH26-containing type DK nanosponges; C: Fluorescence microscopy of RAW264.7 cells featuring PKH26-containing nanosponges 72h after uptake (DAPI counterstain). ....	21
Figure 1.8 Cell viability of RAW264.7 cells as a function of type DK20 nanosponge concentration and incubation time (24h and 48h), as measured by the MTT assay.....	22
Figure 2.1 Principles of cell therapy utilizing nanosponges.....	33
Figure 2.2 Typical structure of a nanosponge according to molecular dynamics (MD) simulations.....	34
Figure 2.3 A: TEM image of type DK20 nanosponges on HOPG, as deposited from PBS solution. A: Bright field transmission TEM (200 kV) of a type DK 20 nanosponge. B: Same image as in 4A after black/white correction filter function in Photoshop. ....	42
Figure 2.4 Caspase-6 triggered carboxyfluorescein (CF) release.....	43

Figure 2.5 Bright field TEM (200 kV) of 0.20 mg/mL of carboxyfluorescein-loaded DK20 nanosponges: A: Nanosponges deposited from PBS before adding caspase-6. B: Reactive mixture deposited from PBS containing caspase-6 ( $2.60 \times 10^{-10}$ M) after 15 min. of reaction at 37°C. C: Novel nanostructures, which were formed in the reaction, deposited from PBS containing caspase-6 ( $2.60 \times 10^{-10}$ M) after 60 min. of reaction at 37°C.....	44
Figure 2.6 Size distribution of carboxyfluorescein-loaded DK20 nanosponges before and after “digestion” with caspase-6.....	46
Figure 2.7 Cell viability of C17.2 neural progenitor cells (NPCs) as a function of DK20 nanosponge concentration and incubation time (24h and 48h), as measured by the MTT assay.....	47
Figure 2.8 Uptake efficacy of type DK20 nanosponges by leukocytes (mainly neutrophils and monocytes/macrophages) and granulocytes in peripheral blood as function of incubation time. ....	48
Figure 2.9 Survival of WBC when exposed to DK20 peptide nanosponges, compared to the survival of an unexposed WBC control group.....	49
Figure 3.1 Mevalonate/cholesterol pathway.....	62
Figure 3.2 Chemical structures of nanosponge types $D(\text{POH})_{10}\text{K}_{20}$ and $D(\text{POH})_{10}\text{R}_{20}$ . ....	65
Figure 3.3 Correlation curves ( $C(\tau)$ ) of dynamic light scattering measurements of (Biotin- $D_{10}(\text{Perillyl alcohol})_{10}\text{K}_{20}\text{DEV DGC})_3$ -trimaleimide nanosponges (type $(D\text{-POH})_{10}\text{K}_{20}$ ) and (Biotin- $D_{10}(\text{Perillyl alcohol})_{10}\text{R}_{20}\text{DEV DGC})_3$ -trimaleimide nanosponges (type $(D\text{-POH})_{10}\text{R}_{20}$ ) in deoxygenated PBS buffer below and above their CMC. ....	74
Figure 3.4 Average hydrodynamic diameters, as measured by DLS, as a function of type $(D\text{-POH})_{10}\text{K}_{20}$ and type $(D\text{-POH})_{10}\text{R}_{20}$ nanosponge concentrations. ....	75
Figure 3.5 AFM images (tapping mode) of $(D\text{-POH})_{10}\text{K}_{20}$ and $(D\text{-POH})_{10}\text{R}_{20}$ nanosponges (0.050 M of each nanosponge in PBS mM) on MICA. ....	76
Figure 3.6 Cell viabilities of neural progenitor cells (NPC) and murine glioma cells (GL26) as a function of the concentration of type $(D\text{-POH})_{10}\text{K}_{20}$ and $(D\text{-POH})_{10}\text{R}_{20}$ nanosponge in serum free medium after 24h of exposure.. ....	78
Figure 3.7 Cell viabilities of neural progenitor cells (NPC) and murine glioma cells (GL26) as a function of the concentration of type $(D\text{-POH})_{10}\text{K}_{20}$ and $(D\text{-POH})_{10}\text{R}_{20}$ nanosponge in serum free medium after 48h of exposure.. ....	79

Figure 3.8 Cell viabilities of neural progenitor cells (NPC) and murine glioma cells (GL26) as a function of the concentration of type (D-POH) <sub>10</sub> K <sub>20</sub> and (D-POH) <sub>10</sub> R <sub>20</sub> nanosponge in serum-containing medium (10% FBS, 5% horse serum) after 24h of exposure .....	80
Figure 3.9 Cell viabilities of neural progenitor cells (NPC) and murine glioma cells (GL26) as a function of the concentration of type (D-POH) <sub>10</sub> K <sub>20</sub> and (D-POH) <sub>10</sub> R <sub>20</sub> nanosponge in serum-containing medium (10% FBS, 5% horse serum) after 48h of exposure. ....	81
Figure 3.10 Functions of the different regions of each peptide branch in (D-POH) <sub>10</sub> K <sub>20</sub> and (D-POH) <sub>10</sub> R <sub>20</sub> . ....	84
Figure A.1 Synthesis of a tri-maleimide scaffold with trigonal symmetry.....	92
Figure A.2 <sup>1</sup> H-NMR spectrum of the maleimide scaffold (Varian, 400 MHz). ....	93
Figure A.3 <sup>13</sup> C-NMR spectrum of the maleimide scaffold (Varian, 400 MHz). ....	94
Figure A.4 Crystal structure of tri-maleimide.....	95
Figure A.5 Main steps of solid phase peptide synthesis <sup>1</sup> .....	96
Figure A.6 CDI activated cholesterol coupling to peptide chains .....	97
Figure A.7 H-Cys(Trt)-2-ClTrt resin .....	97
Figure A.8 Fmoc-Lys(Boc)-OH (K).....	98
Figure A.9 Fmoc-Asp(OtBu)-OH (D) .....	98
Figure A.10 Fmoc-Gly-OH (G) .....	98
Figure A.11 Fmoc-L-valine (V).....	98
Figure A.12 Fmoc-Glu(OBzl)-OH (E) .....	99
Figure A.13 CDI: 1,1'-Carbonyldiimidazole .....	99
Figure A.14 Cholesterol.....	99
Figure A.15 Cholesterol-Peptide-Trimaleimide Adduct Formation.....	99
Figure A.16 MALDI-TOF ((Voyager DE STRT) of A: Cholesterol-(D) <sub>5</sub> DEVDC, the isotope distribution is consistent with the chemical formula C <sub>71</sub> H <sub>105</sub> N <sub>11</sub> O <sub>30</sub> S; B: Cholesterol-(K) <sub>5</sub> DEVDC, the isotope distribution is consistent with the chemical formula C <sub>81</sub> H <sub>140</sub> N <sub>16</sub> O <sub>20</sub> S. ....	100
Figure A.17 MALDI-TOF ((Voyager DE STRT) of A: Cholesterol-(D) <sub>10</sub> DEVDC, the isotope distribution is consistent with the chemical formula C <sub>91</sub> H <sub>130</sub> N <sub>16</sub> O <sub>45</sub> S; B: Cholesterol-(K) <sub>10</sub> DEVDC, the isotope distribution is consistent with the chemical formula C <sub>111</sub> H <sub>200</sub> N <sub>26</sub> O <sub>25</sub> S.....	101

Figure A.18 MALDI-TOF ((Voyager DE STRT) of A: Cholesterol-(D) <sub>15</sub> DEVDC, the isotope distribution is consistent with the chemical formula C <sub>111</sub> H <sub>155</sub> N <sub>21</sub> O <sub>60</sub> S; B: Cholesterol-(K) <sub>15</sub> DEVDC, the isotope distribution is consistent with the chemical formula C <sub>141</sub> H <sub>260</sub> N <sub>36</sub> O <sub>30</sub> S.....	102
Figure A.19 MALDI-TOF ((Voyager DE STRT) of A: Cholesterol-(D) <sub>20</sub> DEVDC, the isotope distribution is consistent with the chemical formula C <sub>131</sub> H <sub>180</sub> N <sub>26</sub> O <sub>75</sub> S; B: Cholesterol-(K) <sub>20</sub> DEVDC, the isotope distribution is consistent with the chemical formula C <sub>171</sub> H <sub>320</sub> N <sub>46</sub> O <sub>35</sub> S.....	103
Figure A.20 Number-averaged size distributions and correlation curve for n=15. ....	104
Figure A.21 Number-averaged size distributions and correlation curve for n=20. ....	104
Figure A.22 RAW264.7 cells after 2h of incubation with PKH26 (1 x 10 <sup>-5</sup> M). ....	106
Figure A.23 Chemical structure of PKH26.....	106
Figure B.1 5(6)-Carboxyfluorescein.....	107
Figure B.2 Excitation and emission spectrum of 5(6)-carboxyfluorescein in PBS (pH = 7.4). .	107
Figure B.3 Concentration dependence of the emission of 5(6)-carboxyfluorescein fluorescence in PBS. ....	108
Figure B.4 DLS of 5(6)-Carboxyfluorescein-loaded type DK 20 nanosponges.....	108
Figure C.1 Fmoc-Cys(Trt)-Rink Amide MBHA resin .....	109
Figure C.2 EDC: 1-Ethyl-3-(3-dimethylaminopropyl)carbodiimide .....	109
Figure C.3 DMAP: 4-Dimethylaminopyridine .....	110
Figure C.4 FTIR of type D10K20 nanosponge before POH loading .....	110
Figure C.5 FTIR of type D10K20 nanosponge after POH loading. ....	111
Figure C.6 FTIR of type D10R20 nanosponge before POH loading.....	112
Figure C.7 FTIR of type D10R20 nanosponge after POH loading.....	113
Figure C.8 HPLC of type D10K20 nanosponge .....	113
Figure C.9 MALDI-TOF ((Voyager DE STRT) of A: D <sub>10</sub> K <sub>20</sub> DEVDC, the isotope distribution is consistent with the chemical formula C <sub>183</sub> H <sub>326</sub> N <sub>56</sub> O <sub>63</sub> S; B: D <sub>10</sub> R <sub>20</sub> DEVDC the isotope distribution is consistent with the chemical formula C <sub>183</sub> H <sub>326</sub> N <sub>96</sub> O <sub>63</sub> S. ....	114
Figure C.10 MALDI-TOF ((Voyager DE STRT) of A: (D-perillyl alcohol) <sub>10</sub> K <sub>20</sub> DEVDC, the isotope distribution is consistent with the chemical formula C <sub>283</sub> H <sub>466</sub> N <sub>56</sub> O <sub>63</sub> S; B: (D-perillyl	

alcohol) <sub>10</sub> R <sub>20</sub> DEVDC the isotope distribution is consistent with the chemical formula C <sub>183</sub> H <sub>466</sub> N <sub>96</sub> O <sub>63</sub> S.....	115
Figure C.11 Zeta potential of type (D-POH) <sub>10</sub> K <sub>20</sub> nanosponges in PBS .....	116
Figure C.12 Zeta potentials of type (D-POH) <sub>10</sub> R <sub>20</sub> nanosponges in PBS .....	116
Figure C.13 Control experiments: Cell viability of GL26 cells (cultured without serum) as a function of added perillyl alcohol (concentrations: a), type D10K20 nanosponge (concentrations: b), type D10R20 nanosponge (concentrations: b), and PBS control (concentrations: b)). .....	119
Figure C.14 COSY (1H-1H correlated spectroscopy) of type (D-POH) <sub>10</sub> K <sub>20</sub> nanosponge (0.10 mml in D <sub>2</sub> O).....	120
Figure C.15 TOCSY (total correlated spectroscopy) of type (D-POH) <sub>10</sub> K <sub>20</sub> nanosponge (0.10 mml in D <sub>2</sub> O).....	121
Figure C.16 NOESY (2D Nuclear Overhauser spectroscopy) of type (D-POH) <sub>10</sub> K <sub>20</sub> nanosponge (0.10 mml in D <sub>2</sub> O) .....	122

## List of Tables

Table 1.1 Effective hydrodynamic diameters, polydispersity indexes (PDI), and standard deviations (SD) for (cholesterol-(K) <sub>n</sub> DEV DGC) <sub>3</sub> -trimaleimide + (cholesterol-(D) <sub>n</sub> DEV DGC) <sub>3</sub> -trimaleimide nanosponges. ....	12
Table 2.1 Uptake of DK20 nanosponges by leukocytes in peripheral blood.....	48
Table 3.1 Diameter and CMC of type (D-POH) <sub>10</sub> K <sub>20</sub> and (D-POH) <sub>10</sub> R <sub>20</sub> nanosponges .....	73
Table 3.2 LC50 values of type (D-POH) <sub>10</sub> K <sub>20</sub> and (D-POH) <sub>10</sub> R <sub>20</sub> nanosponges (in $\mu\text{g/ml}$ and nmol/l) for GL26 and NPC cell lines. Experiments were conducted in serum free and serum containing media. ....	82
Table C.1 Volumes and concentrations of (D-POH) <sub>10</sub> K <sub>20</sub> nanosponge used for CMC detection .....	117
Table C.2 Volumes and concentrations of (D-POH) <sub>10</sub> R <sub>20</sub> nanosponge used for CMC detection	118

## Acknowledgements

It is a great pleasure for me to thank people whose assistance, comments and suggestions were so valuable in doing this project.

Foremost I express my devout dignity and heartiest gratitude to my PhD advisor Prof. Stefan H. Bossmann for his invaluable guidance and continuous support throughout my PhD. Without his exceptional mentorship it would not be possible to conduct this research.

I am also grateful to my PhD advisory committee, Prof. Duy H. Hua, Prof. Deryl L. Troyer, Prof. Paul E. Smith and Prof. Sherry Fleming for their valuable time and support. I am also grateful to Prof. Eric Maatta who was one of my former committee members.

My sincere thanks go to Mrs. Katrin Bossmann for her tremendous support and encouragements in every possible way.

I also appreciate former and current Bossmann group members for their great support, especially Dr. Hongwang wang for sharing his research experience and knowledge.

Special thanks go to Dr. Sebastian Wendel for helping with the cell experiments.

I would like to thank Troyer group members especially Dr. Tej Shrestha and Ms. Marla Pyle for training me to work in BSL2 lab and helping to conduct cell experiments.

I am very grateful to Prof. Emily McLaurin, Prof. Ping Li, Prof. Daniel Higgins, prof. Christer Aakeroy for allowing me to use their laboratories and instruments.

I would also like to thank Dr. Leila Maurmann for helping with the NMR and the non-academic staff; Mr. Jim Hodgson, Mr. Ron Jackson and Mr. Tobe Eggers for helping with technical issues and preparing equipment for my research.

Last, but not least, my warm thanks go my family; my beloved husband Chamara, my parents and my brother for their unconditional love, support, encouragements and blessings.

## **Dedication**

To my loving husband Chamara, my parents and my brother

# Chapter 1 - Rationally Designed Peptide Nanosponges for Cell- Based Cancer Therapy

## 1.1 Abstract

A novel type of supramolecular aggregate, named a “nanosponge” was synthesized through the interaction of novel supramolecular building blocks with trigonal geometry. The cholesterol-(K/D)<sub>n</sub>DEV DGC)<sub>3</sub>-trimaleimide unit consists of a trigonal maleimide linker to which homopeptides (either K or D) of variable lengths (n = 5, 10, 15, 20) and a consensus sequence for executioner caspases (DEV DGC) are added via Michael addition. Upon mixing in aqueous buffer cholesterol-(K)<sub>n</sub>DEV DGC)<sub>3</sub>-trimaleimides and a 1:1 mixture of cholesterol-(K/D)<sub>n</sub>DEV DGC)<sub>3</sub>-trimaleimides forms stable nanosponges, whereas cholesterol-(D)<sub>n</sub>DEV DGC)<sub>3</sub>-trimaleimide is unable to form supramolecular aggregates with itself. The structure of the novel nanosponges was revealed through explicit solvent and then coarse-grained molecular dynamics (MD) simulations. The nanosponges are between 80nm and several micrometers in diameters and virtually non-toxic to monocyte/macrophage-like cells.

## 1.2 Background

### 1.2.1 Classic Liposomes and Peptide Vesicles

Targeted delivery of therapeutics to the tumor site is of vital importance in cancer treatment. This approach is not only able to maximize the treatment efficacy of therapeutics at the cancer site(s), but also to minimize the side effects caused by the therapeutics in conventional cancer treatment.<sup>1-2</sup> One method to achieve targeting delivery is to use a delivery modality designed to carry the therapeutics to the desired site, and then release them in the tumor.<sup>3-6</sup> Liposomes are a well-recognized example of drug delivery devices. Composed of a simple lipid bilayer, liposomes are non-cytotoxic, biocompatible, biodegradable, and capable of integrating or encapsulating large payloads of both hydrophilic and hydrophobic drugs.<sup>7</sup> Drugs incorporated into these nanocarriers can be accumulated in tumor tissue through enhanced permeability and retention (EPR) effect.<sup>8-10</sup> Numerous liposome based drugs have been approved by the FDA, and many more are at different stages of clinical trials.<sup>11</sup> Despite their successes, liposomes have limitations. It is noteworthy that the preparation of liposome based drug requires multistep procedures (i.e., hydration<sup>12-13</sup>, sonication<sup>14-15</sup>, extrusion<sup>16-17</sup>, using a size selective column<sup>18</sup>, etc.) in order to obtain narrow particle size distribution and separation from unloaded drugs. These tedious processes are associated with a high risk of damaging the entrapped drugs. Furthermore, the EPR effect is only slightly selective, thus achieving rarely more than 5 percent delivery of a nanotherapeutic drug to the tumor site(s).<sup>8-10</sup> Finally, liposomes are prone to systemic leaking of drugs, especially at longer circulation times.<sup>19</sup>

Self-assembling peptides are an attractive alternative to liposomes. For example, short amphiphilic sequences, acetyl-AAVLLLLW-(E)<sub>n=2/7</sub>-COOH, form nanosized vesicles

spontaneously in aqueous media at neutral pH. Hydrophilic molecules can be incorporated inside the vesicles.<sup>20</sup> Longer block copolypeptides poly(L-lysine)-*b*-poly(L-leucine),  $K_xL_y$  ( $x = 20$  to  $80$ ,  $y = 10$  to  $30$ ), form stable vesicles and micelles in aqueous solution with size ranging from 1 to 10  $\mu\text{m}$  in diameter. These assemblies showed high degrees of membrane fluidity; as a result, they can be resized with precise control from ten to hundreds nanometer in diameter using liposome-based extrusion techniques.<sup>21</sup> The Tomich group reported two branched peptides with different lengths, mimicking diacyl glycerols, form water-filled vesicles which can entrap water soluble dyes.<sup>22-25</sup>

### **1.2.2 The EPR Effect Works Well in Mice, but Not in Humans**

During the last decade, it has become more and more evident that both, classic liposomes and peptide vesicles are facing the problem of ineffective drug delivery in humans. It is an emerging paradigm that the Enhanced Permeation and Retention Effect (EPR) works well in mouse models of cancer, but not in the clinic.<sup>10, 26-27</sup> Drug transport as a payload of either stem cells<sup>28</sup> or defensive cells<sup>27</sup>, which migrate to tumors following their cytokine/chemokine secretion, is a new concept that has been proven effective in animal models. Currently, clinical translation of cell-based treatment method for cancer and other diseases are rapidly progressing.<sup>29</sup> Therefore, we have developed “peptide nanosponges” for efficient targeting of defensive cells in peripheral blood, as well as cultured stem cells.

### 1.2.3 Peptide Nanosponges

Peptide nanosponges that are reported here, are capable of effectively delivering their payload to defensive cells and stem cells. Especially autologous cells have the potential of truly personalized medicine when treating solid tumors and metastases.<sup>30</sup>

Here, we report the synthesis of a series of (K)<sub>n</sub>DEVGDC, and (D)<sub>n</sub>DEVGDC peptide sequences, where *n* equals to 5, 10, 15, 20 respectively. We have capped the N-terminal of the peptides with cholesterol, and further linked the peptides to a trimaleimide scaffold via Michael-addition.<sup>31</sup> We have obtained one positively and one negatively charged adduct [(cholesterol-(K)<sub>n</sub>DEVGDC)<sub>3</sub>-trimaleimide and (cholesterol(D)<sub>n</sub>DEVGDC)<sub>3</sub>-trimaleimide]. Upon mixing of the adduct pairs (*n* equals to 15 or 20) equimolarly under physiological conditions, nanosponges of very low polydispersity form instantaneously, which were characterized with dynamic light scattering (DLS), transmission electron microscopy (TEM), and atomic force microscopy (AFM).

Our computer modelling has indicated that the structure of the nanosponges is indeed “sponge-like”: numerous hydrophilic and hydrophobic nanodomains exist in direct proximity. We attribute the novel (bio)physical properties of the nanosponges to their formerly unknown structure.

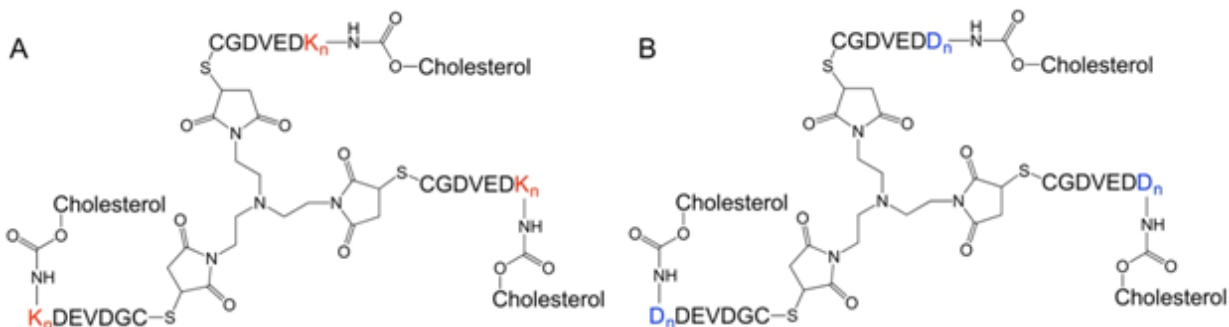


**Figure 1.1 Tri-maleimide based peptide structures: components for the spontaneous formation of nanosponges. A: lysine-based materials,  $n = 5, 10, 15, 20$ ; B: aspartic acid-based materials,  $n = 5, 10, 15, 20$**

Our studies demonstrated that hydrophobic molecules, for example the cyanine 3.0 dye PKH26, can be incorporated inside these nanosponges. In the presence of cancer related proteases (e.g. caspase-3, 6 or 7<sup>32</sup>), these nanovesicles can be – principally - digested, leading to the possibility of triggered release of the payload. We found that the nanosponges are essentially non-toxic, and that these cells internalize them with high efficiency.

Based on these proof-of-concept experiments, our novel peptide-based nanosponges are very well suited for applications in specific drug delivery to solid tumors and metastases by means of cell-based therapy.

## 1.3 Methods

### 1.3.1 Trimaleinimide Scaffold Synthesis

A flexible trimaleinimide scaffold was synthesized by means of a two-step reaction. In the first step, reacting tris(2-aminoethyl)amine with 3 equivalents of maleic anhydride in acetic acid at room temperature produces the trimaleimic acid adduct.<sup>33</sup> In the second step, the trimaleimic acid adduct and sodium acetate were heated in acetic anhydride for 30 min. at 100 °C to give the desired product.<sup>34</sup> The crude product was recrystallized from saturated ethyl acetate, and fully characterized by <sup>1</sup>H-, <sup>13</sup>C- NMR, and single crystal x-ray analysis (see Appendix A.1-A.4).

### 1.3.2 Peptide Synthesis

Oligopeptides were synthesized by means of solid phase peptide synthesis on 2-chlorotrityl resin.<sup>35-36</sup> Three equivalents of F<sub>moc</sub> (N-(9-fluorenyl)methoxycarbonyl) protected amino acid and HBTU were dissolved in a DIEA/DMF solution, and added to the 2-chlorotrityl resin preloaded with 0.20 mmol of amino acid per g. The solution was drained from the resin after 30 minutes of reaction. This process was repeated one more time. Then, the F<sub>moc</sub> group of the newly introduced amino acid was removed by using 20% (v/v) piperidine in DMF. Following this procedure, stepwise addition of F<sub>moc</sub>-protected amino acids resulted in the desired peptides. The N-terminal of the peptides were capped with cholesterol while still being on the resin by reacting with CDI activated cholesterol in DMF solution.<sup>35-36</sup> The final product was cleaved off the resin in TFA/water/TIPS (95:2.5:2.5, v/v/v) cocktail for 3 hours at room temperature.<sup>36</sup> White solid product formed when adding the cocktail into cold anhydrous diethyl ether. The product was collected by centrifugation (3000 rpm, 10 min), washed with cold diethyl ether for three times,

and dissolved in water prior to lyophilization. The products were purified by using a GE peptide column (mobile phase: aqueous 0.05 M TEA/acetic acid buffer, pH = 7.0), and dried in high vacuum.

### **1.3.3 Cholesterol-Peptide-Trimaleimide Adduct Formation**

3.5 equivalents of cholesterol-peptide and 1 equivalent of trimaleimide were dissolved in deoxygenated PBS buffer (pH=7.4), and stirred under argon atmosphere for 24 hours.<sup>37</sup> After removing the solvent by lyophilization, the crude product was purified by dialysis (molecular weight cutoff 3500) against distilled water. The final product inside the membrane bag was lyophilized and further dried under high vacuum.

### **1.3.4 Nanosponge Formation and DLS Characterization**

Separate solutions of (cholesterol-(K)<sub>n</sub>DEV DGC)<sub>3</sub>-trimaleimide and (cholesterol-(D)<sub>n</sub>DEV DGC)<sub>3</sub>-trimaleimide in deoxygenated PBS buffer were prepared and filtered through 200 μm filters. The prepared stock solutions were 0.050 mM and 0.50 mM. All other stock solutions were prepared by diluting the original solutions with deoxygenated PBS buffer. The two solutions were quickly mixed and vortexed for 30 s. The hydrodynamic diameters and polydispersity indexes (PDI) of the formed nanosponges were measured by dynamic light scattering (DLS, ZetaPALS, Brookhaven Instruments Corp., Holtsville, NY).<sup>38</sup> All measurements were carried out at 25 °C, using 658 nm laser wavelength, and 90 degree detection angle. Data were collected from an average of three measurements over 60 seconds. DLS was also used to estimate the critical micellar concentration (cmc) of the nanosponges.

### **1.3.5 AFM Characterization**

Samples for atomic force microscopy (AFM) were prepared by adding one drop of the nanosponge stock solution (0.050 M of each component in PBS) onto a freshly peeled MICA sheet, and followed by removing of the solvent by using a gentle nitrogen stream (2 min). AFM images were taken by the Bruker Innova AFM image system (Bruker, Camarillo, CA) utilizing TESPA-HAR probes in tapping mode. The spring constant of the tip was 50 N/m and the frequency was 350 kHz. The set point, P gain and I gain were set at 1.2, 0.6 and 0.5, respectively. The images were gathered with 256x256 pixel resolution at a scan rate of 1 Hz. The images were then analyzed by the Nanoscope software (Bruker).

### **1.3.6 TEM Characterization**

Samples for transmission electron microscopy (TEM) were prepared by dropping 10  $\mu$ L of 0.005% peptide solution in PBS directly on a glow discharged TEM grid. Uranyl acetate was used as a positive staining agent. In all cases electron microscopy was performed at an accelerating voltage of 200 kV. Nanosponge morphology on HOPG was examined by bright-field and dark-field transmission electron microscopy (TEM) using a FEI Technai G<sub>2</sub> transmission electron microscope at an electron acceleration voltage of 200 kV. High resolution images were captured using a standardized, normative electron dose and a constant defocus value from the carbon-coated surfaces. All TEM measurements were performed at the Microscopy and Analytical Imaging Laboratory of the University of Kansas.<sup>39</sup>

### 1.3.7 Force Field Calculations

For the united atom simulations we have extended the Gromos 53a6 FF<sup>40</sup> to include cholesterol, the maleimide ring attachment to Cys, and the nitrogen cap. The cholesterol parameters were obtained from the Automated Topology Builder (ATB) website.<sup>41</sup> This was then modified to attach the cholesterol to the amino acid chain through an O.C=O.NH linkage involving the cholesterol O and the peptide N-terminal N. Standard atom types consistent with the Gromos FF were used. The charges on the carbonyl group were assigned to be the same as that in a peptide group ( $\pm 0.45$ ), while estimated charges of  $\pm 0.20$  were assigned to the cholesterol oxygen and the carbon to which it is attached. The maleimide ring was added to an existing Cys topology using standard atom types and C-S-C charges of 0.241/-0.482/0.241, as observed for the same connectivity in Met. Both ring carbonyl groups were assigned charges of  $\pm 0.45$ , while the N-C bond was assigned a dipole of  $\pm 0.2$ . The protonated triethyl nitrogen group charges were approximated to be 0.2 on each H, N and carbon – close to the charges found in Lys. All bond lengths, bond angles, improper dihedrals, and torsions were assigned, based on atom type, using the usual the standard Gromos rules.

The CG topology was based on the MARTINI protein FF.<sup>42</sup> A cholesterol CG FF exists and this was used here.<sup>43</sup> The maleimide ring was modelled using three beads – two polar and one nonpolar. The ring was attached to the side chain bead of Cys and to a bead representing the two ethyl carbons, with another single bead for the nitrogen cap. Coil secondary structure bead types were used for all beads. The MARTINI FF does not, in general, include chain flexibility for peptides.<sup>42</sup> However, we considered this to be an important factor for the present systems. To ensure a reasonable description of the chain flexibility was obtained during the CG simulations we compared the angle and dihedral distributions obtained from the CG simulations with the

distributions from the Gromos united atom FF. In particular, we examined the connectivity between cholesterol and the peptide chain, the connection between Cys and the maleimide ring, and the ring-N-ring arrangement. Attention was also paid to the dihedral angle distribution for consecutive backbone beads for the poly-Lys and poly-Asp chains. The force constants and equilibrium parameters were then adjusted to best reproduce the distributions observed during the united atom simulations. A comparison of the united atom and CG distributions, as provided by the original MARTINI FF, for the peptide chain C<sup>α</sup> pseudo dihedrals suggested that there were some differences between the FFs. However, additional testing indicated that this had little effect on the results presented here.

### **1.3.8 Entrapment of PKH26 within Peptide Nanosponges**

PKH26 solution was prepared by dissolving 10 μL of the PKH26 ethanolic dye solution (Sigma-Aldrich) to 1.0 mL of Diluent C in a polypropylene centrifuge tube, followed by addition of double-distilled water (pH = 6.90) to bring the total volume to 2.0 mL (final PKH26 concentration  $5.0 \times 10^{-6}$  M). Equal molar amounts of cholesterol-(K)<sub>20</sub>DEV DGC<sub>3</sub>-trimaleimide and cholesterol-(D)<sub>20</sub>DEV DGC<sub>3</sub>-trimaleimide (1.0 mM of each component) were added to the above dye solution. After brief sonication, the homogeneous solution was incubated at 37 °C for 6 hours without light exposure. The free dye was removed by passing the entire sample through a Sephadex G-50 gel filtration column using double-distilled water as eluent. The collected fractions containing the nanosponges were lyophilized to dryness, and re-hydrated with PBS buffer (pH=7.4). The DLS measurement showed that the hydrodynamic diameter of the nanovesicles were between 110 to 130 nm.

### 1.3.9 Cell Experiments and MTT Assays

The cytotoxicity of the PKH26 containing nanosponges was assessed by utilizing the MTT assay<sup>44</sup> on RAW264.7 monocyte/macrophage-like cells<sup>35</sup>. Cell experiments were carried out in DMEM supplemented with 10% FBS (Sigma-Aldrich), 5% horse serum (Invitrogen), 1% glutamine (Invitrogen), and 1% penicillin- streptomycin (Invitrogen). The percentage of live cells was determined after 24 and 48 hours of incubation. Cells were seeded in T-25 flask with suitable medium (RAW264.7: RPMI medium). After 24 h of incubation at 37 °C, cells were re-plated in a 96 well plate at 20000/cm<sup>2</sup> density and further incubated for 24 h at 37<sup>0</sup>C to obtain 80 % confluency.

Concentration series of the nanosponge composed of (cholesterol-(K)<sub>20</sub>DEV DGC)<sub>3</sub>-trimaleimide and (cholesterol-(D)<sub>20</sub>DEV DGC)<sub>3</sub>-trimaleimide (0.0, 0.1, 0.2, 0.5, 1.0, 2.0, 5.0, 10, 20, 40, 60, 80, 100 μmoles L<sup>-1</sup> in total, molar ratio 1:1) was prepared by dissolving the nanosponge components in the same media that were used for culturing the cells. Cells were incubated for 24/48 h at 37 °C. Eight replicates were prepared for each concentration. A portion of 10 μL of MTT reagent (5 mg/ml in PBS) was added to each well, and the plates were incubated for another 4 h at 37 °C. Finally, 100 μL of the cell solvent solution was added into each well and incubated for 24 h at 37 °C. Their absorbance was recorded by using a plate reader at 550nm and 690nm. PBS solution was used as control for all the experiments.

RAW264.7 cells were imaged by using a Leica DMRD microscope with darkfield, brightfield, phase contrast and epifluorescence illumination, a camera system and an Optronics 870 color CCD camera attached to a Bioquant True color image analysis system.

## 1.4 Results

### 1.4.1 DLS Characterization of the Nanosponges

The effective diameters and the polydispersity index (PDI) values of the nanosponges obtained by dynamic light scattering measurements (DLS) are summarized in Table 1. These results indicate that nanosponge formation depends on the number of lysine/aspartic acid units. Larger aggregates with higher polydispersity are observed when  $n$  equals 5. A significant decrease in both size and PDI (polydispersity index) was observed when increasing  $n$  to 10 (439 nm and 0.26). A further increase of  $K$  and  $D$  to 15 and 20 led to virtually mono-dispersed nanosponges with effective diameters of approx. 200nm. It is noteworthy that the formation of these nanosponges is spontaneous upon mixing of the adduct solutions. Continuous monitoring by DLS for 12 hours at 298 K revealed that the nanosponges are very stable in aqueous solution (PBS). For drug delivery purposes, we are particularly interested in nanosponges of 100 to 200 nm in diameter. Further characterization was carried out for  $n = 15$  and 20. The corresponding correlation curves and number-averaged size distributions are shown in the Appendix A (Figure A.19 and A.20). Hydrodynamic diameters remained virtually constant for 12h.

$n$ (D and K) =	Effective diameter $\pm$ SD (nm)	PDI $\pm$ SD
5	1,200 $\pm$ 240	0.642 $\pm$ 0.07
10	440 $\pm$ 50	0.26 $\pm$ 0.04
15	200 $\pm$ 5.0	0.077 $\pm$ 0.01
20	180 $\pm$ 25	0.201 $\pm$ 0.03

**Table 1.1 Effective hydrodynamic diameters, polydispersity indexes (PDI), and standard deviations (SD) for (cholesterol-(K) $_n$ DEV DGC) $_3$ -trimaleimide + (cholesterol-(D) $_n$ DEV DGC) $_3$ -trimaleimide nanosponges (0.050 mM of each component in PBS).**

### 1.4.2 CMC of the Nanosponges

In analogy to the formation of micelles, a critical concentration at which spontaneous aggregation to nanosponges occurs, was determined. This molar concentration was named CMC in analogy to “critical micellar concentration”. In a monodisperse nanomaterial solution, the correlation curve ( $C(t)$ ) of the measured data in a dynamic light scattering (DLS) experiment is a smooth, single exponential decay function. The diffusion coefficient ( $D$ ) is proportional to the lifetime of the exponential decay and can be calculated by fitting the correlation curve to an exponential function. The hydrodynamic diameter of particles can be obtained by using a variation of the Stokes-Einstein equation with known  $D$  value.<sup>45</sup> Based on basic DLS theory, we measured the critical concentrations for the nanosponge formation of (cholesterol-(K)<sub>20</sub>DEV DGC)<sub>3</sub>-trimalleimide (K) and a 1:1 mixture of (cholesterol-(D)<sub>20</sub>DEV DGC)<sub>3</sub>-trimalleimide (D) and (cholesterol-(K)<sub>20</sub>DEV DGC)<sub>3</sub>-trimalleimide (K). The concentrations of D, K, and DK were stepwise increased by adding microliter aliquots from stock solutions of 0.50 M each to 1.0 mL of PBS buffer in a cuvette. The endpoint indication of this titration curve is the appearance of a smooth, single exponential decay correlation curve. (Cholesterol-(D)<sub>20</sub>DEV DGC)<sub>3</sub>-trimalleimide (D) did not show significant aggregation even after increasing its concentration to 0.30 mM. For (cholesterol-(K)<sub>20</sub>DEV DGC)<sub>3</sub>-trimalleimide a smooth, single exponential decay curve was observed when its concentration reached 0.080 mM. The equimolar mixture of (cholesterol)-(D)<sub>20</sub>DEV DGC)<sub>3</sub>-trimalleimide and (cholesterol-(K)<sub>20</sub>DEV DGC)<sub>3</sub>-trimalleimide (DK) showed most facile nanosponge formation at a concentration as low as 0.0050 mM (total concentration, 0.0025 mM (D) and 0.0025 mM (K)). In comparison, sodium dodecyl sulfate micelles possess a CMC of approx. 8 mM at 298K, which corresponds to 2.31 g L<sup>-1</sup>. In

comparison, only about  $0.055 \text{ g L}^{-1}$  of type DK nanospheres and  $0.90 \text{ g L}^{-1}$  of type K nanospheres are required to achieve spontaneous aggregation.

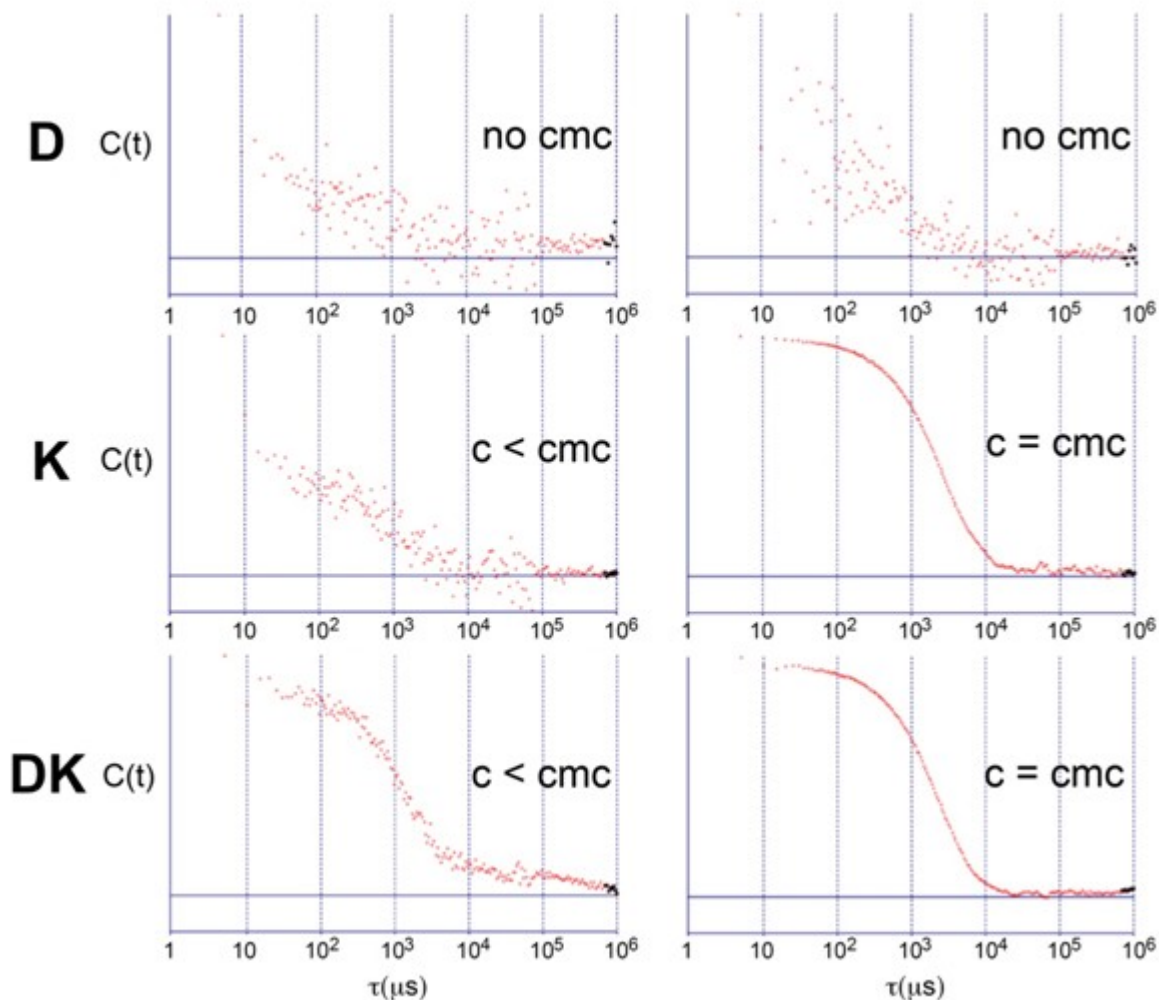


**Figure 1.2** Correlation curves ( $C(t)$ ) of dynamic light scattering measurements of cholesterol-(D)<sub>20</sub>DEV(DGC)<sub>3</sub>-trimalleimide (D), cholesterol-(K)<sub>20</sub>DEV(DGC)<sub>3</sub>-trimalleimide (K), and mixture (1/1 molar ratio) of both nanosphere components (DK) in  $1\times$  PBS buffer. In the left column, the concentrations of K, and DK are below the cmc (critical micellar concentration, here: concentration at which aggregation occurs). In the right column the concentrations are at their respective cmc (0.080 mM for type K and 0.0050 mM for type DK). No aggregation was observed for D in the concentration interval from 0.01 (left) to 0.30 mM (right).

### 1.4.3 AFM Characterization

Figure 1.3 shows the AFM images of (cholesterol-(D)<sub>15</sub>DEV DGC)<sub>3</sub>-trimaleimide/cholesterol-(K)<sub>15</sub>DEV DGC)<sub>3</sub>-trimaleimide and (cholesterol-(D)<sub>20</sub>DEV DGC)<sub>3</sub>-trimaleimide/ (cholesterol-(K)<sub>20</sub>DEV DGC)<sub>3</sub>-trimaleimide nanosponges. Type DK15 nanosponges formed 0.5-0.9 μm aggregated bundles. The height of the bundles is between 150 to 250 nm. At higher magnification, it can be discerned that each bundle was formed by 3 to 5 smaller subunits. The diameter of the subunits ranges from 150 nm to 200 nm. Type DK20 nanosponges formed well defined individual nanosponges of 85 to 110 nm in size. Their height falls into the same range, indicating the formation of spherical nanosponges.

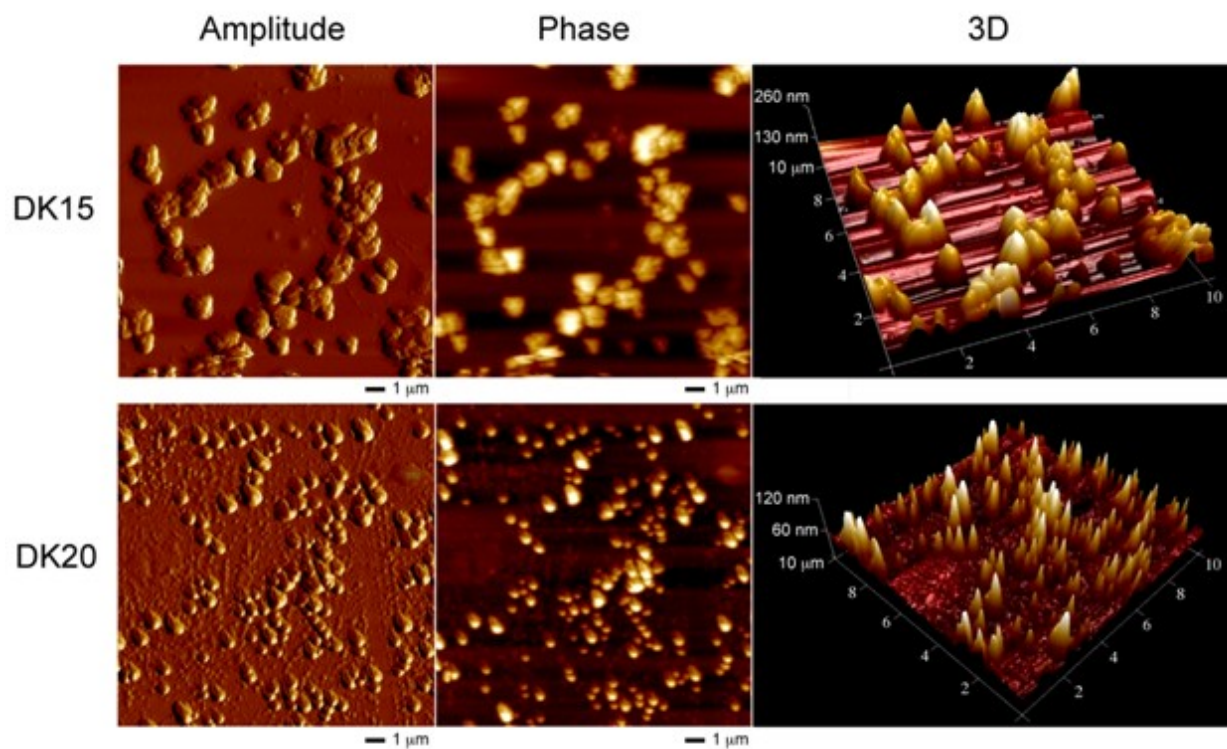


**Figure 1.3 AFM (amplitude, phase, and 3D) images of type DK15 and type DK20 nanosponges. “15” and “20” refer to the number of D and K units in the oligopeptides that are attached to trimaleimide linkers.**

### 1.4.4 TEM Characterization

TEM images for type DK20 nanosponges are shown in Figure 1.4. 2D-projections of spherical sponges with diameters between 85 to 100 nm are clearly discernible Figure 1.4A. Their size distribution is displayed Figure 1.4B. However, smaller structures that are 35 to 45 nm in size can also be found in the TEM images. It is noteworthy that the exterior of the nanosponges acquired strong uranyl stains. This is an indication that cholesterol-(D)<sub>20</sub>DEV DGC<sub>3</sub>-trimaleimide is enriched at the exterior of the nanostructures.

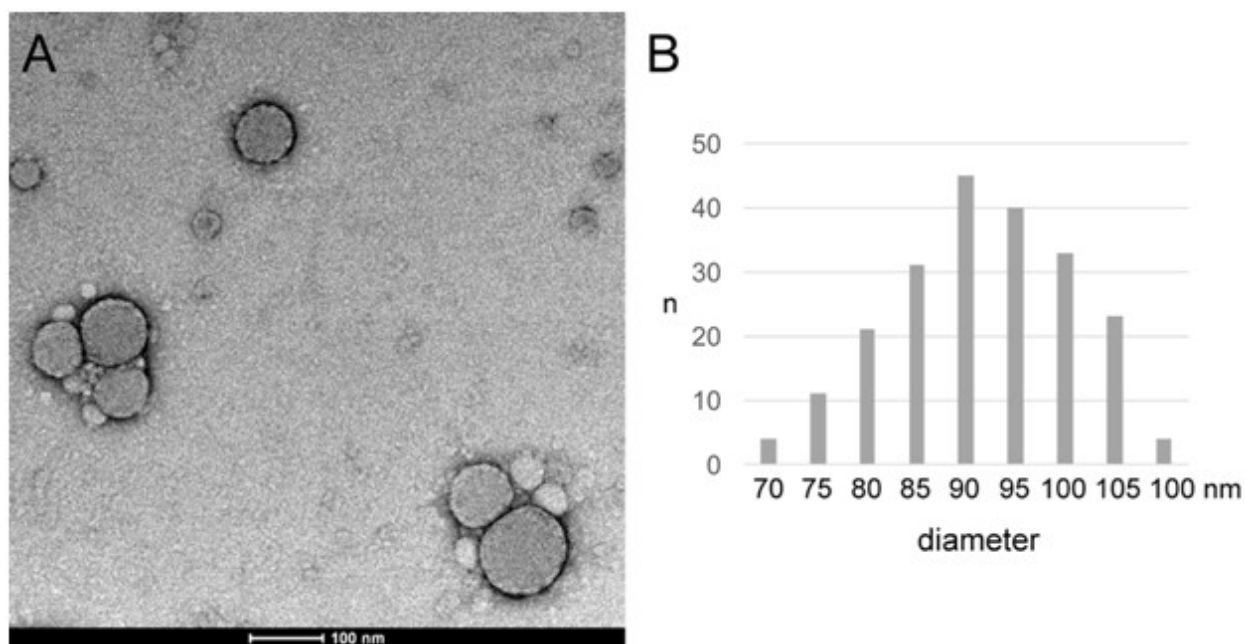


**Figure 1.4 A:** TEM image of type DK20 nanosponges on graphite with uranyl acetate as positive staining. **B:** Histogram of the size distribution of the larger nanosponges, obtained by using Image J (n: number of nanosponges counted in each group).<sup>46</sup>

### 1.4.5 Force Field Calculations

In an effort to elucidate the structure of the peptide aggregates we have performed all atom (AA) explicit solvent and coarse-grained (CG) molecular dynamics (MD) simulations. All of these calculations were performed by our collaborators Prof. Dr. Paul E. Smith and Nilusha

Kariyawasam in the Chemistry Department of Kansas State. The calculations are included here to permit a direct comparison of experimental results and theoretical predictions.

A detailed description of the models used, together with technical aspects of the simulations, is provided in the Methods and in the Appendix A sections. However, before simulating the aggregation process itself it is important to check that the CG models are sufficiently accurate that reasonable results can be obtained. CG simulations are required as the systems under investigation involve large molecular aggregates. However, CG models generally provide rather crude representations of electrostatic interactions and conformational flexibility. As both these aspects are clearly present in the systems to be studied here, we have also investigated the ability of our CG models to mimic the more accurate AA explicit solvent analogues.

#### **1.4.5.1 Force Fields**

The simulations described here involve molecules for which no force fields (FFs) are currently available. Here, we describe our approach to provide reasonable descriptions of these systems using united atom and coarse-grained (CG) approaches. Highly accurate FFs for these systems would require significant development and may also necessitate experimental data that is not available. Hence, we have taken a more approximate, but practical, approach. We feel this is appropriate as we are probing the overall behavior of the systems, and the requirement of CG models to study such large systems already introduces significant approximation.

The results from 100 ns AA and 1  $\mu$ s CG MD simulations of the ss-Lys and ss-Asp peptides have been compared. Electrostatic interactions followed the usual approach for the MARTINI models,<sup>42</sup> while partial conformational flexibility was introduced as described in the Appendix A. The results are illustrated in Figure 1.5A. The most notable behavior of the two peptide

strands was the extended structures observed for cholesterol-(D)<sub>20</sub>DEV DGC, and the collapsed structures observed for cholesterol-(K)<sub>20</sub>DEV DGC strands, as indicated by the AA simulations. The collapse of the cholesterol-(K)<sub>20</sub>DEV DGC chain appears to require cholesterol as removal of this group eliminated any chain collapse (data not shown). This later observation is then in agreement with experimental data on poly-lys and poly-asp strands,<sup>47-49</sup> where the chains adopt extended or random coil structures. Clearly, the presence of cholesterol modifies this behavior. However, the same is not true for cholesterol-(D)<sub>20</sub>DEV DGC, which remains extended even in the presence of the cholesterol linkage. Most importantly, this difference in behavior is well reproduced in the CG simulations which also give rise to an extended cholesterol-(D)<sub>20</sub>DEV DGC and collapsed cholesterol-(K)<sub>20</sub>DEV DGC structures. Further examination of the cholesterol-(K)<sub>20</sub>DEV DGC simulation did not reveal any secondary structure formation upon collapse. Nevertheless, the identical behavior observed for the AA and CG models suggests that conformational flexibility and electrostatic interactions in these systems are sufficiently well represented that one can have confidence in the CG simulations.

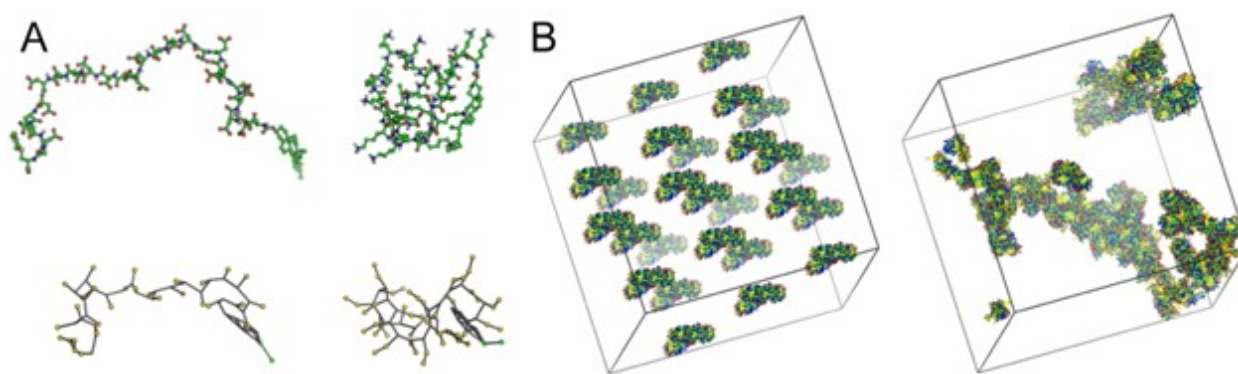


**Figure 1.5 A: Final structures obtained from the AA (top) and CG (bottom) simulations of cholesterol-(D)<sub>20</sub>DEV DGC (left) and cholesterol-(K)<sub>20</sub>DEV DGC (right). B: Initial and final (4μs) structures obtained from the CG simulation of (cholesterol-(K)<sub>20</sub>DEV DGC)<sub>3</sub>-trimaleimide and (cholesterol-(D)<sub>20</sub>DEV DGC)<sub>3</sub>-trimaleimide.**

The aggregation of equimolar mixtures of (cholesterol-(K)<sub>20</sub>DEV DGC)<sub>3</sub>-trimaleimide and (cholesterol-(D)<sub>20</sub>DEV DGC)<sub>3</sub>-trimaleimide was performed in two steps using just CG MD simulations. In the first step, we randomly placed four (cholesterol-(K)<sub>20</sub>DEV DGC)<sub>3</sub>-trimaleimides and four (cholesterol-(D)<sub>20</sub>DEV DGC)<sub>3</sub>-trimaleimides in a relatively small simulation box (15 nm in length), then transferred this peptide arrangement to a larger solvated box (40 nm in length) and simulated for 1  $\mu$ s. This places the molecules in close proximity and they quickly formed a single relatively compact aggregate. In the second step the peptide aggregate was resolvated in a 15 nm length box, and then replicated in all three directions to form the final simulation box (45 nm in length) that was then simulated for 4  $\mu$ s. During this period the smaller aggregates formed larger aggregates. This behavior is illustrated in Figure 1.6. Here, the smaller aggregates formed larger worm-like structures. Indeed, after 4  $\mu$ s there were no isolated aggregates as all peptides chains contacted at least one other peptide chain. Clearly, the final structure obtained here does not represent that of a typical spherical vesicle, but more of a nanosponge. However, this is not too surprising as the peptides used here do not possess significant amphiphilic character compared to lipids, for example. Nevertheless, aggregation is observed in agreement with the experimental results described above, and other studies of poly-lys and poly-asp mixtures.<sup>50</sup>

While appearing largely amorphous the final structure obtained in Figure 1.5B does display some interesting features. There was no strong evidence for secondary structure formation by either the tri-lys or tri-asp chains. While water did appear to be largely excluded from the chain contacts, there were visible cavities that appeared large enough to contain small molecules. An enlarged view of a section of the aggregate is display in Figure 1.6. Here one can see a preference of Asp side chains, over Lys side chains, for the surface. There was significant

aggregation of cholesterol molecules to form stacked structures. However, these do not appear to be large enough to hold the aggregate together. Rather, electrostatic interactions appeared to be the main stabilizing force. The Asp-Lys side chain coordination numbers were determined to be 2.8 for the intermolecular contacts out to a distance of 0.7 nm.

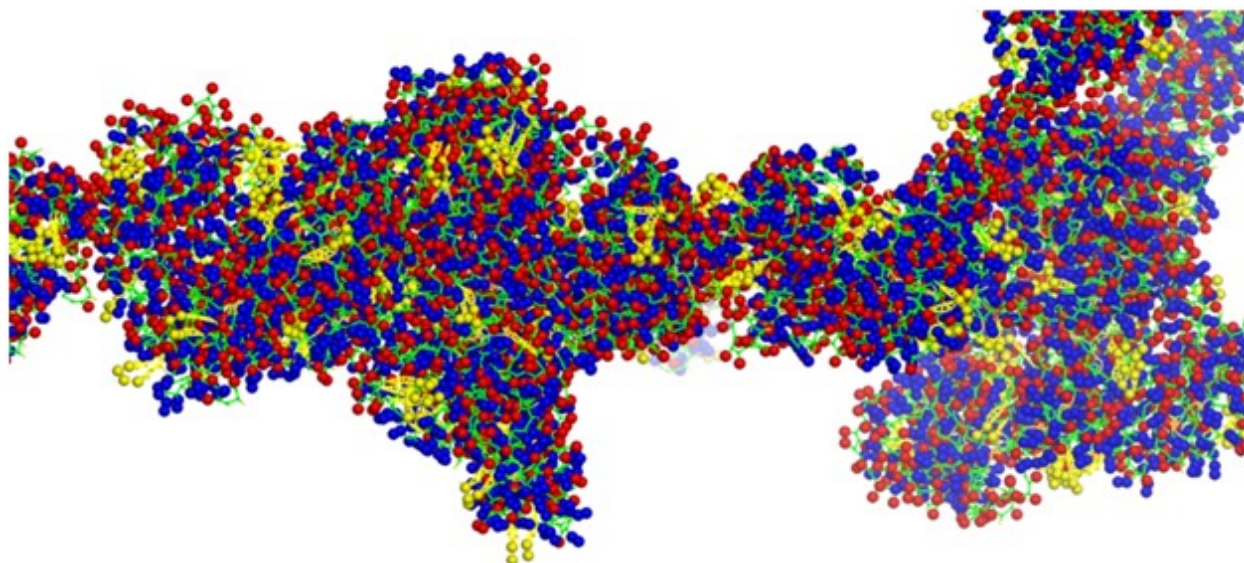


**Figure 1.6 Expanded view of the final structure obtained from the CG MD simulations. The peptide backbone is displayed as green sticks, the Asp side chains are displayed as red balls, the Lys side chains are displayed as blue balls, while the cholesterol molecules are colored yellow. The structure resembles a “nanosponge” with hydrophobic and hydrophilic areas, as well as solvent-filled cavities.**

#### **1.4.6 Uptake of PKH26-containing Nanosponges by RAW264.7 Cells**

Cell loading of the PKH26 entrapped nanosponges was tested on RAW264.7 monocyte/macrophage-like cells. This cell type was selected, because it can be used as carrier in cell-mediated cancer therapy.<sup>51-53</sup> Results indicated that type DK20 nanosponges can be loaded into RAW264.7 within 2 hours. Under the fluorescence microscope, intensive red fluorescence spots can be discerned inside the cells, which is very different from labelling cells with free PKH26, which leads to uniform labeling (see Appendix A.21). This indicates that after being taken up by these cells, the PKH26 is still entrapped inside the nanosponges. The PKH26-

containing type DK20 nanosponges in Raw264.7 cells were studied over 24 h, 48h, and 72 h. Virtually no leaching of the dye was observed by fluorescence microscopy within 72h.

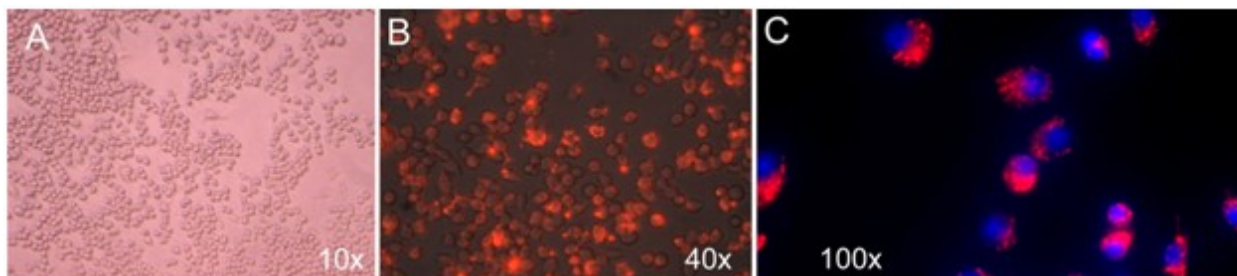


**Figure 1.7 A: RAW264.7 cells (control); B: RAW264.7 cells after 2h of incubation with 50  $\mu$ M of PKH26-containing type DK nanosponges; C: Fluorescence microscopy of RAW264.7 cells featuring PKH26-containing nanosponges 72h after uptake (DAPI counterstain).**

#### **1.4.7. Cell Toxicity of the Peptide Nanosponges**

We have performed classic MTT cell proliferation assays<sup>35, 51-53</sup> to measure the cell viability of RAW264.7 cells after incubation with PKH26-containing type DK20 nanosponges. As Figure 1.8 indicates, the type DK20 nanosponges are essentially not toxic to monocyte/macrophage-like cells, even at 100  $\mu$ M concentration.

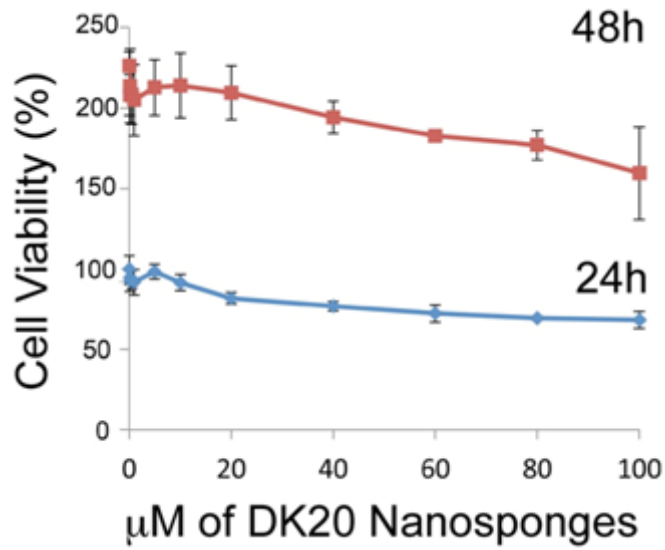


**Figure 1.8 Cell viability of RAW264.7 cells as a function of type DK20 nanosponge concentration and incubation time (24h and 48h), as measured by the MTT assay.<sup>35, 51-53</sup> Nanosponges were added to the cell culture medium in their respective concentrations (see methods section).**

## 1.5 Discussion

A good targeted drug delivery system should have the following characteristics: a) composed by biocompatible and biodegradable materials, b) fast assemble and cargo loading, c) minimal systemic leaking during delivery, d) fast release upon arrival at interested site.<sup>54</sup> We have designed (cholesterol-(K)<sub>n</sub>DEV DGC)<sub>3</sub>-trialeimide and (cholesterol-(D)<sub>n</sub>DEV DGC)<sub>3</sub>-trialeimide units that both feature a trigonal linker, a cleavable sequence designed for executioner caspases-3,6, and 7 (DEV DGC<sup>32</sup>) and either an oligo-lysine or oligo-aspartic acid sequence of variable length (n = 5, 10, 15, 20). Whereas the cysteine at the C-terminus of each oligopeptide is used to attach it to the trigonal linker via Michael addition to maleimide<sup>31</sup>, the N-terminus is tethered to cholesterol, which has the function of a hydrophobic anchor. As Coarse-Grained Molecular Dynamics simulations indicate, a sponge-like dynamic structure is spontaneously assembled, due to the formation of ion pairs, intense hydrogen bonding, and the occurrence of hydrophobic regions and water-filled nanocavities. For nanosponges from (cholesterol-(K)<sub>20</sub>DEV DGC)<sub>3</sub>-trialeimide / (cholesterol-(D)<sub>20</sub>DEV DGC)<sub>3</sub>-trialeimide units, AFM, TEM and DLS are in principal agreement about the diameter of the nanosponges. Furthermore, all three methods indicate the highly dynamic nature of the sponge-like aggregates, which is in very good agreement with the results obtained from Coarse-Grained Molecular Dynamics. The calculation discussed here predict the relative enrichment of aspartate units at the nanosponges' surfaces. We can observe distinctly stronger staining at the exterior by uranyl acetate of the nanostructures observed in TEM. This is in perfect agreement with the predictions by modelling.

The size of the nanosponges can be adjusted from several micrometers down to approx. 80 nm in diameter, depending on the concentration and the chemical composition (especially chain-

length of the mono-peptides (D or K)) of the supramolecular building blocks. The resulting nanosponges can be generated by simply mixing their components in aqueous buffer. They are stable in size for up to 72h. Therefore, in distinct contrast to classic liposomes, numerous applications can be envisioned in which the nanosponge will be long-term stored in desiccated form and mixed with aqueous buffer immediately before clinical use.

In recent years, cytotherapy has attracted massive attention as a targeting cancer therapy. Cytotherapy uses cancer targeting cells as delivery vehicles to carry therapeutics into the tumor site.<sup>18, 30, 35, 51-53, 55-56</sup> Studies have shown that macrophages are capable of delivering therapeutics to tumors sites.<sup>51-53</sup> We envision entrapping therapeutics into these nanovesicles, and then loading them into neutrophils to achieve targeting delivery. However, the nanosponges themselves have to be non-toxic to ensure high survival rates during transport. Therefore, it is encouraging that virtually no toxic effects have been found during our initial cell proliferation tests with monocyte-macrophage-like cells.

## 1.6 Summary

Nanosponges form spontaneously by mixing two trimeric peptide building blocks, (cholesterol-(K)<sub>n</sub>DEVGDC)<sub>3</sub>-trimaleimide and (cholesterol-(D)<sub>n</sub>DEVGDC)<sub>3</sub>-trimaleimide (n = 5, 10, 15, 20) in aqueous buffers. The resulting sponge-like supramolecular aggregates are long-term stable and do not significantly change their diameter within 72h. Their structure was elucidated with the help of Coarse-Grained Molecular Dynamics. Since the nanosponges were virtually non-toxic in cell experiments with monocyte/macrophage-like cells (RAW264.7 cells), they are promising candidates for drug-delivery to transporting cells in cytototherapy of solid tumors (leucocytes or stem cells). The fundamental features of this novel and structurally unique supramolecular system have been elucidated in this initial study. In further studies, we will investigate the suitability and adaptability of these systems for tailored applications in targeted cancer therapy.

## 1.7 References

1. Cassidy, J.; Schatzlein, A. G., Tumour-targeted drug and gene delivery: principles and concepts. *Expert Rev Mol Med* **2004**, *6* (19), 1-17.
2. Hamad, I.; Moghimi, S. M., Critical issues in site-specific targeting of solid tumours: the carrier, the tumour barriers and the bioavailable drug. *Expert Opin Drug Del* **2008**, *5* (2), 205-219.
3. Moses, M. A.; Brem, H.; Langer, R., Advancing the field of drug delivery: Taking aim at cancer. *Cancer Cell* **2003**, *4* (5), 337-341.
4. Allen, T. M.; Cullis, P. R., Drug delivery systems: Entering the mainstream. *Science* **2004**, *303* (5665), 1818-1822.
5. Tiwari, G.; Tiwari, R.; Sriwastawa, B.; Bhati, L.; Pandey, S.; Pandey, P.; Bannerjee, S. K., Drug delivery systems: An updated review. *Int J Pharm Investig* **2012**, *2* (1), 2-11.
6. Devadasu, V. R.; Bhardwaj, V.; Kumar, M. N. V. R., Can Controversial Nanotechnology Promise Drug Delivery? *Chem Rev* **2013**, *113* (3), 1686-1735.
7. Sawant, R. R.; Torchilin, V. P., Liposomes as 'smart' pharmaceutical nanocarriers. *Soft Matter* **2010**, *6* (17), 4026-4044.
8. Yapa, A. S. B., S. H., Development of Magnetic Theranostic Agents. In *Magnetic Nanomaterials: Applications in Catalysis and Life Sciences*, Bossmann, S. H. W., H., Ed. The Royal Society of Chemistry: London, UK, 2017.
9. Yu, M. X.; Zheng, J., Clearance Pathways and Tumor Targeting of Imaging Nanoparticles. *Acs Nano* **2015**, *9* (7), 6655-6674.
10. Nakamura, Y.; Mochida, A.; Choyke, P. L.; Kobayashi, H., Nanodrug Delivery: Is the Enhanced Permeability and Retention Effect Sufficient for Curing Cancer? *Bioconjugate Chem* **2016**, *27* (10), 2225-2238.
11. Lytton-Jean, A. K.; Kauffman, K. J.; Kaczmarek, J. C.; Langer, R., Cancer nanotherapeutics in clinical trials. *Cancer Treat Res* **2015**, *166*, 293-322.
12. Colletier, J.-P.; Chaize, B.; Winterhalter, M.; Fournier, D., Protein encapsulation in liposomes: efficiency depends on interactions between protein and phospholipid bilayer. *BMC Biotechnol* **2002**, *2*, 9.
13. Glavas-dodov, M.; Fredro-kumbaradzi, E.; Goracinova, K.; Calis, S.; Simonoska, M.; Hincal, A. A., 5-Fluorouracil in topical liposome gels for anticancer treatment - formulation and evaluation. *Acta Pharm. (Zagreb, Croatia)* **2003**, *53* (4), 241-250.

14. Templeton, N. S.; Lasic, D. D.; Frederik, P. M.; Strey, H. H.; Roberts, D. D.; Pavlakis, G. N., Improved DNA: liposome complexes for increased systemic delivery and gene expression. *Nat. Biotechnol.* **1997**, *15* (7), 647-652.
15. Yatvin, M. B.; Weinstein, J. N.; Dennis, W. H.; Blumenthal, R., Design of liposomes for enhanced local release of drugs by hyperthermia. *Science (Washington, D. C.)* **1978**, *202* (4374), 1290-3.
16. Mayer, L. D.; Hope, M. J.; Cullis, P. R., Vesicles of variable sizes produced by a rapid extrusion procedure. *Biochim Biophys Acta* **1986**, *858* (1), 161-8.
17. Olson, F.; Hunt, C. A.; Szoka, F. C.; Vail, W. J.; Papahadjopoulos, D., Preparation of liposomes of defined size distribution by extrusion through polycarbonate membranes. *Biochim. Biophys. Acta, Biomembr.* **1979**, *557* (1), 9-23.
18. Basel, M. T.; Shrestha, T. B.; Troyer, D. L.; Bossmann, S. H., Protease-Sensitive, Polymer-Caged Liposomes: A Method for Making Highly Targeted Liposomes Using Triggered Release. *ACS Nano* **2011**, *5* (3), 2162-2175.
19. Gabizon, A. A.; Shmeeda, H.; Zalipsky, S., Pros and cons of the liposome platform in cancer drug targeting. *J Liposome Res* **2006**, *16* (3), 175-183.
20. van Hell, A. J.; Costa, C. I. C. A.; Flesch, F. M.; Sutter, M.; Jiskoot, W.; Crommelin, D. J. A.; Hennink, W. E.; Mastrobattista, E., Self-Assembly of Recombinant Amphiphilic Oligopeptides into Vesicles. *Biomacromolecules* **2007**, *8* (9), 2753-2761.
21. Holowka, E. P.; Pochan, D. J.; Deming, T. J., Charged Polypeptide Vesicles with Controllable Diameter. *J. Am. Chem. Soc.* **2005**, *127* (35), 12423-12428.
22. Sukthankar, P.; Gudlur, S.; Avila, L. A.; Whitaker, S. K.; Katz, B. B.; Hiromasa, Y.; Gao, J.; Thapa, P.; Moore, D.; Iwamoto, T.; Chen, J.; Tomich, J. M., Branched Oligopeptides Form Nanocapsules with Lipid Vesicle Characteristics. *Langmuir* **2013**, *29* (47), 14648-14654.
23. Sukthankar, P.; Whitaker, S. K.; Garcia, M.; Herrera, A.; Boatwright, M.; Prakash, O.; Tomich, J. M., Thermally induced conformational transitions in nascent branched amphiphilic peptide capsules. *Langmuir* **2015**, *31* (10), 2946-2955.
24. Avila, L. A.; Aps, L. R. M. M.; Sukthankar, P.; Ploscariu, N.; Gudlur, S.; Simo, L.; Szoszkiewicz, R.; Park, Y.; Lee, S. Y.; Iwamoto, T.; Ferreira, L. C. S.; Tomich, J. M., Branched Amphiphilic Cationic Oligopeptides Form Peptiplexes with DNA: A Study of Their Biophysical Properties and Transfection Efficiency. *Mol. Pharmaceutics* **2015**, *12* (3), 706-715.
25. Jia, Z.; Whitaker, S. K.; Tomich, J. M.; Chen, J., Organization and Structure of Branched Amphipathic Oligopeptide Bilayers. *Langmuir* **2016**, *32* (38), 9883-9891.

26. Danhier, F., To exploit the tumor microenvironment: Since the EPR effect fails in the clinic, what is the future of nanomedicine? *J Control Release* **2016**, *244*, 108-121.
27. Si, J. X.; Shao, S. Q.; Shen, Y. Q.; Wang, K., Macrophages as Active Nanocarriers for Targeted Early and Adjuvant Cancer Chemotherapy. *Small* **2016**, *12* (37), 5108-5119.
28. Rachakatla, R. S.; Balivada, S.; Seo, G.-M.; Myers, C. B.; Wang, H.; Samarakoon, T. N.; Dani, R.; Pyle, M.; Kroh, F. O.; Walker, B.; Leaym, X.; Koper, O. B.; Chikan, V.; Bossmann, S. H.; Tamura, M.; Troyer, D. L., Attenuation of Mouse Melanoma by A/C Magnetic Field after Delivery of Bi-Magnetic Nanoparticles by Neural Progenitor Cells. *ACS Nano* **2010**, *4* (12), 7093-7104.
29. Heathman, T. R. J.; Nienow, A. W.; McCall, M. J.; Coopman, K.; Kara, B.; Hewitt, C. J., The translation of cell-based therapies: clinical landscape and manufacturing challenges. *Regen Med* **2015**, *10* (1), 49-64.
30. Basel, M. T.; Shrestha, T. B.; Bossmann, S. H.; Troyer, D. L., Cells as delivery vehicles for cancer therapeutics. *Therapeutic delivery* **2014**, *5* (5), 555-67.
31. Fontaine, S. D.; Reid, R.; Robinson, L.; Ashley, G. W.; Santi, D. V., Long-Term Stabilization of Maleimide-Thiol Conjugates. *Bioconjugate Chem.* **2015**, *26* (1), 145-152.
32. Linder, M.; Tschernig, T., Vasculogenic mimicry: Possible role of effector caspase-3, caspase-6 and caspase-7. *Ann Anat* **2016**, *204*, 114-7.
33. Rich, D. H.; Gesellchen, P. D.; Tong, A.; Cheung, A.; Buckner, C. K., Alkylating derivatives of amino acids and peptides. Synthesis of N-maleoylamino acids, [1-(N-maleoylglycyl)cysteinyl]oxytocin, and [1-(N-maleoyl-11-aminoundecanoyl)cysteinyl]oxytocin. Effects on vasopressin-stimulated water loss from isolated toad bladder. *J. Med. Chem.* **1975**, *18* (10), 1004-10.
34. Pieken, W.; Hill, K.; Eaton, B.; McGee, D.; Vagle, K.; Gold, L.; Stephens, A. Conjugating macromolecules using cycloaddition reactions. US6737236B1, 2004.
35. Wang, H.; Shrestha, T. B.; Basel, M. T.; Dani, R. K.; Seo, G.-M.; Balivada, S.; Pyle, M. M.; Prock, H.; Koper, O. B.; Thapa, P. S.; Moore, D.; Li, P.; Chikan, V.; Troyer, D. L.; Bossmann, S. H., Magnetic-Fe/Fe<sub>3</sub>O<sub>4</sub>-nanoparticle-bound SN38 as carboxylesterase-cleavable prodrug for the delivery to tumors within monocytes/macrophages. *Beilstein J. Nanotechnol.* **2012**, *3*, 444-455, 12 pp.
36. Coin, I.; Beyermann, M.; Bienert, M., Solid-phase peptide synthesis: from standard procedures to the synthesis of difficult sequences. *Nat. Protoc.* **2007**, *2* (12), 3247-3256.
37. Cheronis, J. C.; Whalley, E. T.; Nguyen, K. T.; Eubanks, S. R.; Allen, L. G.; Duggan, M. J.; Loy, S. D.; Bonham, K. A.; Blodgett, J. K., A new class of bradykinin antagonists: synthesis and in vitro activity of bissuccinimidoalkane peptide dimers. *J. Med. Chem.* **1992**, *35* (9), 1563-72.

38. Perera, A. S.; Wang, H.; Basel, M. T.; Pokhrel, M. R.; Gamage, P. S.; Kalita, M.; Wendel, S.; Sears, B.; Welideniya, D.; Liu, Y.; Turro, C.; Troyer, D. L.; Bossmann, S. H., Channel Blocking of MspA Revisited. *Langmuir* **2013**, *29* (1), 308-315.
39. <https://mai.ku.edu/about-mai-lab> (accessed 01/31/2017).
40. Oostenbrink, C.; Villa, A.; Mark, A. E.; Van Gunsteren, W. F., A biomolecular force field based on the free enthalpy of hydration and solvation: The GROMOS force-field parameter sets 53A5 and 53A6. *Journal of Computational Chemistry* **2004**, *25* (13), 1656-1676.
41. Malde, A. K.; Zuo, L.; Breeze, M.; Stroet, M.; Poger, D.; Nair, P. C.; Oostenbrink, C.; Mark, A. E., An Automated Force Field Topology Builder (ATB) and Repository: Version 1.0. *Journal of Chemical Theory and Computation* **2011**, *7* (12), 4026-4037.
42. Monticelli, L.; Kandasamy, S. K.; Periole, X.; Larson, R. G.; Tieleman, D. P.; Marrink, S.-J., The MARTINI Coarse-Grained Force Field: Extension to Proteins. *Journal of Chemical Theory and Computation* **2008**, *4* (5), 819-834.
43. Marrink, S. J.; Risselada, H. J.; Yefimov, S.; Tieleman, D. P.; de Vries, A. H., The MARTINI Force Field: Coarse Grained Model for Biomolecular Simulations. *The Journal of Physical Chemistry B* **2007**, *111* (27), 7812-7824.
44. Stockert, J. C.; Blazquez-Castro, A.; Canete, M.; Horobin, R. W.; Villanueva, A., MTT assay for cell viability: Intracellular localization of the formazan product is in lipid droplets. *Acta Histochem.* **2012**, *114* (8), 785-796.
45. Bhattacharjee, S., DLS and zeta potential - What they are and what they are not? *J. Controlled Release* **2016**, *235*, 337-351.
46. <https://imagej.nih.gov/nih-image/>.
47. Chou, P. Y.; Scheraga, H. A., Calorimetric measurement of enthalpy change in the isothermal helix-coil transition of poly-L-lysine in aqueous solution. *Biopolymers* **1971**, *10* (4), 657-680.
48. Pivcova, H.; Saudek, V., <sup>13</sup>C nmr relaxation study of poly (aspartic acid). *Polymer* **1985**, *26* (5), 667-672.
49. Saudek, V.; Stokrova, S.; Schmidt, P., Conformational Study of Poly(Alpha-L-Aspartic Acid). *Biopolymers* **1982**, *21* (6), 1011-1020.
50. Ismail, A. A.; Mantsch, H. H., Salt bridge induced changes in the secondary structure of ionic polypeptides. *Biopolymers* **1992**, *32* (9), 1181-1186.
51. Basel, M. T.; Balivada, S.; Shrestha, T. B.; Seo, G.-M.; Pyle, M. M.; Tamura, M.; Bossmann, S. H.; Troyer, D. L., A Cell-Delivered and Cell-Activated SN38-Dextran

- Prodrug Increases Survival in a Murine Disseminated Pancreatic Cancer Model. *Small* **2012**, *8* (6), 913-920.
52. Seo, G.-M.; Rachakatla, R. S.; Balivada, S.; Pyle, M.; Shrestha, T. B.; Basel, M. T.; Myers, C.; Wang, H.; Tamura, M.; Bossmann, S. H.; Troyer, D. L., A self-contained enzyme activating prodrug cytotherapy for preclinical melanoma. *Mol. Biol. Rep.* **2012**, *39* (1), 157-165.
  53. Basel, M. T.; Balivada, S.; Wang, H.; Shrestha, T. B.; Seo, G. M.; Pyle, M.; Abayaweera, G.; Dani, R.; Koper, O. B.; Tamura, M.; Chikan, V.; Bossmann, S. H.; Troyer, D. L., Cell-delivered magnetic nanoparticles caused hyperthermia-mediated increased survival in a murine pancreatic cancer model. *Int. J. Nanomed.* **2012**, *7*, 297-306.
  54. Lehner, R.; Wang, X.; Marsch, S.; Hunziker, P., Intelligent nanomaterials for medicine: Carrier platforms and targeting strategies in the context of clinical application. *Nanomedicine (N. Y., NY, U. S.)* **2013**, *9* (6), 742-757.
  55. Shrestha, T. B.; Seo, G. M.; Basel, M. T.; Kalita, M.; Wang, H.; Villanueva, D.; Pyle, M.; Balivada, S.; Rachakatla, R. S.; Shinogle, H.; Thapa, P. S.; Moore, D.; Troyer, D. L.; Bossmann, S. H., Stem cell-based photodynamic therapy. *Photochem. Photobiol. Sci.* **2012**, *11* (7), 1251-1258.
  56. Alshetaiwi, H. S.; Balivada, S.; Shrestha, T. B.; Pyle, M.; Basel, M. T.; Bossmann, S. H.; Troyer, D. L., Luminol-based bioluminescence imaging of mouse mammary tumors. *J. Photochem. Photobiol., B* **2013**, *127*, 223-228.

## **Chapter 2 - Peptide Nanosponges Designed for Rapid Uptake by Stem Cells and Leukocytes**

### **2.1 Abstract**

The structure of novel binary nanosponges consisting of cholesterol-(K/D)<sub>n</sub>DEVGDC)<sub>3</sub>-trimaleimide units possessing a trigonal maleimide linker, to which either lysine (K)<sub>20</sub> or aspartic acid (D)<sub>20</sub> are tethered, has been elucidated by means of TEM. A high degree of agreement between these findings and structure predictions through explicit solvent and then coarse-grained molecular dynamics (MD) simulations has been found. Based on the nanosponges' structure and dynamics, caspase-6 mediated release of the model drug 5(6)-carboxyfluorescein has been demonstrated. Furthermore, the binary (DK20) nanosponges have been found virtually non-toxic in cultures of neural progenitor cells. Additionally, DK20 nanosponges were taken up efficiently by leucocytes (WBC) in peripheral blood within 3h of exposure. The percentage of live cells among the WBC was not significantly decreased by the DK20 nanosponges. Therefore, this novel material holds great promise for improved cell-mediated therapy.

## 2.2 Background

One of the grand challenges in nanomedicine is the effective targeting of tumors and metastases.<sup>1</sup> For almost a generation, Enhanced Permeation and Retention (EPR)<sup>2-3</sup>, the passive diffusion of nanosize delivery vehicles (e.g. vesicles<sup>4</sup>, liposomes<sup>5</sup>, exosomes<sup>6</sup>, nanoparticles<sup>7</sup>, polymer-based nanostructures<sup>8-10</sup>) through gaps in the vasculature that have been built rapidly around tumor tissue, has been hailed as an important breakthrough in the fight against cancer. Unfortunately, emerging evidence clearly suggests that the EPR effect works well in rodent models (especially in nude mice), but not in humans, which feature a distinctly different vasculature and, compared to rodents, significantly slower tumor growth.<sup>2-3, 11</sup> Therefore, alternative targeting approaches are urgently needed. Active targeting strategies use either antibodies<sup>12-14</sup>, antibody-fragments<sup>15-17</sup>, peptide sequences<sup>15-16, 18</sup> or aptamers<sup>15-16</sup>, which are capable of targeting receptors that are overexpressed in solid tumors, as for instance members of the integrin family<sup>19-20</sup>. However, active targeting processes can be impaired by physiological barriers, such as high interstitial fluid pressures and the formidable physical barrier imposed by tumor stroma.<sup>21</sup> Therefore, cell-mediated transport of anticancer drugs into the tumor tissue is, in the opinion of the authors, the most viable strategy to develop intelligent alternatives to chemotherapy.<sup>10, 22-27</sup> Transport cells have the ability to migrate to tumors and metastases following cytokine/chemokine gradients.<sup>28</sup> Among them are stem cells<sup>29</sup>, monocytes/macrophages<sup>30-31</sup> and neutrophils.<sup>32-33</sup> Neural stem cells, which can be, principally, cultured and matched to patient-types, have been successfully utilized for cell-mediated therapies in rodent models<sup>22, 27, 34</sup>, as well as neutrophils<sup>35</sup> and monocytes<sup>10, 23-24, 27</sup>. The use of autologous cells has the potential of developing truly patient specific therapies, and also of significantly lowering the regulatory barriers for cell-based human cancer therapies.<sup>36</sup> Targeting neutrophils

and monocytes in peripheral blood will avoid the necessity for their time-consuming isolation and culturing, and further reduce the regulatory hurdles since cell isolation is not necessary. In Figure 2.1, the principles of cell based cancer therapy are shown. In step 1, the selected transport cell type is targeted. This step has to be efficient in order to maintain high cell viabilities. Furthermore, the vector that is used to facilitate uptake has to be virtually non-toxic. After the cells have been returned to the host, they actively migrate to tumors and metastases following cytokine/chemokine gradients. The last step consists in the triggered release of the payload and uptake of the latter by the tumor and stromal cells.<sup>27</sup>

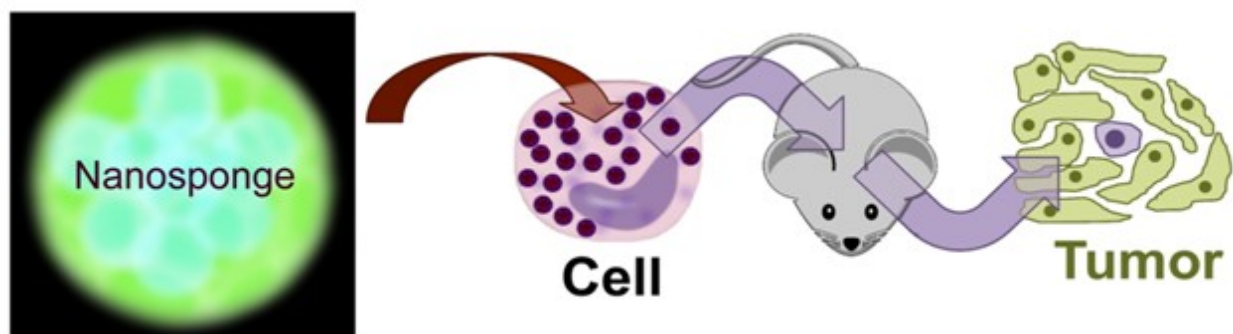


**Figure 2.1 Principles of cell therapy utilizing nanosponges. Neutrophils in peripheral blood will be loaded by targeting them with peptide nanosponges. After the blood has been given back intravenously to the patient, the neutrophils will home to tumors within 6-12h. Alternatively, neural stem cells can be cultured, loaded with peptide nanosponges and injected intravenously into the patient.**

Chapter 1 describes the design, synthesis, and characterization of designer peptide-nanosponges for efficient uptake by delivery cells in drug delivery.<sup>37</sup> Their supramolecular building blocks consist of cholesterol-(K/D)<sub>n</sub>DEV DGC)<sub>3</sub>-trialeimide units featuring a trigonal maleimide linker to which either lysine (K)<sub>20</sub> or aspartic acid (D)<sub>20</sub> are attached. Furthermore, a consensus sequence for caspase-6 (DE-VDGC) is integrated into the structures. Both, (cholesterol-(K)<sub>20</sub>DEV DGC)<sub>3</sub>-trialeimide and mixtures of (cholesterol-(K)<sub>20</sub>DEV DGC)<sub>3</sub>-trialeimide and cholesterol-(D)<sub>20</sub>DEV DGC)<sub>3</sub>-trialeimides form stable nanosponges (short

notation: DK20). The structure of the novel nanosponges was investigated through explicit solvent and then coarse-grained molecular dynamics (MD) simulations. As Figure 2.2 indicates, the nanosponge structure is featuring aspartate- and lysine-rich regions, together with cholesterol domains and (aqueous) solvent filled nanoholes. The resulting structure is fluctuating, depending on the temperature. Upon mixing with aqueous buffers, long-term stable (up to 72h have been experimentally determined) DK20 nanosponges are immediately formed, which possess very low polydispersities. They are capable of incorporating the hydrophobic cyanine 3.0-dye PKH26.

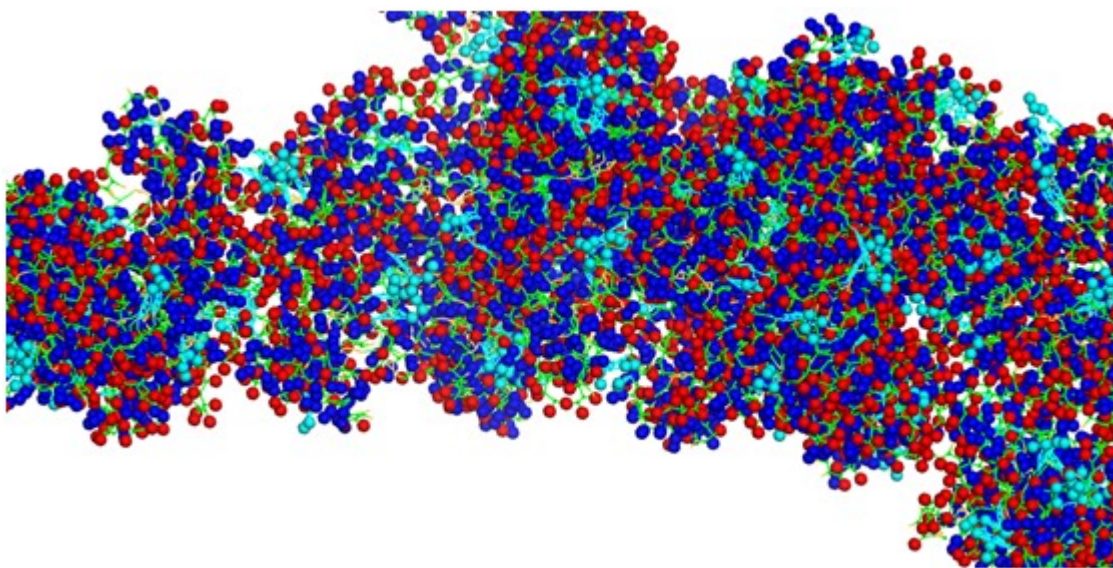


**Figure 2.2 Typical structure of a nanosponge according to molecular dynamics (MD) simulations.<sup>37</sup> Red: aspartate groups, blue: lysine groups, cyan: cholesterol aggregates, green: peptide backbone.**

In order to function properly, the nanosponges have been taken up quickly by the transport cells, transported to the tumor sites, and then released. The latter will be achieved by means of programmed cell death (apoptosis), which will occur naturally in neutrophils 12 to 24h after reaching the tumor environment<sup>38</sup>, or by means of triggered apoptosis (macrophages and neural stem cells<sup>27</sup>). Caspase activation is the hallmark of apoptosis.<sup>39</sup> We will utilize caspases, which are proteolytic enzymes, to activate the nanosponges for drug delivery purposes.

In this chapter, we will describe refined structural investigations by TEM, *in-vitro* release studies of the model drug carboxyfluorescein by caspase-6 activation, as well as cell targeting experiments of cultured neural stem cells and leucocytes in peripheral (pig) blood. The data obtained from these experiments will demonstrate the unique properties of type DK20 nanosponges.

## **2.3 Methods**

### **2.3.1 Synthesis and Characterization of the Nanosponges**

The synthesis of all building blocks required for the assembly of DK20 and K20 nanosponges, as well as their characterization by NMR and MALDI-TOF has been described in chapter 1.<sup>37</sup>

### **2.3.2 TEM Characterization**

Samples for transmission electron microscopy (TEM) were prepared by dropping 10  $\mu$ L of 0.050 mM type DK20 solution in PBS directly on a glow discharged TEM grid. Uranyl acetate was used as a positive staining agent in a part of the TEM experiments. In all cases electron microscopy was performed at an accelerating voltage of 200 kV. Nanosponge morphology on HOPG was examined by bright-field and dark-field transmission electron microscopy (TEM) using a FEI Technai G<sub>2</sub> transmission electron microscope at an electron acceleration voltage of 200 kV. Dark-field TEM did not reveal a characteristic diffraction pattern. High resolution images were captured using a standardized, normative electron dose and a constant defocus value from the carbon-coated surfaces. All TEM measurements were performed at the Microscopy and Analytical Imaging Laboratory of the University of Kansas.<sup>40</sup>

### **2.3.3 Nanosponge Formation and DLS Characterization**

The hydrodynamic diameter and polydispersity index (PDI) of the formed nanosponges were measured by dynamic light scattering (DLS, ZetaPALS, Brookhaven Instruments Corp., Holtsville, NY). All measurements were carried out at 25 °C, with 658 nm laser wavelength, and

90 degree detection angle. Data were collected from an average of three measurements over 60 seconds.

### **2.3.4 Carboxyfluorescein Encapsulation**

Equal molar ratios of (cholesterol-(K)<sub>20</sub>DEV DGC)<sub>3</sub>-trimaleimide and (cholesterol-(D)<sub>20</sub>DEV DGC)<sub>3</sub>-trimaleimide ( $5.0 \times 10^{-4}$  M of each component) were dissolved in 10  $\mu$ M carboxyfluorescein PBS (pH=7.4) solution. After incubating at room temperature for 2 hours, the solution was transferred to a 3,500 Da molecular weight cutoff dialysis bag. Free carboxyfluorescein was removed by means of continuous dialysis against 1 $\times$  PBS buffer until virtually no fluorescence could be detected in the solution using a Fluoromax-2 spectrometer. Using a fluorescence calibration curve, it was estimated that the concentration of free carboxyfluorescein was < 1 nM. At this point, a dark red color was still retained inside the dialysis bag. This finding provided a good indication that carboxyfluorescein had been trapped inside the peptide nanosponges. From the integrated UV/Vis-absorption of the dialysis solution we have estimated that  $65 \pm 4$  mol % of carboxyfluorescein was encapsulated in the procedure. After lyophilizing to dryness, a yellow/brown powder was obtained, which could be easily re-dispersed in PBS by vortexing for 5 min. In a subsequent dialysis experiment, it was found that virtually no carboxyfluorescein was leached after 24, 48, and 72h. The UV/Vis and fluorescence spectra of carboxyfluorescein, as well as the fluorescence calibration curve as a function of carboxyfluorescein concentration can be found in the Appendix B.2 and B.3.

### **2.3.5 Caspase-6 Triggered Dye Release**

The dye release experiment was performed using a fluorescence plate reader (BioTek Synergy H1). 200  $\mu\text{L}$  of carboxyfluorescein loaded nanosponges in PBS solution (0.20 mg/mL) were added to each well of a 96-well black clear-bottom plate. To each control well, 10  $\mu\text{L}$  of PBS buffer was added, and to each experimental well, 10  $\mu\text{L}$  of caspase-6 PBS solution (0.1  $\mu\text{g}/\text{mL}$ ,  $5.5 \times 10^{-9}$  M, Enzo LifeSciences) was added. The plate was incubated at 37  $^{\circ}\text{C}$ , the fluorescence intensity at 520 nm was recorded every 5 min. The experiments were repeated 5 times and p-values calculated, as described in the literature.<sup>41</sup>

### **2.3.6 Cell Experiments and MTT Assays**

The cytotoxicity of the PKH26 containing nanosponges was assessed by utilizing the MTT assay<sup>42</sup> on C17.2 neural progenitor cells (NPCs)<sup>34</sup>, which were a gift from Dr. V. Ourednik (Iowa State University) to Dr. D. L. Troyer, DVM (Kansas State University, Anatomy & Physiology). NPCs were originally developed by Dr. Evan Snyder.<sup>43</sup> These cells were maintained in DMEM supplemented with 10% FBS (Sigma-Aldrich), 5% horse serum (Invitrogen), 1% glutamine (Invitrogen), and 1% penicillin/streptomycin (Invitrogen). PKH26 is a hydrophobically modified cyanine 3.0 dye. The preparation of PKH26-loaded type DK20 nanosponges was described earlier in chapter 1.<sup>37</sup> Cell experiments were carried out in the culturing medium described above. The percentage of viable cells was determined after 24 and 48 hours of incubation. Cells were seeded in T-25 flask. After 24 h of incubation at 37  $^{\circ}\text{C}$ , cells were re-plated in a 96 well plate at 20000/cm<sup>2</sup> density and further incubated for 24 h at 37<sup>0</sup>C to obtain 80 % confluency before the nanosponges were added.

Concentration series of type DK20 nanosponges (0.0, 0.1, 0.2, 0.5, 1.0, 2.0, 5.0, 10, 20, 40, 60, 80, 100  $\mu\text{moles L}^{-1}$  in total, molar ratio 1:1) were prepared by dissolving the nanosponge components in the same media that were used for culturing the cells. Cells were incubated for 24/48 h at 37 °C. Eight replicates were prepared for each concentration. A portion of 10  $\mu\text{L}$  of MTT reagent (5 mg/ml in PBS) was added to each well, and the plates were incubated for another 4 h at 37 °C. Finally, 100  $\mu\text{L}$  of 10% sodium dodecyl sulfate in 0.010M HCl was added into each well and incubated for 24 h at 37 °C. Their absorbance was recorded by using a plate reader at 550nm and 690nm. PBS solution was used as control for all the experiments. The solution with of  $\mu\text{mole L}^{-1}$  of nanosponge served as control.

Murine stem cells were imaged by using a Zeiss, Axiovert 40 CFL microscope with darkfield, brightfield, phase contrast and epifluorescence illumination, a camera system and Jenoptik, ProgRes C3 Cool camera and a ProgRes Capture Pro 2.10.0.0 software.

### **2.3.7 Cell Uptake from Peripheral Blood**

Cattle blood was obtained at the Kansas State feed lot. Blood was collected in citrated (0.105M) 4.5ml tubes (BD Vacutainer, Franklin Lakes, NJ, USA). The collected blood was pooled and split into 3.0 ml samples. Samples were supplemented with 1.0 ml of serum containing RPMI medium to ensure supply of nutrients. The samples were incubated with 1.0 ml of 1.0 mg/ml type DK 20 nanosponges in PBS at 37°C. Leukocytes (WBC) were extracted via removal of the buffy coat after centrifugation.<sup>44-45</sup> Red Blood Cell Lysis Buffer (Sigma-Aldrich, St. Louis, MO, USA) was used to remove any remaining red blood cells and the samples were washed with PBS (10 min, 500g). Cells were counted via hemocytometer and diluted to achieve a concentration of  $5 \times 10^5$  cells/ml, suitable for analysis by flow cytometry (Guava EasyCyte,

EMD Millipore). To evaluate the loading of type DK20 nanosponges over time, PKH26 fluorescent dye modified nanosponges were used and red fluorescence intensity was detected. Thresholds were set using unmodified extracted WBC. The survival of WBC incubated type DK20 nanosponges was detected with a Annexin V / Propidium Iodine apoptosis kit (Novus Biologicals). The protocol provided with the kit was exactly followed.<sup>46</sup> The procedure was carried out five times and p-values were calculated.<sup>41</sup>

## 2.4 Results

### 2.4.1 TEM-Analysis of the Nanosponge Structure

Bright field transmission electron microscopy was able to reveal structures that are formed after depositing the nanosponges directly onto HOPG grids and exposing them to the high vacuum inside the TEM. The flattened nanosponges contain dark spots, which are indicative of water/buffer-filled pockets inside the structure. Furthermore, after applying a black/white correction filter function available in Adobe Photoshop, brighter than average spots can be discerned within the nanosponge structure, which are indicative of cholesterol-rich regions. The average grey within the structure shown on Figure 2.3B suggests the presence of both, lysine and aspartate-rich regions, which retain some of their water-content in high vacuum. These findings are in excellent agreement with the principal results of the molecular dynamics (MD) simulations of nanosponge structure.<sup>37</sup>

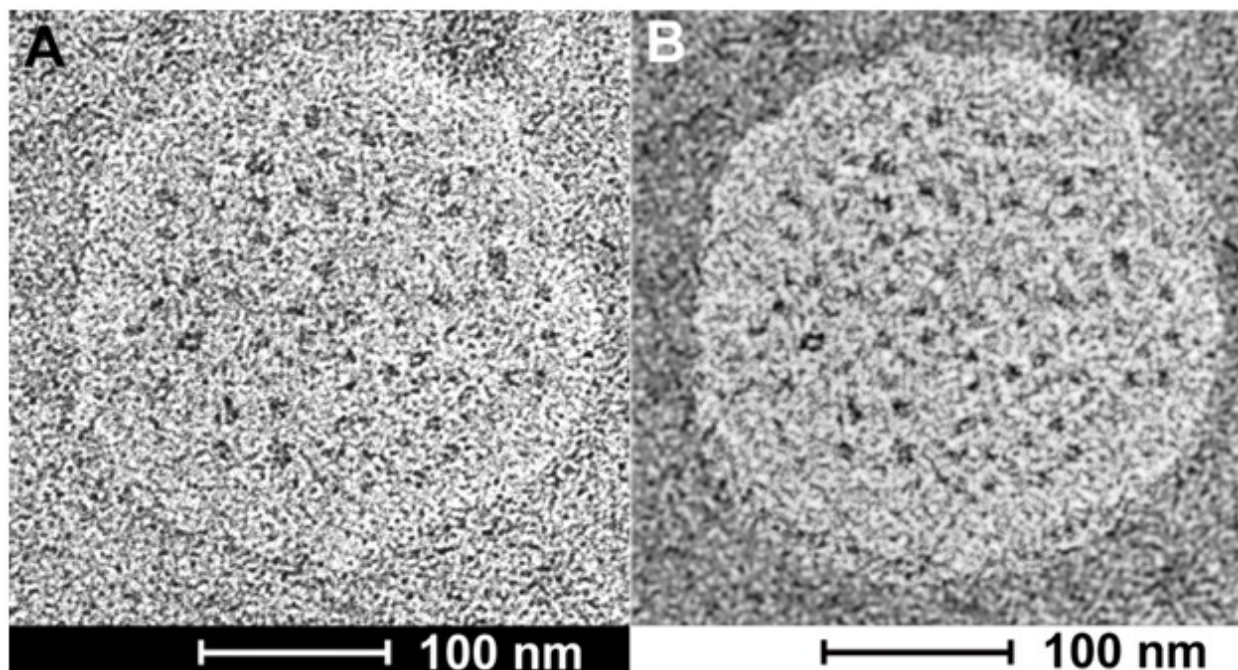


**Figure 2.3 A:** TEM image of type DK20 nanosponges on HOPG, as deposited from PBS solution. No staining agent was employed. **A:** Bright field transmission TEM (200 kV) of a type DK 20 nanosponge. Water-filled vesicles are discernible as dark spots within the bright nanosponge. **B:** Same image as in 4A after black/white correction filter function in Photoshop.

It is noteworthy that the nanosponges obtained under the experimental conditions described here appear to be larger ( $240 \pm 30$  nm in diameter), whereas their diameter reported earlier was  $90 \pm 15$  nm.<sup>37</sup> However, an about five times lower type DK20 concentration and no uranyl staining was used for recording the TEM imaging shown in Figure 2.3.

#### **2.4.2 Caspase-6 Triggered Carboxyfluorescein Release**

Carboxyfluorescein is a fluorescent dye, which has been used for microscopy and cell-tracking purposes. It is established that at increased concentrations, carboxyfluorescein undergoes intense self-quenching. A detailed investigation of the concentration-dependent quenching of carboxyfluorescein in liposomes revealed both, monomer-monomer and monomer-

dimer energy transfer processes.<sup>47</sup> Carboxyfluorescein dimers are non-fluorescent. Because carboxyfluorescein fluorescence can increase as function of decreasing dye concentration, it has become a popular probe detecting drug release from a delivery system.<sup>9, 48-49</sup> After entrapping carboxyfluorescein into type DK20 peptide nanospheres and subsequent lyophilizing to dryness, the obtained solid was dissolved in 3.0 mL PBS buffer (pH=7.4). DLS measurements showed that the hydrodynamic diameter was  $213 \pm 25$  nm before adding caspase-6 (see Appendix B.4). The nanospheres remained stable during 24h. The dye release experiment showed  $18 \pm 1$  % of fluorescence increase in the caspase-6 group during the first hour. During the same time interval, only 1.6% fluorescence increase was observed in the control group, which was within the margin of error ( $\pm 0.88$  %). Longer incubation time did not lead to significant further fluorescence increase. The results of this experiment provided a strong indication that the encoded DE-VDGC peptide sequence in the nanosphere is cleaved by caspase-6. This proteolytic process led to a disruption of the nanosphere and consequent release of the entrapped fluorescent dye.

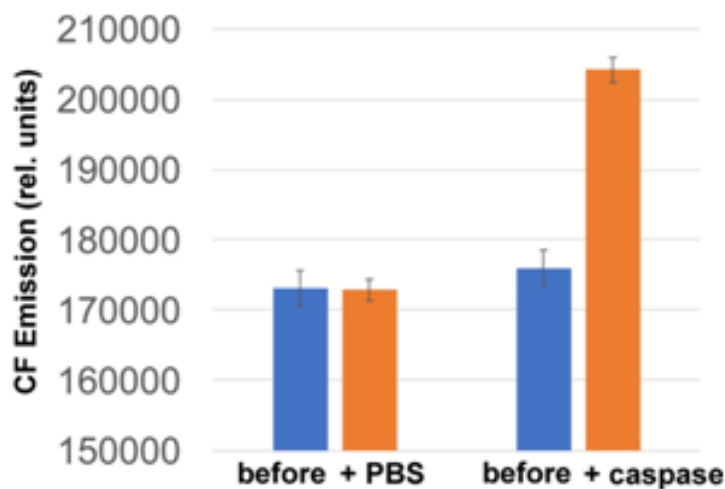


**Figure 2.4 Caspase-6 triggered carboxyfluorescein (CF) release.** Type DK20 nanospheres containing carboxyfluorescein were incubated with PBS (control) or  $2.60 \times 10^{-10}$  M caspase-6 in PBS at 37 °C. The observed fluorescence emission was recorded at 515 nm with a 5nm bandpass filter,  $\lambda_{exc} = 493$  nm.

### 2.4.3 TEM-Analysis of Caspase-6 Activation

Bright field TEM was also successfully used to visualize the effect of caspase-6 activation of nanosponges. In Figure 2.5, a sequence of three TEM images is shown: **A:** 0.20 mg/mL of carboxyfluorescein-loaded DK20 nanosponges (CF-DK20), deposited from PBS dispersion onto HOPG. **B:** 0.20 mg/mL of CF-DK20 nanosponges after 15 min of incubation at 37°C with commercially available caspase-6 ( $2.60 \times 10^{-10}$  M), deposited from PBS dispersion onto HOPG. **C:** 0.20 mg/mL of CF-DK20 nanosponges after 60 min of incubation at 37°C with commercially available caspase-6 ( $2.60 \times 10^{-10}$  M), deposited from PBS dispersion onto HOPG. TEM images were recorded immediately after the deposition of the (reactive) nanosponges on the carbon surfaces. Uranyl staining was added shortly before depositing the dispersions onto HOPG.

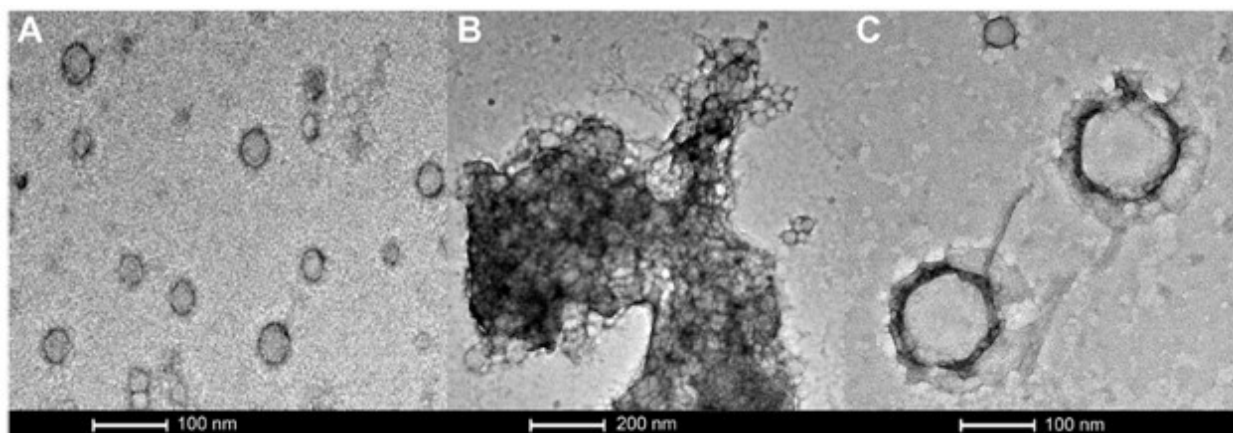


**Figure 2.5 Bright field TEM (200 kV) of 0.20 mg/mL of carboxyfluorescein-loaded DK20 nanosponges: A: Nanosponges deposited from PBS before adding caspase-6. B: Reactive mixture deposited from PBS containing caspase-6 ( $2.60 \times 10^{-10}$  M) after 15 min. of reaction at 37°C. C: Novel nanostructures, which were formed in the reaction, deposited from PBS containing caspase-6 ( $2.60 \times 10^{-10}$  M) after 60 min. of reaction at 37°C.**

As it is shown in Figure 2.5, CF-DK20 nanosponges were digested by caspase-6, followed by the formation of a novel supramolecular structure by the products of this enzymatic reaction. The nanosponges shown in Figure 2.5A differ again in size from the structure shown in Figure

2.3 and DK20 nanosponges, which were previously discussed in chapter 1.<sup>37</sup> The reasons for this observation are that the concentrations used in the TEM experiment very closely resemble the ones from the caspase-6-triggered carboxyfluorescein release, but are different from previous TEM experiments. Furthermore, we have observed that the presence of a charged molecule (here: 5(6)-carboxyfluorescein) within the DK20 framework will influence the size of the formed aggregates. Moreover, the spherical nanosponges are deposited onto a carbon surface for the purpose of TEM. This will flatten their structures to a 2D coating and, at least partially, lead to the orientation of the hydrophobic cholesterol labels towards the carbon surface. Therefore, in opposite to dynamic light scattering, the nanosponges' structure will be somewhat distorted by the procedures necessary to record TEM.

In Figure 2.5B the originally observed organic structures have completely vanished and a mesh of organic structures has formed. It is our interpretation of this observation that caspase-6 was able to cleave at least a fraction of the DE-VDGC, thus disrupting the structure of the nanosponges. Enzymatic cleavage releases cholesterol-K<sub>20</sub>-DE and cholesterol-D<sub>20</sub>-DE units. According to the results shown in Figure 2.5C, these units (or at least cholesterol-K<sub>20</sub>-DE) are able to form novel supramolecular structures. The re-formation of well-ordered structures may be responsible for the observed release of “only” about 18% of carboxyfluorescein, which was observed by means of quantitative fluorescence recording. Interestingly, the supramolecular structures formed after 1h of “digestion” with caspase-6 ( $2.60 \times 10^{-10}$  M) are larger than the original nanosponges.

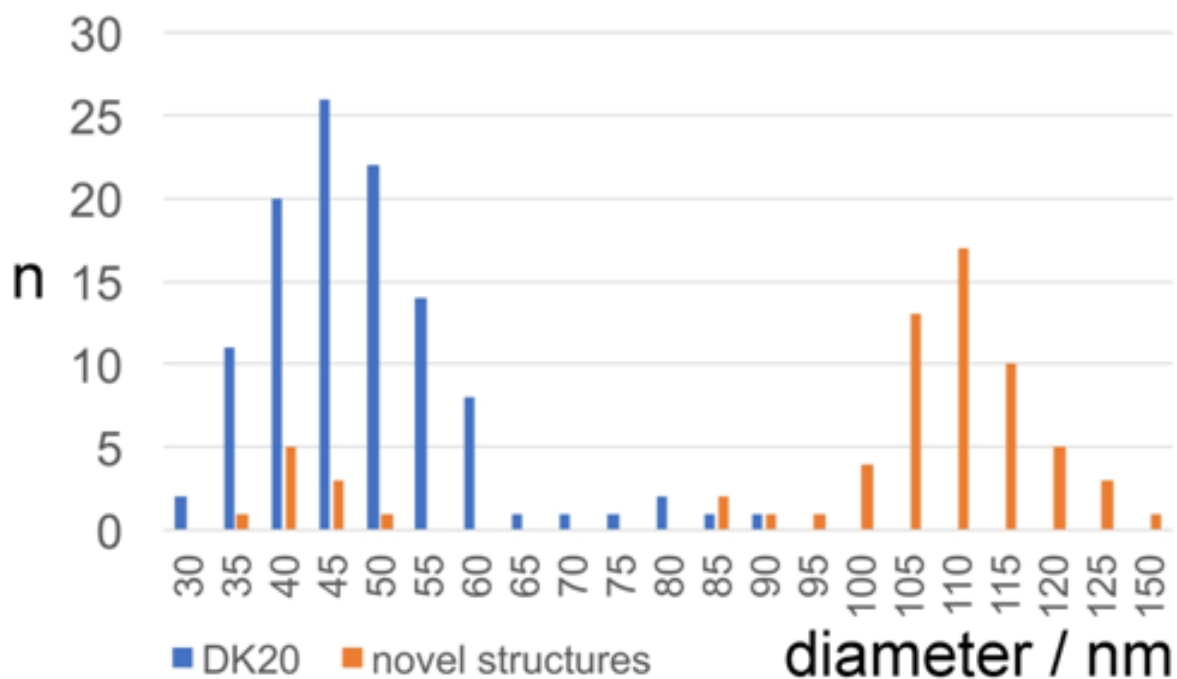


**Figure 2.6** Size distribution of carboxyfluorescein-loaded DK20 nanosponges before and after “digestion” with caspase-6 (see text, and Figures 2.4 and 2.5 for further explanation)

#### 2.4.4 Cell Toxicity of the Peptide Nanosponges

We have performed classic MTT cell proliferation assays<sup>10, 23-24, 50</sup> to determine the cell viability of murine C17.2 neural progenitor cells (NPCs)<sup>34</sup> after incubation with PKH26-containing DK20 nanosponges. As Figure 2.7 demonstrates, the DK20 nanosponges are not toxic to NPCs, even at concentrations as large as 100  $\mu$ M.

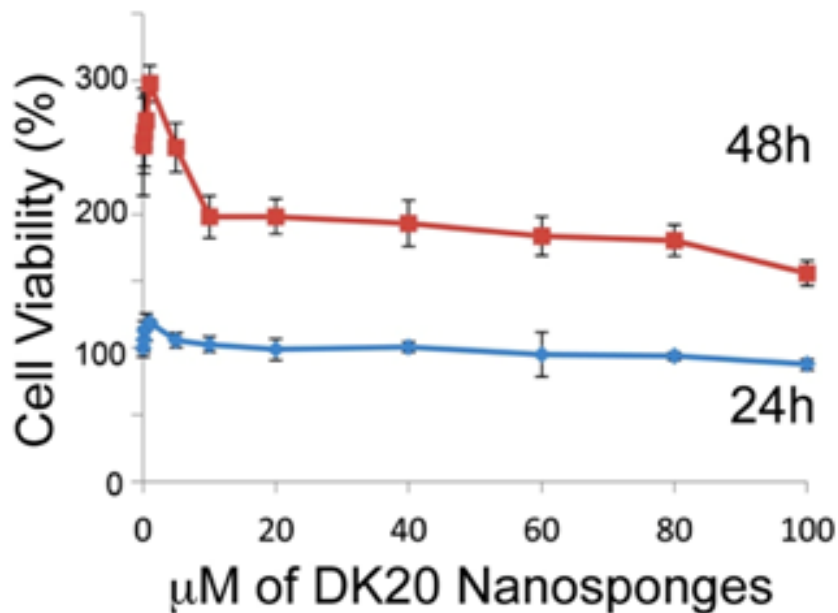


**Figure 2.7** Cell viability of C17.2 neural progenitor cells (NPCs) as a function of DK20 nanosponge concentration and incubation time (24h and 48h), as measured by the MTT assay.<sup>10, 23-24, 50</sup> Nanosponges were added to the cell culture medium in their respective concentrations (see methods section). The cell viability after 24h in the absence of DK20 nanosponge was used as reference to calculate all other viabilities.

#### 2.4.5 Nanosponge-Uptake Kinetics by Leucocytes in Peripheral Blood

Cell Uptake Kinetics were recorded to determine the uptake efficiencies of the peptide nanosponges by neutrophils and monocytes/macrophages in peripheral blood. The results are summarized in Table 2.1 and Figure 2.8. They indicate that the targeting of defensive cells within peripheral blood, followed by cell-based transport to the tumor site, is a feasible treatment strategy.

	DK20 Nanosponges					
	30 min		3 h		6 h	
	Neutrophils loaded	Monocytes/Macrophages loaded	Neutrophils loaded	Monocytes/Macrophages loaded	Neutrophils loaded	Monocytes/Macrophages loaded
Average	4.3%	22.6%	19.5%	49.4%	25.0%	54.0%
StDev	2.4%	6.0%	5.4%	14.8%	17.3%	19.7%

**Table 2.1 Uptake of DK20 nanosponges by leukocytes in peripheral blood**

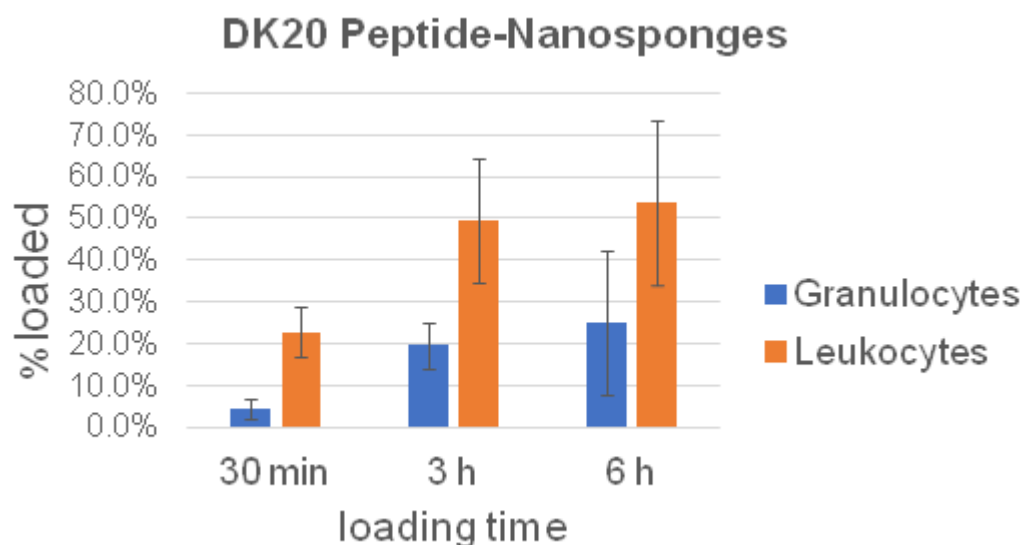


**Figure 2.8 Uptake efficacy of type DK20 nanosponges by leukocytes (mainly neutrophils and monocytes/macrophages) and granulocytes in peripheral blood as function of incubation time.**

White blood cells from cattle blood show a time dependent uptake of DK20 nanosponges. The entire WBC (white blood cells) population was subclassified into granulocytes and monocytes & macrophages. Here, the monocyte and macrophage group loaded twice as fast (>50%) compared to the granulocyte group (~25%). The loading was observed over a timeframe of 6 hours with the maximum loading completed after 3 hours.

Survival of the WBC population was analyzed by detecting apoptotic cells with the Annexin V fluorescent marker and dead cells with propidium iodine. The relative survival was measured after 5.5 and 7 hours of incubation with DK20 nanosponges and compared to a control group. The live cell population remained between 78% and 89% relative to the total cell count and with no significant difference between the control and the DK20 group for the duration of the experiment. Apoptotic cells were at approximately 12% after 5.5 hours, again with no significant difference between the two groups. The apoptotic cell count in the DK20 nanosponge group drops to 2% after seven hours while the dead cell count is significantly increased and measured at 15%. Our hypothesis is that this is observed due to the stress exerted on the WBS from endocytosis and processing of the DK20 nanosponges.

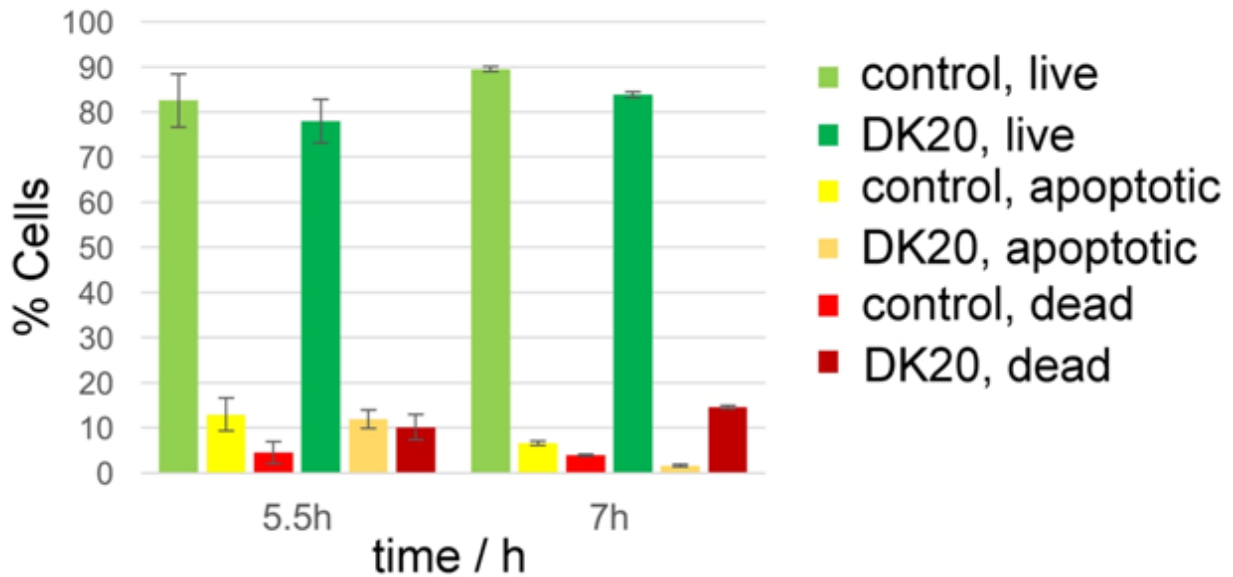


**Figure 2.9** Survival of WBC when exposed to DK20 peptide nanosponges, compared to the survival of an unexposed WBC control group. No significant difference ( $p>0.05$ ) between the treated and untreated live cell populations was detected after 5.5h. Due to the smaller experimental errors, there is a small, but significant difference in cell viabilities after 7h.

## 2.5 Discussion

Three main obstacles to efficient cell-mediated therapy of cancer and infectious diseases remain today: 1) Fast uptake of drug formulations by the transport cells. 2) Effective migration of the transport cells to their intended target. 3) Efficient drug release by the transport cells once the target is reached. The nanosponges that are discussed here will be able to efficiently target neural progenitor cells and leucocytes, either in cell cultures or, preferentially, in peripheral blood to utilize the advantages of autologous cells for patient-specific cell therapies. Because of their fast uptake kinetics and virtually non-existing toxicity, the nanosponges are well-suited for loading numerous drug formulations into various types of transport cells. Furthermore, because of their low toxicity to the transport cells, they make a very important contribution to facilitating effective cell migration to targets *in-vivo*, because the viability of the transport cells will remain high during the migration phase of several days. Finally, as we have demonstrated here by utilizing 5(6)-carboxyfluorescein as model drug, caspase-mediated drug release can be achieved. Although the observed release efficacy of carboxyfluorescein was only  $18\pm 1\%$ , the “caspase storm” during apoptosis has the potential of further degrading the nanosponges and to create numerous apoptotic bodies, to which the nanosponge-derived components will be adsorbed. Therefore, we anticipate a distinctly higher degree of release *in-vivo*.

We have utilized caspase-6 (MEROPS, ID:C14.005) in our studies, because it is one of the “effector caspases of apoptosis”.<sup>51</sup> Caspases 3 and 6 are responsible for significant morphological changes in the nucleus at the onset of apoptosis. For that purpose, they are internalized by the cell at the beginning of the path towards apoptosis. Caspase-6 cleaves nuclear lamina and the protein NuMa of the nuclear mitotic apparatus. Because caspase-6 is internalized, it is a suitable protease to cleave the DE-VDGC motif of the nanosponges. According to this

mechanism, drug release from the nanosponges within the transport cells can be triggered, which – in turn – leads to apoptosis of the transport cell and subsequent drug release.<sup>52</sup> It is noteworthy that the consensus sequence DEVGDC is also capable of reacting with caspases-2,3, and 7.

Neutrophils make up approx. 60 percent of leucocytes.<sup>53</sup> As already discussed, neutrophils undergo apoptosis within hours after reaching tumors and metastases.<sup>53</sup> Neural progenitor cells constitute a second class of delivery cells, which can migrate to solid tumors and metastases in large numbers.<sup>29, 34, 43</sup> However, the release of the payload has to be triggered by introducing apoptosis, as described above of by designing a TetOn gene regulation system, which silences a specific gene unless a tetracycline, such as doxycycline, is present.<sup>10, 54</sup>

## 2.6 Summary

The structure predictions for the supramolecular binary nanosponges (type DK20) through explicit solvent and then coarse-grained molecular dynamics (MD) simulations, have been confirmed by transmission electron microscopy and dynamic light scattering studies. The structural and dynamic understanding of the nanosponges has enabled several applications of these novel materials, which, principally, prove them as advanced biomaterials in cell-mediated drug transport to solid tumors/metastases and infectious diseases:

Caspase-activated (model) drug release could be demonstrated with 5(6)-carboxyfluorescein-loaded nanosponges).

PKH26-loaded nanosponges were essentially non-toxic to cultured neural progenitor cells (NPC).

Targeting of leucocytes (WBC) in peripheral blood was successful. After 3h of incubation, maximal uptake into leukocytes (mainly neutrophils and monocytes/macrophages) and granulocytes in peripheral blood was observed. No significant difference between the untreated and DK20-nanosponge-treated live cell populations was detected. This proves that direct targeting of leucocytes in peripheral blood, followed by re-injection of the treated blood is a promising path to effective cell-mediated therapy.

## 2.7 References

1. Yapa, A. S.; Bossmann, S. H., Development of Magnetic Theranostic Agents. In *Magnetic Nanomaterials: Applications in Catalysis and Life Sciences*, Bossmann, S. H.; Wang, H., Eds. RCS: London, 2017; Vol. in print.
2. Si, J.; Shao, S.; Shen, Y.; Wang, K., Macrophages as Active Nanocarriers for Targeted Early and Adjuvant Cancer Chemotherapy. *Small* **2016**, *12* (37), 5108-5119.
3. Danhier, F., To exploit the tumor microenvironment: Since the EPR effect fails in the clinic, what is the future of nanomedicine? *J. Controlled Release* **2016**, *244* (Part\_A), 108-121.
4. Tavano, L.; Muzzalupo, R., Multi-functional vesicles for cancer therapy: The ultimate magic bullet. *Colloids Surf., B* **2016**, *147*, 161-171.
5. Fathi, S.; Oyelere, A. K., Liposomal drug delivery systems for targeted cancer therapy: is active targeting the best choice? *Future Med. Chem.* **2016**, *8* (17), 2091-2112.
6. Srivastava, A.; Babu, A.; Filant, J.; Moxley, K. M.; Ruskin, R.; Dhanasekaran, D.; Sood, A. K.; McMeeki, S.; Ramesh, R., Exploitation of exosomes as nanocarriers for gene-, chemo-, and immune-therapy of cancer. *J. Biomed. Nanotechnol.* **2016**, *12* (6), 1159-1173.
7. Swain, S.; Sahu, P. K.; Beg, S.; Babu, S. M., Nanoparticles for Cancer Targeting: Current and Future Directions. *Curr. Drug Delivery* **2016**, *13* (8), 1290-1302.
8. Neto, W. S.; Pena, L. I.; Ferreira, G. R.; Souza Junior, F. G.; Machado, F., Target Delivery from Modified Polymers to Cancer Treatment. *Curr. Org. Chem.* **2017**, *21* (1), 4-20.
9. Basel, M. T.; Shrestha, T. B.; Troyer, D. L.; Bossmann, S. H., Protease-Sensitive, Polymer-Caged Liposomes: A Method for Making Highly Targeted Liposomes Using Triggered Release. *ACS Nano* **2011**, *5* (3), 2162-2175.
10. Basel, M. T.; Balivada, S.; Shrestha, T. B.; Seo, G.-M.; Pyle, M. M.; Tamura, M.; Bossmann, S. H.; Troyer, D. L., A Cell-Delivered and Cell-Activated SN38-Dextran Prodrug Increases Survival in a Murine Disseminated Pancreatic Cancer Model. *Small* **2012**, *8* (6), 913-920.
11. Nakamura, Y.; Mochida, A.; Choyke, P. L.; Kobayashi, H., Nanodrug Delivery: Is the Enhanced Permeability and Retention Effect Sufficient for Curing Cancer? *Bioconjugate Chem.* **2016**, *27* (10), 2225-2238.
12. Di Lorenzo, G.; De Placido, S.; Pagliuca, M.; Ferro, M.; Lucarelli, G.; Rossetti, S.; Bosso, D.; Puglia, L.; Pignataro, P.; Ascione, I.; De Cobelli, O.; Caraglia, M.; Aieta, M.;

- Terracciano, D.; Facchini, G.; Buonerba, C.; Sonpavde, G., The evolving role of monoclonal antibodies in the treatment of patients with advanced renal cell carcinoma: a systematic review. *Expert Opin. Biol. Ther.* **2016**, *16* (11), 1387-1401.
13. Parakh, S.; Parslow, A. C.; Gan, H. K.; Scott, A. M., Antibody-mediated delivery of therapeutics for cancer therapy. *Expert Opin. Drug Delivery* **2016**, *13* (3), 401-419.
  14. Hughes, P. E.; Caenepeel, S.; Wu, L. C., Targeted Therapy and Checkpoint Immunotherapy Combinations for the Treatment of Cancer. *Trends Immunol.* **2016**, *37* (7), 462-476.
  15. Bazak, R.; Houry, M.; El Achy, S.; Kamel, S.; Refaat, T., Cancer active targeting by nanoparticles: a comprehensive review of literature. *J. Cancer Res. Clin. Oncol.* **2015**, *141* (5), 769-784.
  16. Mukherjee, B.; Satapathy, B. S.; Mondal, L.; Dey, N. S.; Maji, R., Potentials and Challenges of Active Targeting at the Tumor Cells by Engineered Polymeric Nanoparticles. *Curr. Pharm. Biotechnol.* **2013**, *14* (15), 1250-1263.
  17. Sun, H.; Zu, Y., Aptamers and Their Applications in Nanomedicine. *Small* **2015**, *11* (20), 2352-2364.
  18. Wu, X.; Chen, J.; Wu, M.; Zhao, J. X., Aptamers: active targeting ligands for cancer diagnosis and therapy. *Theranostics* **2015**, *5* (4), 322-344, 23 pp.
  19. Hamidi, H.; Pietila, M.; Ivaska, J., The complexity of integrins in cancer and new scopes for therapeutic targeting. *Br. J. Cancer* **2016**, *115* (9), 1017-1023.
  20. Sun, C.-C.; Qu, X.-J.; Gao, Z.-H., Integrins: players in cancer progression and targets in cancer therapy. *Anti-Cancer Drugs* **2014**, *25* (10), 1107-1121.
  21. Jain, R. K.; Stylianopoulos, T., Delivering nanomedicine to solid tumors. *Nat. Rev. Clin. Oncol.* **2010**, *7* (11), 653-664.
  22. Shrestha, T. B.; Seo, G. M.; Basel, M. T.; Kalita, M.; Wang, H.; Villanueva, D.; Pyle, M.; Balivada, S.; Rachakatla, R. S.; Shinogle, H.; Thapa, P. S.; Moore, D.; Troyer, D. L.; Bossmann, S. H., Stem cell-based photodynamic therapy. *Photochem. Photobiol. Sci.* **2012**, *11* (7), 1251-1258.
  23. Seo, G.-M.; Rachakatla, R. S.; Balivada, S.; Pyle, M.; Shrestha, T. B.; Basel, M. T.; Myers, C.; Wang, H.; Tamura, M.; Bossmann, S. H.; Troyer, D. L., A self-contained enzyme activating prodrug cytotherapy for preclinical melanoma. *Mol. Biol. Rep.* **2012**, *39* (1), 157-165.
  24. Basel, M. T.; Balivada, S.; Wang, H.; Shrestha, T. B.; Seo, G. M.; Pyle, M.; Abayaweera, G.; Dani, R.; Koper, O. B.; Tamura, M.; Chikan, V.; Bossmann, S. H.; Troyer, D. L., Cell-delivered magnetic nanoparticles caused hyperthermia-mediated increased survival in a murine pancreatic cancer model. *Int. J. Nanomed.* **2012**, *7*, 297-306.

25. Troyer, D., Cell-based targeting of anti-cancer nanotherapy to tumors. *J. Cancer Sci. Ther.* **2013**, *5* (4), 142-143.
26. Alshetaiwi, H. S.; Balivada, S.; Shrestha, T. B.; Pyle, M.; Basel, M. T.; Bossmann, S. H.; Troyer, D. L., Luminol-based bioluminescence imaging of mouse mammary tumors. *J. Photochem. Photobiol., B* **2013**, *127*, 223-228.
27. Basel, M. T.; Shrestha, T. B.; Bossmann, S. H.; Troyer, D. L., Cells as delivery vehicles for cancer therapeutics. *Ther. Delivery* **2014**, *5* (5), 555-567.
28. Kulbe, H.; Levinson, N. R.; Balkwill, F.; Wilson, J. L., The chemokine network in cancer-much more than directing cell movement. *Int. J. Dev. Biol.* **2004**, *48* (5/6, Spec. Issue), 489-496.
29. Ullah, N.; Liaqat, S.; Fatima, S.; Zehra, F.; Anwer, M.; Sadiq, M., Stem cells and cancer: A review. *Asian Pac. J. Trop. Dis.* **2016**, *6* (5), 406-419.
30. Panni, R. Z.; Linehan, D. C.; DeNardo, D. G., Targeting tumor-infiltrating macrophages to combat cancer. *Immunotherapy* **2013**, *5* (10), 1075-1087.
31. Richards, D. M.; Hettinger, J.; Feuerer, M., Monocytes and Macrophages in Cancer: Development and Functions. *Cancer Microenviron.* **2013**, *6* (2), 179-191.
32. Coffelt, S. B.; Wellenstein, M. D.; de Visser, K. E., Neutrophils in cancer: neutral no more. *Nat. Rev. Cancer* **2016**, *16* (7), 431-446.
33. Mantovani, A., Macrophages, neutrophils, and cancer: a double edged sword. *New J. Sci.* **2014**, 1-15.
34. Rachakatla, R. S.; Balivada, S.; Seo, G.-M.; Myers, C. B.; Wang, H.; Samarakoon, T. N.; Dani, R.; Pyle, M.; Kroh, F. O.; Walker, B.; Leaym, X.; Koper, O. B.; Chikan, V.; Bossmann, S. H.; Tamura, M.; Troyer, D. L., Attenuation of Mouse Melanoma by A/C Magnetic Field after Delivery of Bi-Magnetic Nanoparticles by Neural Progenitor Cells. *ACS Nano* **2010**, *4* (12), 7093-7104.
35. Tecchio, C.; Cassatella, M. A., Neutrophil-derived chemokines on the road to immunity. *Semin. Immunol.* **2016**, *28* (2), 119-128.
36. Copier, J.; Bodman-Smith, M.; Dalglish, A., Current status and future applications of cellular therapies for cancer. *Immunotherapy* **2011**, *3* (4), 507-516.
37. Wang, H.; Yapa, A. S.; Kariyawasam, N.; Shrestha, T. B.; Wendel, S. O.; Yu, J.; Pyle, M.; Basel, M. T.; Malalasekera, A. P.; Toledo, Y.; Ortega, R.; Thapa, P. S.; Huang, H.; Sun, S. X.; Smith, P. E.; Troyer, D. L.; Bossmann, S. H., Rationally Designed Peptide Nanosponges for Cell-Based Cancer Therapy. *Nanomedicine NBM* **2017**, *submitted*.
38. Powell, D. R.; Huttenlocher, A., Neutrophils in the Tumor Microenvironment. *Trends Immunol.* **2016**, *37* (1), 41-52.

39. Logue, S. E.; Martin, S. J., Caspase activation cascades in apoptosis. *Biochem. Soc. Trans.* **2008**, *36* (1), 1-9.
40. <https://mai.ku.edu/about-mai-lab> (accessed 01/31/2017).
41. Welch, B. L., The Generalization of Students Problem When Several Different Population Variances Are Involved. *Biometrika* **1947**, *34* (1-2), 28-35.
42. Stockert, J. C.; Blazquez-Castro, A.; Canete, M.; Horobin, R. W.; Villanueva, A., MTT assay for cell viability: Intracellular localization of the formazan product is in lipid droplets. *Acta Histochem.* **2012**, *114* (8), 785-796.
43. Ourednik, J.; Ourednik, V.; Lynch, W. P.; Schachner, M.; Snyder, E. Y., Neural stem cells display an inherent mechanism for rescuing dysfunctional neurons. *Nat. Biotechnol.* **2002**, *20* (11), 1103-1110.
44. Rees, G.; Gough, R., Buffy-coat preparation from fresh whole blood. *J Med Lab Technol* **1968**, *25* (2), 117-8.
45. Cid, J.; Claparols, M.; Pinacho, A.; Hernandez, J. M.; Ortiz, P.; Puig, L. S.; Pla, R. P., Comparison of blood component preparation methods from whole blood bags based on buffy coat extraction. *Transfus Apher Sci* **2007**, *36* (3), 243-7.
46. Annexin V Apoptosis Kit [FITC]. [https://www.novusbio.com/products/annexin-v-kit\\_nbp1-92656](https://www.novusbio.com/products/annexin-v-kit_nbp1-92656) (accessed 04-17-2017).
47. Chen, R. F.; Knutson, J. R., Mechanism of fluorescence concentration quenching of carboxyfluorescein in liposomes: energy transfer to nonfluorescent dimers. *Anal. Biochem.* **1988**, *172* (1), 61-77.
48. Lee, J. E.; Lee, N.; Kim, T.; Kim, J.; Hyeon, T., Multifunctional Mesoporous Silica Nanocomposite Nanoparticles for Theranostic Applications. *Acc. Chem. Res.* **2011**, *44* (10), 893-902.
49. Shoji, A.; Sakamoto, M.; Sugawara, M. In *Design of liposomes with A pH-sensitive fluorescent dye and gramicidin channels for immune-sensing*, Nova Science Publishers, Inc.: 2014; pp 147-170.
50. Wang, H.; Shrestha, T. B.; Basel, M. T.; Dani, R. K.; Seo, G.-M.; Balivada, S.; Pyle, M. M.; Prock, H.; Koper, O. B.; Thapa, P. S.; Moore, D.; Li, P.; Chikan, V.; Troyer, D. L.; Bossmann, S. H., Magnetic-Fe/Fe<sub>3</sub>O<sub>4</sub>-nanoparticle-bound SN38 as carboxylesterase-cleavable prodrug for the delivery to tumors within monocytes/macrophages. *Beilstein J. Nanotechnol.* **2012**, *3*, 444-455, 12 pp.
51. Martinova, E. A., Apoptotic Regulation of Caspase Activity. *Russ. J. Bioorg. Chem.* **2003**, *29* (5), 471-495.

52. Gimenez-Bonafe, P.; Tortosa, A.; Perez-Tomas, R., Overcoming drug resistance by enhancing apoptosis of tumor cells. *Curr. Cancer Drug Targets* **2009**, *9* (3), 320-340.
53. Cowburn, A. S.; Condliffe, A. M.; Farahi, N.; Summers, C.; Chilvers, E. R., Advances in neutrophil biology: clinical implications. *Chest* **2008**, *134* (3), 606-612.
54. Le Guiner, C.; Stieger, K.; Toromanoff, A.; Rolling, F.; Moullier, P.; Adjali, O. In *Gene switches for pre-clinical studies in gene therapy*, World Scientific Publishing Co. Pte. Ltd.: 2010; pp 163-180.

# **Chapter 3 - Peptide Nanosponges Designed for the Cytotherapy of Gliomas**

## **3.1 Abstract**

Two different nanosponges featuring trigonal supramolecular building blocks, type (D-POH)<sub>10</sub>K<sub>20</sub> and (D-POH)<sub>10</sub>R<sub>20</sub> were synthesized, purified, and characterized by Dynamic Light Scattering (DLS) and Atomic Force Microscopy (AFM). They were then tested in cell cultures of murine glioma cells (GL26) and murine neural progenitor cells (NPC). The two nanosponges exhibited significantly different biophysical properties (size distribution and zeta potentials). Consequently, different efficacies in killing GL26 and NPC were observed in both, serum free and serum containing culture media. The results from these experiments confirmed that type (D-POH)<sub>10</sub>K<sub>20</sub> nanosponge is an excellent candidate for the cytototherapy of glioblastoma.

## 3.2 Background

To date, more than 130 types of brain<sup>1</sup> and central nervous system (CNS) tumors have been discovered. This study focus on one type of brain cancer; Glioblastoma multiforme (GBM or Glioblastoma). This formidable disease arises from star-shaped cells called astrocytes, which constitute of the supportive tissue of the brain. Since these cells can reproduce rapidly and they have ample blood supply, glioblastomas are usually highly malignant. Other than histology, the 2016 CNS WHO accounts molecular parameters for the central nervous system (CNS) tumor classification.<sup>2</sup> According to the latest WHO tumor classification, glioblastoma is a grade IV astrocytoma<sup>2</sup> and it is the most common and most aggressive/fatal primary glioma found in humans.<sup>3-5</sup>

In general, glioblastomas are found in both cerebral hemispheres of the brain, as well as the spinal cord. In contrast, the chances of diagnosing this tumor in other parts of the body are rare.<sup>4</sup>

Glioblastomas are divided into two sub categories; primary (new or de novo) and secondary tumors.<sup>4, 6</sup> De novo is the most common and aggressive form of GBM. It emerges quickly and tends to make its presence known abruptly. In contrast, secondary glioblastomas grow gradually, but still are very aggressive. They may start as low-grade or mid-grade tumors and eventually transform into higher grade tumors.<sup>4</sup>

Glioblastomas can be difficult to treat because of their histopathologically heterogeneous nature<sup>6</sup> and finger-like tentacles.<sup>7</sup> Moreover, many chemotherapeutics are unable to cross the blood–brain barrier<sup>8</sup>, which is required to act on the tumor. This is why the treatment plans for glioblastoma often combine several approaches.<sup>9</sup> When the tumor cannot be removed by surgery, radiation and chemotherapy are important to delay and control the growth of the tumor.<sup>9</sup>

However, all of these methods are not very successful. Consequently, the mortality of glioblastoma is very high.

According to Fonseca et al., the molecular genetics of malignant gliomas provides new targets for antineoplastic agents. Altered activation of the Ras/MAPK and PI3K/Akt pathways in gliomas<sup>10-11</sup> are promising therapy targets.<sup>4, 12-13</sup> These signaling pathways play a critical role in regulating diverse cellular functions including cell survival, cell cycle progression and cellular growth<sup>14</sup> in healthy cells, as well as in cancer cells. Overexpression of the oncogenes EGFR and PDGFR<sup>3-5, 15</sup> and “mutations and deletions of tumor suppressor genes TP53 and PTEN”<sup>4</sup> are the roots of those overactive signaling pathways.<sup>4</sup>

A family of membrane-associated small GTPases, Ras proteins, plays a vital role in cellular signal transduction.<sup>16</sup> They transduce extracellular signals provided by growth factors and cytokines. Elevated levels of Ras proteins are observed in glioblastoma patients. In order to become functionally active, Ras proteins must be attached to the inner cell membrane.<sup>16</sup> This membrane anchoring is facilitated by a posttranslational modification on Ras proteins. A farnesyl group is covalently attached to the cysteine on C-terminal of the CAAX motif of Ras protein. This process is catalyzed by the enzyme farnesyl transferase. Since unfarnesylated Ras is incapable of anchoring to the cell membrane, it is not capable of cellular transformation. Hence, farnesyl transferase inhibitors can be considered as a new class of antineoplastic drugs, which act by altering cell signal transduction and thereby inhibiting proliferation and survival of malignant cells.<sup>4</sup>

Recent studies have revealed that the naturally occurring monoterpene perillyl alcohol (IUPAC: [4-(prop-1-en-2-yl)cyclohex-1-en-1-yl]methanol) can be used as pharmacological inhibitor of the Ras-mediated signaling pathway.<sup>4, 17-19</sup> By conducting phase I clinical trials,

Azzoli et al. showed that the maximum tolerance dose of perillyl alcohol (POH) is 8400 mg/m<sup>2</sup> per day when delivered orally.<sup>20</sup> According to the phase I and phase II human clinical trial results, oral administration of POH does not exert hepatic, renal or neurobiological toxicity, but it does cause gastrointestinal track disturbances<sup>21</sup>, such as nausea, vomiting and diarrhea.<sup>20, 22-23</sup> It is necessary to find effective POH delivery strategies free of side effects. The novel Peptide-Nanosponges<sup>24-25</sup> that were developed earlier by us are ideal candidates for biomedical applications, because they are virtually non-toxic, highly biocompatible, and biodegradable.<sup>26</sup> They are safe packaging systems and capable of eliminating several problems that are persisting with lipid-based or viral delivery systems, such as antigenicity, and inflammatory effects, as well as insufficient stability and targeting specificity.<sup>27</sup>

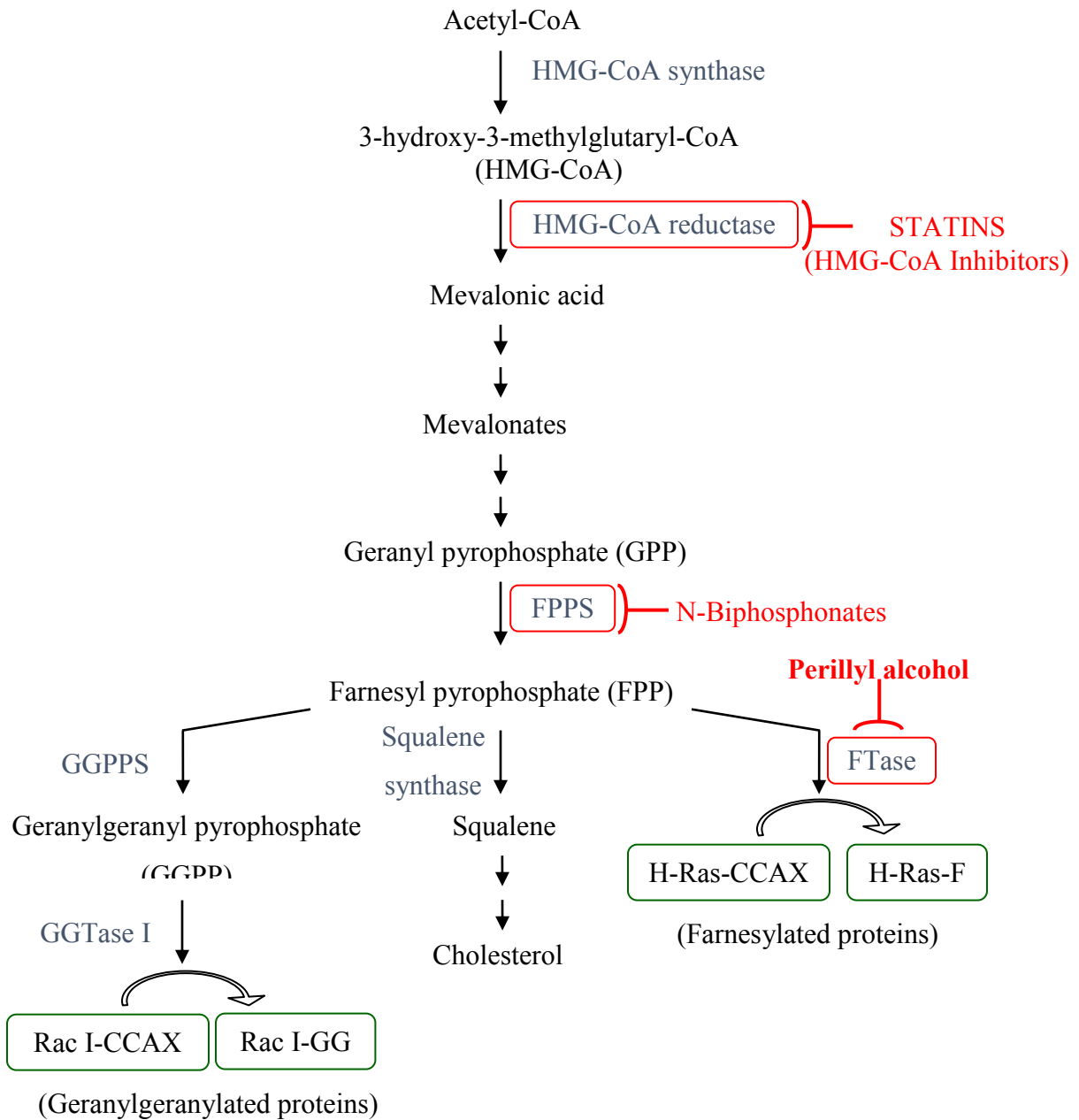


**Figure 3.1 Mevalonate/cholesterol pathway (Farnesyl diphosphate synthase (FPPS), Farnesyl transferase (FTase), Geranylgeranyl diphosphate synthase (GGPPS), Geranylgeranyl transferase (GGTase I))<sup>17, 28-32</sup>**

The novel nanosponges were designed by utilizing the self-assembling properties of (cholesterol-(K)<sub>n</sub>DEV DGC)<sub>3</sub>-trimaleimide and (cholesterol-(D)<sub>n</sub>DEV DGC)<sub>3</sub>-trimaleimide units that both feature a trigonal linker, a cleavable sequence designed for caspases-3, 6, and 7 (DEV DGC<sup>33</sup>) and either an oligo-lysine or oligo-aspartic acid sequence (n = 20). The C-terminus of each oligopeptide is attached to the trigonal linker via Michael addition to maleimide<sup>34</sup>, whereas the N-terminus is tethered to a hydrophobic cholesterol anchor. A sponge-like dynamic structure is spontaneously assembled, due to the formation of ion pairs, intense hydrogen bonding, and the occurrence of hydrophobic regions and water-filled nanocavities, as Coarse-Grained Molecular Dynamics simulations suggest. Molecular self-assembly is a free energy driven, spontaneous process, which offers many advantages when synthesizing tunable nanoscale structures, including adjustable size, shape and surface chemistries.<sup>26, 35-36</sup> In chapter 1, we studied the assembling properties of these adducts with same number of amino acids at physiological conditions. Upon mixing (cholesterol-(K)<sub>20</sub>DEV DGC)<sub>3</sub>-trimaleimide and (cholesterol-(D)<sub>20</sub>DEV DGC)<sub>3</sub>-trimaleimide units in aqueous media, nanosponges formed instantaneously.<sup>24</sup>

We demonstrated with different characterization methods such as, dynamic light scattering (DLS), transmission electron microscopy (TEM), and atomic force microscopy (AFM) that the obtained nanosponges are of low polydispersity and their sizes range from 100 to 150 nm in diameter. These nanosponges, which like regular sponges consist of neighboring regions of high lipophilicity and hydrophobicity, are essentially not toxic and are rapidly taken up by defensive cells in peripheral blood, such as neutrophils and monocytes.<sup>25</sup> Therefore, these nanosponges are well-suited materials for defensive cell-based drug-delivery applications in cancer therapy and theranostic applications.

### 3.2.1 Nanosponge-based Delivery Platforms for Perillyl Alcohol (POH)

We have developed two nanosponges for POH delivery by designing peptide chains containing segments of D<sub>10</sub>K<sub>20</sub>, and D<sub>10</sub>R<sub>20</sub>, thus combining oligoaspartic acid units with oligolysine or oligoarginine units. These peptides were again coupled to trimaleimide via the facile maleimide-thiol coupling reaction.<sup>34</sup> To the N-terminus of the peptides biotin was attached to enable targeted delivery by the nanosponge.<sup>37</sup> Then POH was covalently bound to the peptide via the carboxyl groups of the aspartic acid side chain. This ester bond is strong enough to survive the transport to gliomas through the blood brain barrier in neural progenitor cells<sup>38</sup>, but is easily hydrolyzed in the presence of proteases when the tumor site is reached and the payload is released. The novel drug-loaded carriers are biotin-(D-perillyl alcohol)<sub>10</sub>K<sub>20</sub>DEV DGC)<sub>3</sub>-trimaleimide (type (D-POH)<sub>10</sub>K<sub>20</sub>) and biotin-(D-perillyl alcohol)<sub>10</sub>R<sub>20</sub>DEV DGC)<sub>3</sub>-trimaleimide (type (D-POH)<sub>10</sub>R<sub>20</sub>).

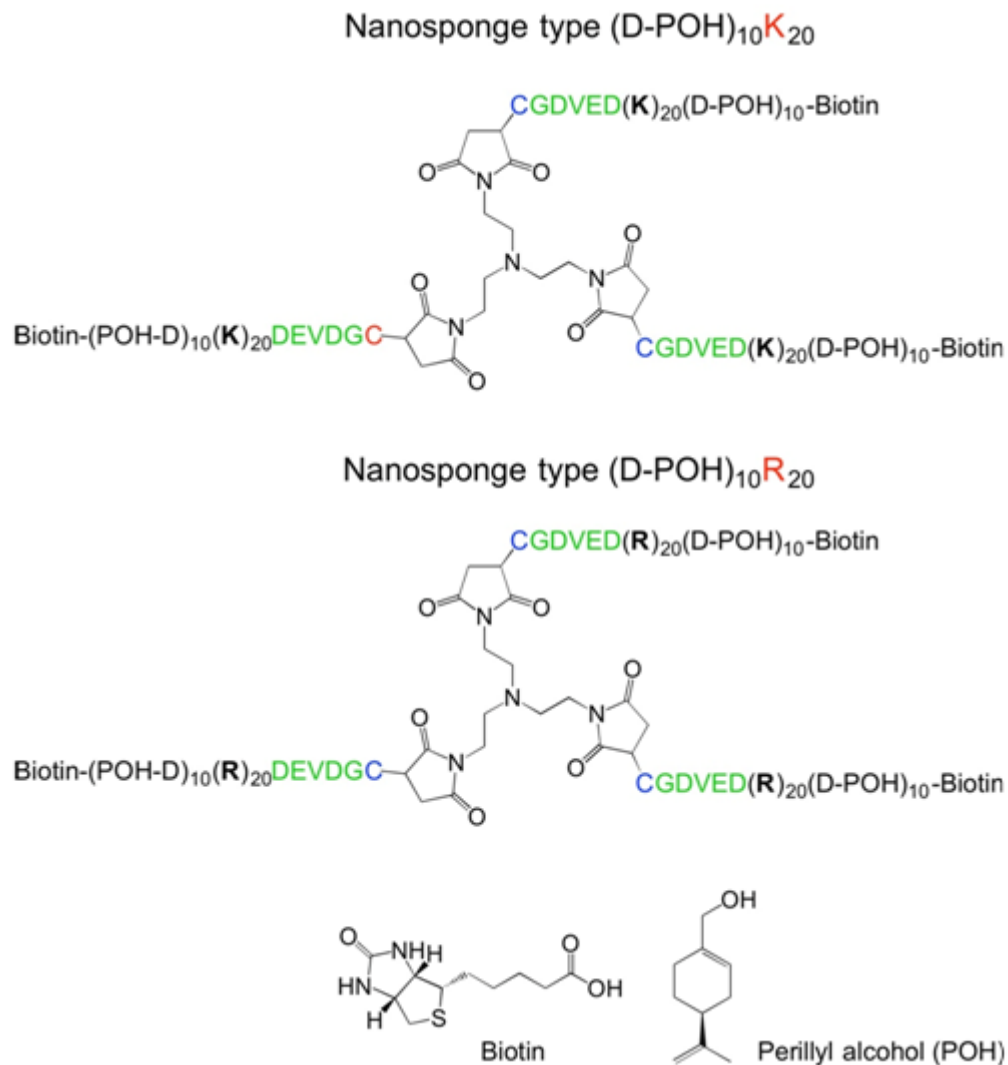


**Figure 3.2 Chemical structures of nanosponge types D(POH)<sub>10</sub>K<sub>20</sub> and D(POH)<sub>10</sub>R<sub>20</sub>: C: cysteine, G: glycine, D: aspartic acid, V: valine, E: glutamic acid, K: lysine, R: arginine. The chemical composition of the peptide components has been verified by MALDI-TOF. The data are included in the Appendix C.**

In this chapter, the “critical micellar concentrations”<sup>39</sup>, e.g. the concentration at which nanosponge- formation spontaneously occurs, has been determined for the nanosponge types D(POH)<sub>10</sub>K<sub>20</sub> and D(POH)<sub>10</sub>R<sub>20</sub>, as well as for their precursors featuring no attached perillyl alcohol units. The resulting structures have been investigated by Atomic Force Microscopy (tapping mode) as well.

Nanosponges for cytotherapy of gliomas using neural progenitor cells as drug carriers are only viable if it can be proven that a) the nanosponges are toxic to glioma cell cultures and b) that they are virtually not toxic to neural progenitor cells. Therefore, we have determined cell viabilities in serum-free and serum containing media.

## 3.3 Methods

### 3.3.1 Materials

Amino acids, F<sub>moc</sub>-Cys(Trt)-Rink Amide MBHA resin and *N,N,N',N'*-Tetramethyl-*O*-(1*H*-benzotriazol-1-yl)uronium hexafluorophosphate (HBTU) were purchased from peptides international Inc, Louisville, KY, USA. *N*-(3-Dimethylaminopropyl)-*N'*-ethylcarbodiimide hydrochloride (EDCxHCl) was procured from Oakwood Chemical, West Columbia SC, USA. 4-Dimethylaminopyridine (DMAP) was purchased from ACROS Organics, New Jersey, USA. Perillyl alcohol, Piperidine and Triisopropylsilane (TIPS) were purchased from Sigma Aldrich. *N,N*-Diisopropylethylamine (DIPA), trifluoroacetic acid, ether, methylene chloride and dimethylformamide (DMF) were purchased from Fisher Scientific.

### 3.3.2 Peptide Synthesis and Biotin Coupling

The D<sub>10</sub>K<sub>20</sub>DEVGDC and D<sub>10</sub>R<sub>20</sub>DEVGDC peptides were synthesized by iterative solid phase peptide synthesis according to standard Fmoc (*N*-(9-fluorenyl)methoxycarbonyl) protocol.<sup>40</sup> Fmoc-Cys(Trt)-Rink Amide MBHA resin was used as solid support. Biotin was coupled to the *N*- terminal aspartic acid (D) applying peptide coupling conditions. The synthesized peptide was purified by dialysis (MWCO 3500) and then lyophilized. It was qualitatively analyzed by HPLC (Shimadzu NexeraSR) utilizing a reverse phase (C18) column and H<sub>2</sub>O / CH<sub>3</sub>CN + 1% CF<sub>3</sub>COOH as eluent. The organic phase was increased from 0.5% to 40% within 30min. The corresponding HPLC chromatograms can be found in the Appendix C.

### **3.3.3 Synthesis of Type D<sub>10</sub>K<sub>20</sub> and D<sub>10</sub>R<sub>20</sub> Nanosponges via Michael Addition of D<sub>10</sub>K<sub>20</sub>DEVDGC or D<sub>10</sub>R<sub>20</sub>DEVDGC to Trimaleimide**

The biotinylated peptide (D<sub>10</sub>K<sub>20</sub>DEVDGC or D<sub>10</sub>R<sub>20</sub>DEVDGC) was dissolved in degassed, 1X PBS solution, pH 7.4. Trimaleimide<sup>24</sup> in degassed DMF was added drop-wise to the peptide solution (peptide: trimaleimide molar ratio; 4:1) while stirring at RT under inert atmosphere. The reaction was carried out for 24 h followed by dialysis (MWCO 3500). Solutions were freeze-dried. Yield: 85% of (Biotin-D<sub>10</sub>K<sub>20</sub>DEVDGC)<sub>3</sub>-trimaleimide and 87% of (Biotin-D<sub>10</sub>R<sub>20</sub>DEVDGC)<sub>3</sub>-trimaleimide. Resultant nanosponges were analyzed using FTIR (see Appendix C.4, C.6).

### **3.3.4 Perillyl Alcohol Loading to (Biotin-D<sub>10</sub>K<sub>20</sub>DEVDGC)<sub>3</sub>-trimaleimide**

(Biotin-D<sub>10</sub>K<sub>20</sub>DEVDGC)<sub>3</sub>-trimaleimide was dissolved in 1X PBS solution, pH 7.4. Perillyl alcohol in DMF was added drop-wise while stirring rapidly to obtain a uniform solution. Then a mixture of EDC (1-Ethyl-3-(3-dimethylaminopropyl)carbodiimide) and DMAP (4-Dimethylaminopyridine) in 1X PBS solution, pH 7.4, was added and stirred for 24 h (peptide: alcohol: EDC: DMAP molar ratios; 1:50:1.2:1). The product was purified by solvent extraction using dichloromethane. The aqueous phase was freeze dried to obtain final product. Yield: 55% of (Biotin-D<sub>10</sub>(Perillyl alcohol<sub>10</sub>)K<sub>20</sub>DEVDGC)<sub>3</sub>-trimaleimide. Drug loaded D10K20 nanosponge was analyzed using FTIR and HPLC (see Appendix C.5, C.8).

### **3.3.5 Perillyl Alcohol Loading to (Biotin-D<sub>10</sub>R<sub>20</sub>DEVDGC)<sub>3</sub>-trimaleimide**

The synthetic procedure for (Biotin-D<sub>10</sub>(Perillyl alcohol<sub>10</sub>)R<sub>20</sub>DEVDGC)<sub>3</sub>-trimaleimide was identical than for (Biotin-D<sub>10</sub>(Perillyl alcohol<sub>10</sub>)K<sub>20</sub>DEVDGC)<sub>3</sub>-trimaleimide, with the exception

of using 1X PBS with an adjusted pH = 5.5 (instead of pH = 7.4) for EDC coupling. Yield: 48% of (Biotin-D<sub>10</sub>(Perillyl alcohol<sub>10</sub>)R<sub>20</sub>DEVDC)<sub>3</sub>-trimaleimide. Perillyl alcohol loaded D10R20 nanosponge was analyzed using FTIR (see Appendix C.7).

### 3.3.6 Nanosponge Formation and DLS Characterization

Separate solutions of (Biotin-D<sub>10</sub>(Perillyl alcohol<sub>10</sub>)K<sub>20</sub>DEVDC)<sub>3</sub>-trimaleimide and (Biotin-D<sub>10</sub>(Perillyl alcohol<sub>10</sub>)R<sub>20</sub>DEVDC)<sub>3</sub>-trimaleimide in deoxygenated PBS buffer were prepared and filtered through 200 μm filters. The prepared stock solutions were 0.55 mM and 2.00 mM respectively. All other stock solutions were prepared by diluting the original solutions with deoxygenated PBS buffer. The hydrodynamic diameters and polydispersity indexes (PDI) of the formed nanosponges were measured by dynamic light scattering (DLS, ZetaPALS, Brookhaven Instruments Corp., Holtsville, NY).<sup>41</sup> All measurements were carried out at 298 K, using 658 nm laser wavelength, and 90 degree detection angle. Data were collected from an average of three measurements over 60 seconds. DLS was also used to estimate the critical micellar concentration (CMC)<sup>39</sup> of the nanosponges (see Appendix C for procedure).

### 3.3.7 AFM Characterization

Samples for atomic force microscopy (AFM) were prepared by adding one drop the nanosponge stock solution (0.050 M of each nanosponge in PBS) onto a freshly peeled MICA sheet, and followed by removing of the solvent by using a gentle nitrogen stream (2 min). AFM images were taken by a Nanoscope AFM image system (Digital Instruments) utilizing TESPA-HAR probes in tapping mode. The spring constant of the tip was 50 N/m and the frequency was 350 kHz. The set point, P gain and I gain were set at 1.2, 0.6 and 0.5, respectively. The images

were gathered with 256x256 pixel resolution at a scan rate of 1 Hz. The images were then analyzed by the Nanoscope software (Bruker) and by Adobe Photoshop (contour plots).

### 3.3.8 Cell Experiments and MTT Assays

The cytotoxicity of (Biotin-D<sub>10</sub>(Perillyl alcohol<sub>10</sub>)K<sub>20</sub>DEV DGC)<sub>3</sub>-trimaleimide and (Biotin-D<sub>10</sub>(Perillyl alcohol<sub>10</sub>)R<sub>20</sub>DEV DGC)<sub>3</sub>-trimaleimide nanosponges was assessed by utilizing the MTT assay<sup>42</sup> on C17.2 neural progenitor cells (NPCs)<sup>43</sup>, which were a gift from Dr. V. Ourednik (Iowa State University) to Dr. D. L. Troyer, DVM (Kansas State University, Anatomy & Physiology). NPCs were originally developed by Dr. Evan Snyder.<sup>44</sup> These cells were maintained in DMEM supplemented with 10% FBS (Sigma-Aldrich), 5% horse serum (Invitrogen), 1% glutamine (Invitrogen), and 1% penicillin/streptomycin (Invitrogen). GL26 murine glioma cells<sup>45</sup> were cultured in RPMI 1640 medium with 10% FBS, and 5% CO<sub>2</sub>. The percentage of viable cells was determined after 24 and 48 hours of incubation. Cells were seeded in T-25 flask. After 24 h of incubation at 37 °C and 5% CO<sub>2</sub>, cells were re-plated in a 96 well plate at 20000/cm<sup>2</sup> density and further incubated for 24 h at 37<sup>0</sup>C, 5% CO<sub>2</sub>, to obtain 80 % confluency before the type (D-POH)<sub>10</sub>K<sub>20</sub> or (D-POH)<sub>10</sub>R<sub>20</sub> nanosponges were added.

Concentration series of type (D-POH)<sub>10</sub>K<sub>20</sub> or (D-POH)<sub>10</sub>R<sub>20</sub> nanosponges (0.0, 0.1, 0.2, 0.5, 1.0, 2.0, 5.0, 10, 20, 40, 60, 80, 100 μmoles L<sup>-1</sup>) were prepared by dissolving the nanosponge components in the same media that were used for culturing the cells. Cells were incubated for 24/48 h at 37 °C. Eight replicates were prepared for each concentration. A portion of 10 μL of MTT reagent (5 mg/ml in PBS) was added to each of the 96 wells, and the plates were incubated for another 4 h at 37 °C. Finally, 100 μL of 10% sodium dodecyl sulfate in 0.010M HCl was added into each well and incubated for 24 h at 37 °C. Their absorbance was recorded by using a

plate reader at 550nm and 690nm. PBS solution was used as control for all the experiments. P-values were calculated according to the literature.<sup>46</sup>

## 3.4 Results

### 3.4.1 DLS Characterization of the Nanosponges

The effective diameters and the polydispersity index (PDI) values of the nanosponges obtained by dynamic light scattering measurements (DLS) are summarized in Table 3.1. DLS measurements were performed in the following manner: stock solutions of each of the two nanosponges were prepared at 0.55 mM (D-POH)<sub>10</sub>K<sub>20</sub>) and 2.00 mM (D-POH)<sub>10</sub>R<sub>20</sub>). 1.0  $\mu$ L aliquots of the stock solution of (Biotin-D<sub>10</sub>(Perillyl alcohol<sub>10</sub>)K<sub>20</sub>DEV DGC)<sub>3</sub>-trimaleimide were given stepwise to 1.0 mL of PBS. DLS was measured after 10 min at incubation of 37 °C after addition of each 1.0  $\mu$ L aliquot. For (Biotin-D<sub>10</sub>(Perillyl alcohol<sub>10</sub>)R<sub>20</sub>DEV DGC)<sub>3</sub>-trimaleimide, aliquots of 5.0  $\mu$ L were added. DLS was measured after 10 min at incubation of 37 °C after addition of each 5.0  $\mu$ L aliquot. Continuous monitoring by DLS for 12 hours at 298 K revealed that type (D-POH)<sub>10</sub>K<sub>20</sub> and (D-POH)<sub>10</sub>R<sub>20</sub> nanosponges are very stable in aqueous solution (PBS). The corresponding correlation curves and number-averaged size distributions are shown in Figure 3.3. Additional data are provided in the Appendix C.

As summarized in Table 3.1, the CMC of the (Biotin-D<sub>10</sub>(Perillyl alcohol<sub>10</sub>)K<sub>20</sub>DEV DGC)<sub>3</sub>-trimaleimide is about 0.0011 mM. At that concentration, nanosponges of the order of 2 micrometers in diameters are formed with relatively low polydispersity. In distinct contrast, supramolecular aggregation of (Biotin-D<sub>10</sub>(Perillyl alcohol<sub>10</sub>)R<sub>20</sub>DEV DGC)<sub>3</sub>-trimaleimide occurs not until the concentration of the supramolecular building blocks about 45 times greater. Interestingly, the resulting type (D-POH)<sub>10</sub>R<sub>20</sub> nanosponges are smaller in diameter (approx. 360 nm) at the CMC, but their polydispersity is significantly larger.

<b>Nanosponge Type</b>	<b>Diameter / nm</b>	<b>Concentration / mM</b>	<b>CMC / mM</b>	<b>Polydispersity</b>	<b>Zeta-Potential / mV</b>
<b>(D-POH)<sub>10</sub>K<sub>20</sub></b>	<b>1955 ± 258</b>	<b>0.0011</b>	<b>0.0011</b>	<b>0.134</b>	
<b>(D-POH)<sub>10</sub>K<sub>20</sub></b>	<b>1880 ± 205</b>	<b>0.00165</b>		<b>0.282</b>	<b>20 ± 1</b>
<b>(D-POH)<sub>10</sub>R<sub>20</sub></b>	<b>360 ± 52</b>	<b>0.0488</b>	<b>0.0488</b>	<b>0.307</b>	
<b>(D-POH)<sub>10</sub>R<sub>20</sub></b>	<b>421 ± 32</b>	<b>0.0676</b>		<b>0.113</b>	<b>- 2 ± 3</b>

**Table 3.1 Diameter and CMC of type (D-POH)<sub>10</sub>K<sub>20</sub> and (D-POH)<sub>10</sub>R<sub>20</sub> nanosponges**

It is of mechanistic interest that the CMC of type (D-POH)<sub>10</sub>K<sub>20</sub> is approx. 5 times lower than the CMC of the binary nanosponge (cholesterol-(D)<sub>20</sub>DEV DGC)<sub>3</sub>-trimaleimide and (cholesterol-(K)<sub>20</sub>DEV DGC)<sub>3</sub>-trimaleimide, (type DK20)) of 0.0050 mM (total concentration, 0.0025 mM (D) and 0.0025 mM (K)). In type DK20 each peptide sequence is attached to a terminal hydrophobic cholesterol unit ( $\log P^{47} = 7.39$ ) and charge-attraction, as well as hydrogen-bonding can occur in aqueous buffers.<sup>48</sup> In contrast, perillyl alcohol has a  $\log P = 1.95$ , which is not hydrophobic. The differences between type (D-POH)<sub>10</sub>K<sub>20</sub> and type K<sub>20</sub> are even more pronounced. For (cholesterol-(K)<sub>20</sub>DEV DGC)<sub>3</sub>-trimaleimide a CMC of 0.080 mM was determined by means of DLS, which is 70 times larger than the CMC of (Biotin-D<sub>10</sub>(Perillyl alcohol)<sub>10</sub>)R<sub>20</sub>DEV DGC)<sub>3</sub>-trimaleimide. The zeta potentials of type (D-POH)<sub>10</sub>K<sub>20</sub> nanosponges in PBS were positive, as this was expected considering that they contain either K<sub>20</sub> segments. In sharp contrast, the nanosponges featuring R<sub>20</sub> segments possess zeta potentials that are very close to 0 mV. This was quite surprising and a clear indication that the structures of type (D-POH)<sub>10</sub>K<sub>20</sub> and (D-POH)<sub>10</sub>R<sub>20</sub> nanosponges are very different! Whereas in (D-POH)<sub>10</sub>K<sub>20</sub> we observe oligo-lysine chains at the surface, in (D-POH)<sub>10</sub>R<sub>20</sub> the surface is characterized by either

the presence of aspartate-perillyl units, and/or the nanosponge is efficiently attracting chloride and/or ((di)hydrogen)phosphate anions from PBS.

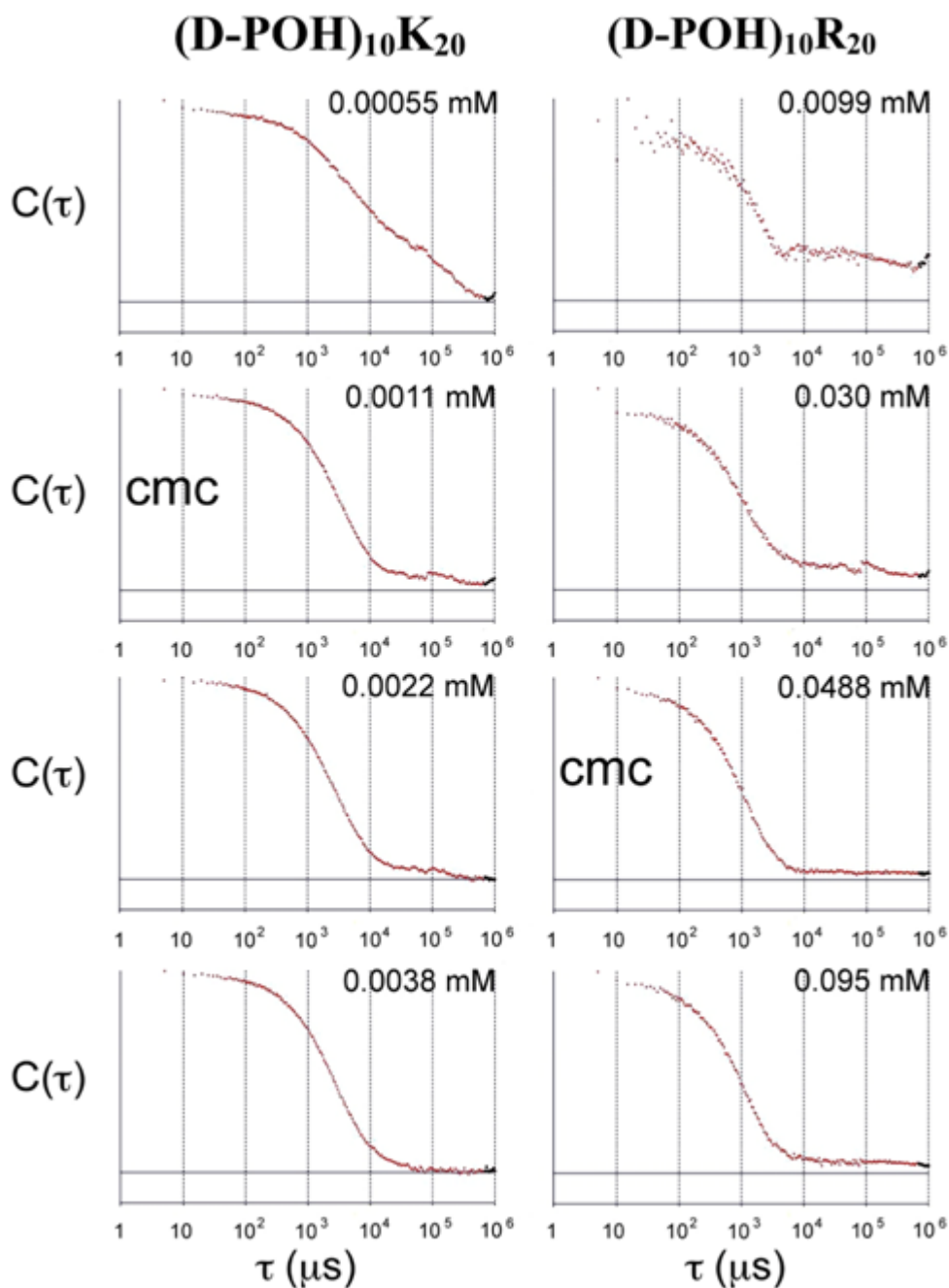


**Figure 3.3** Correlation curves ( $C(\tau)$ ) of dynamic light scattering measurements of (Biotin- $D_{10}$ (Perillyl alcohol $_{10}$ ) $K_{20}$ DEVDC) $_3$ -trimaleimide nanosponges (type (D-POH) $_{10}$  $K_{20}$ ) and (Biotin- $D_{10}$ (Perillyl alcohol $_{10}$ ) $R_{20}$ DEVDC) $_3$ -trimaleimide nanosponges (type (D-POH) $_{10}$  $R_{20}$ ) in deoxygenated PBS buffer below and above their CMC (“critical micellar concentration”<sup>39</sup>).

In Figure 3.4, the concentration dependence of type (D-POH)<sub>10</sub>K<sub>20</sub> and (D-POH)<sub>10</sub>R<sub>20</sub> nanosponges is shown. Both curves begin at their respective (estimated) cmc's. Apparently, the sizes of both types of nanosponges can be adjusted by selecting the correct concentration. Rapid changes of the observed nanosponge diameters have been measured during the first 10 min. After that time, the observed diameters did not change within the experimental errors for 24h.

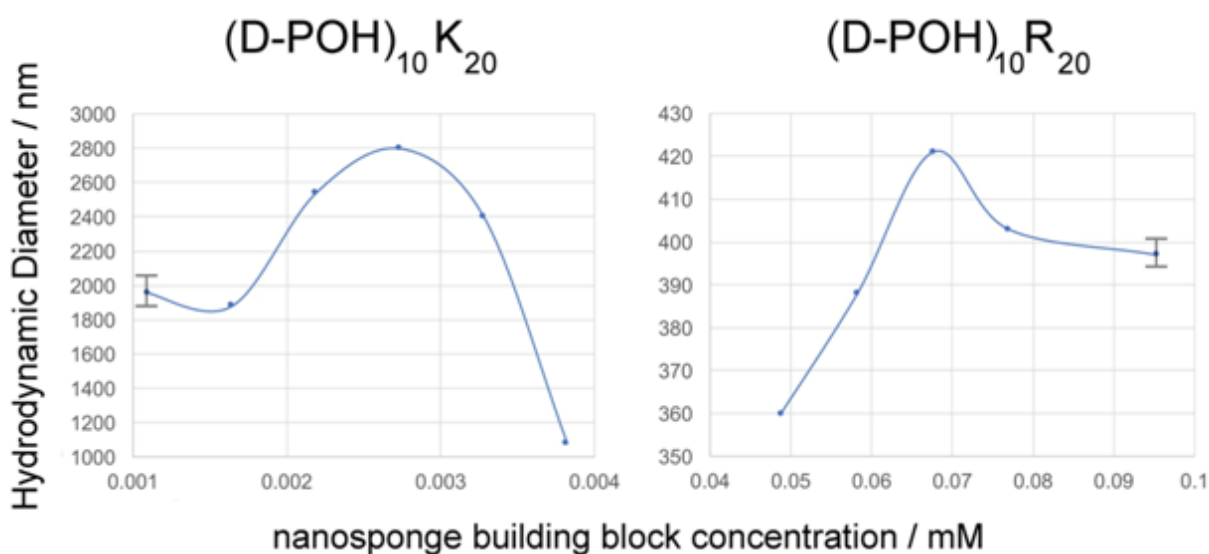


**Figure 3.4 Average hydrodynamic diameters, as measured by DLS, as a function of type (D-POH)<sub>10</sub>K<sub>20</sub> and type (D-POH)<sub>10</sub>R<sub>20</sub> nanosponge concentrations. In each curve, the typical experimental error is indicated.**

### 3.4.2 Atomic Force Microscopy of Type (D-POH)<sub>10</sub>K<sub>20</sub> and type (D-POH)<sub>10</sub>R<sub>20</sub>

#### Nanosponges

Figures 3.5 shows the AFM images type (D-POH)<sub>10</sub>K<sub>20</sub> and (D-POH)<sub>10</sub>R<sub>20</sub> nanosponges. Both types form irregular aggregates on MICA surfaces (sheet silica mineral). The resulting structures are approx. 110- 130 nm in height for both types. The heights of the bundles are between 150 to 250 nm. The widths for both types range from 220 to 420 nm. However, as the contour plots indicate, numerous smaller aggregates are present as well.

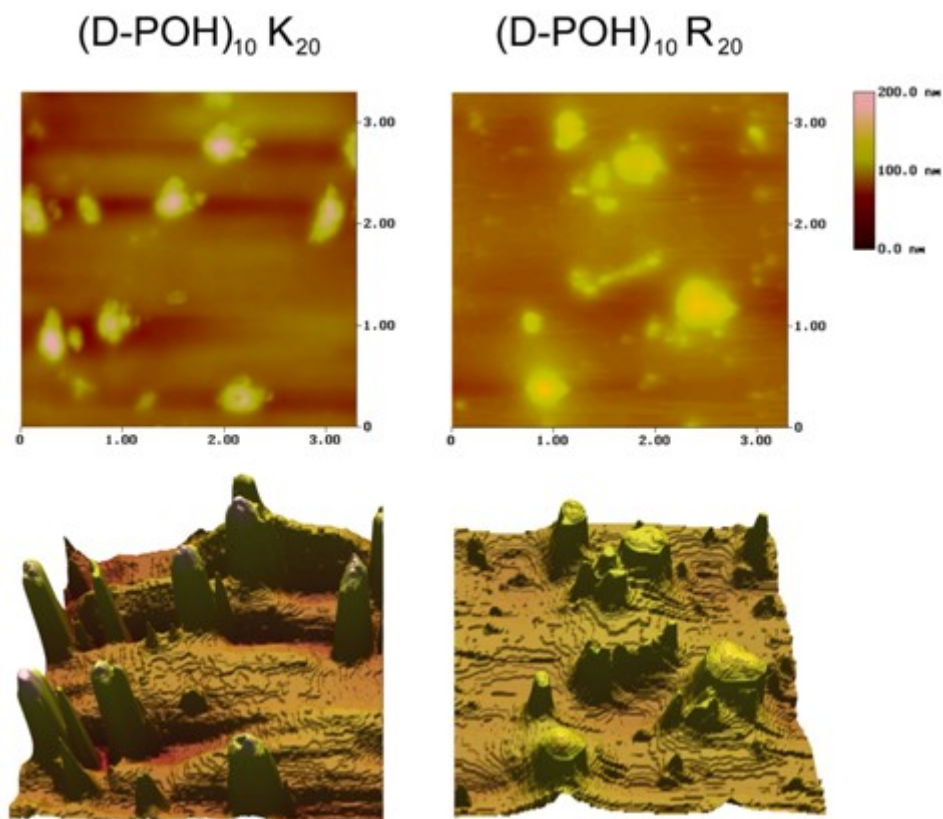


**Figure 3.5 AFM images (tapping mode) of (D-POH)<sub>10</sub>K<sub>20</sub> and (D-POH)<sub>10</sub>R<sub>20</sub> nanosponges (0.050 M of each nanosponge in PBS mM) on MICA.**

### 3.4.3 Cell Experiments and MTT Assays

The first set of cell experiments was carried out in serum free media. Cell viability was measured by using the MTT assay, which is sensitive to cell proliferation.<sup>42</sup> Before performing cell toxicity experiments with nanosponges containing perillyl alcohol, the toxicity of perillyl alcohol itself was tested. The results, which prove that perillyl alcohol is virtually not toxic to neural progenitor cells (NPC) and glioma cells (GL26), are shown in the Appendix C. The same concentrations of perillyl alcohol were used, either as free perillyl alcohol in the control experiments, or chemically bound to both nanosponges. Furthermore, we have tested the toxicity

of the nanosponges without attached perillyl alcohol. Both, type D<sub>10</sub>K<sub>20</sub> and type D<sub>10</sub>R<sub>20</sub> nanosponges were essentially not toxic to both, GL26 and NPC cells (Appendix C.13). After establishing this, we proceeded to testing nanosponges with chemically attached perillyl units.

The experiments reported here comprise measuring the cell viabilities of neural progenitor cells and murine glioma cells after adding type (D-POH)<sub>10</sub>K<sub>20</sub> and (D-POH)<sub>10</sub>R<sub>20</sub> nanosponges for 24h and 48h. The concentrations of both nanosponges that were added to the cell cultures ranged from 0 to 0.16  $\mu\text{g/mL}$ .

Both perillyl alcohol-containing nanosponges caused only very little toxicity when incubated with neural progenitor cells after 24h<sup>43</sup>, however, after 48h cell toxicity was significant. Both nanosponges were equally effective against murine glioma cells<sup>45</sup> after 24h and 48h of incubation (Figures 3.6 and 3.7). LC50 values for all experiments performed were calculated using the Graphpad Prism software<sup>49</sup> and are summarized in Table 3.2.

The experiments conducted in the presence of 10% FBS exhibited promising results for type (D-POH)<sub>10</sub>K<sub>20</sub> nanosponges. They remained to be very effective against GL26 cells after both, 24 and 48 hours of incubation (Figures 3.8 and 3.9). It is noteworthy that type (D-POH)<sub>10</sub>K<sub>20</sub> nanosponges show also a modest activity against neural progenitor cells, albeit only at the highest tested concentration. Fortunately, this finding does not rule NPCs out as transport cells for (D-POH)<sub>10</sub>K<sub>20</sub> in future animal models testing cell-mediated glioma therapy. Type (D-POH)<sub>10</sub>R<sub>20</sub> did not exhibit any activity, neither against GL26, nor against NPC cells in serum-containing medium. Potential reasons for the observed differences in the activities of (D-POH)<sub>10</sub>K<sub>20</sub> and (D-POH)<sub>10</sub>R<sub>20</sub> nanosponges will be considered in the Discussion section.

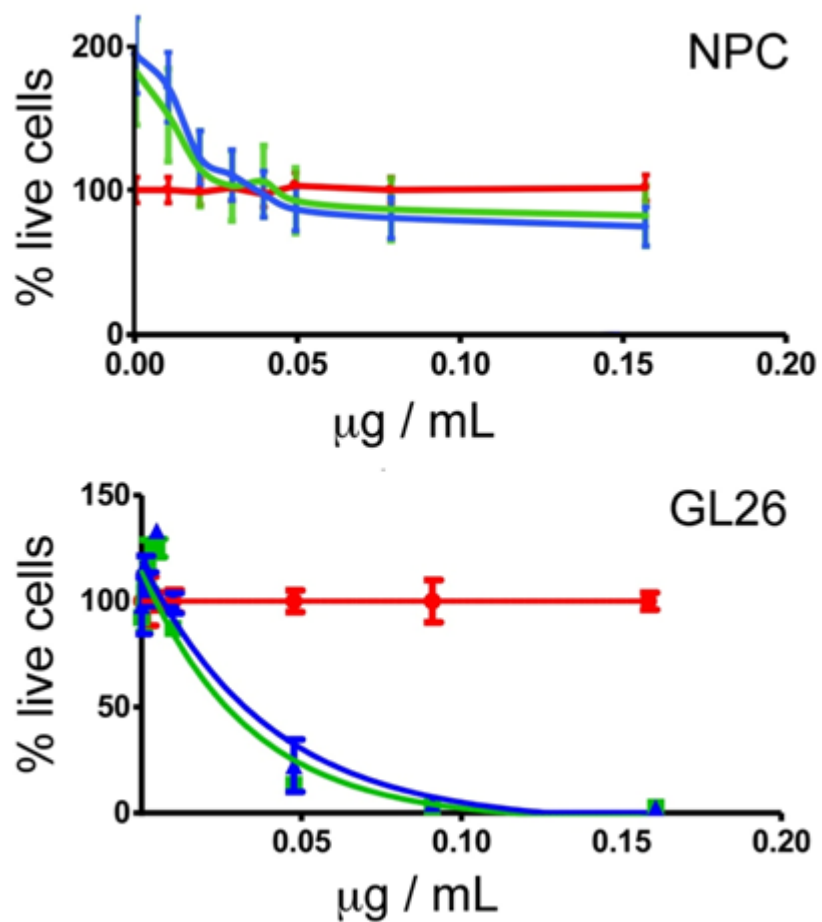
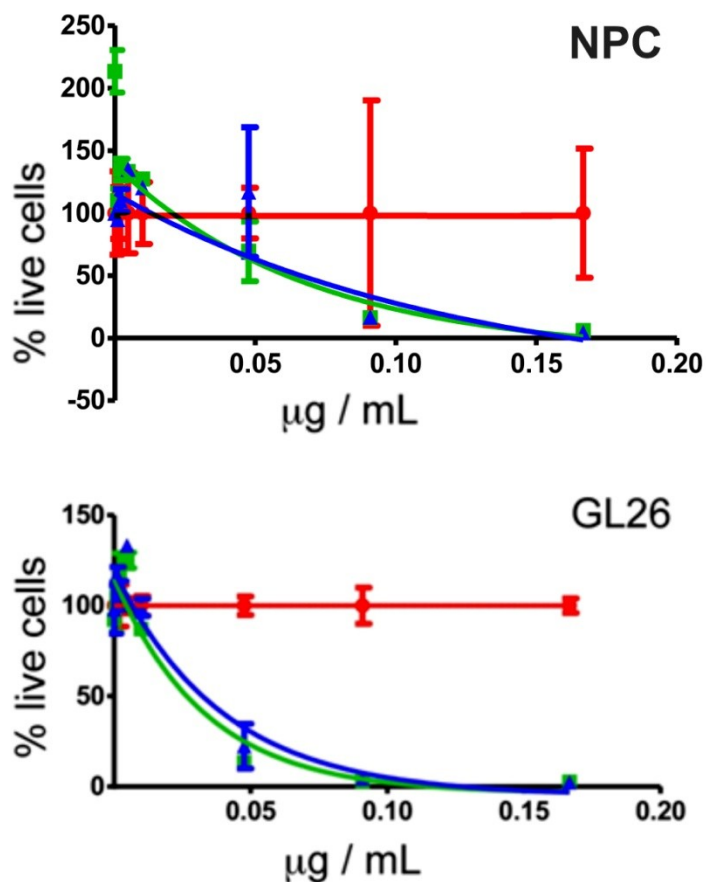


Figure 3.6 Cell viabilities of neural progenitor cells (NPC) and murine glioma cells (GL26) as a function of the concentration of type (D-POH)<sub>10</sub>K<sub>20</sub> (green) and (D-POH)<sub>10</sub>R<sub>20</sub> (blue) nanosponge in serum free medium after 24h of exposure. The red line is showing the results of the control experiment (only PBS was added).



**Figure 3.7** Cell viabilities of neural progenitor cells (NPC) and murine glioma cells (GL26) as a function of the concentration of type (D-POH)<sub>10</sub>K<sub>20</sub> (green) and (D-POH)<sub>10</sub>R<sub>20</sub> (blue) nanosponge in serum free medium after 48h of exposure. The red line is showing the results of the control experiment (only PBS was added).

One further control experiment has been added to the MTT experiments shown in Figure 3.8: 2 µl of 5 x 10<sup>-9</sup> moles L<sup>-1</sup> of active recombinant caspase-6 (purchased from Enzo Lifesciences) was added to each well before the cells were incubated for 24h in the presence of (D-POH)<sub>10</sub>R<sub>20</sub>. Caspase-6 will cleave the consensus sequence DEVDGC, which leads to a partial release of the payload, as previously demonstrated.<sup>25</sup> However, this measure was unable to enhance the cell toxicity of (D-POH)<sub>10</sub>R<sub>20</sub>.

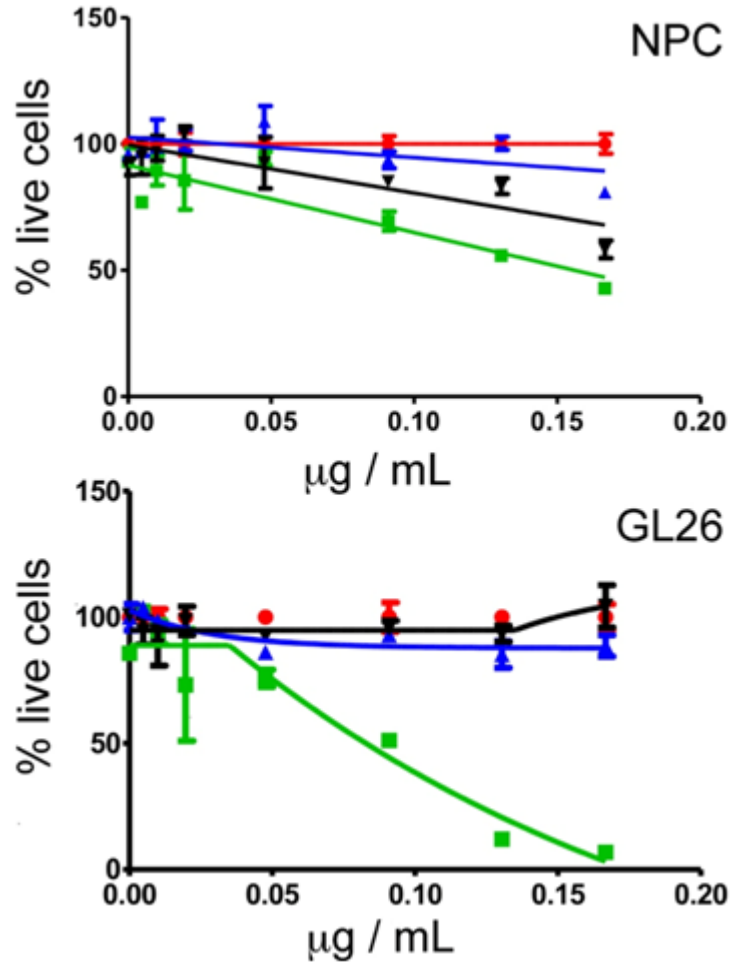


Figure 3.8 Cell viabilities of neural progenitor cells (NPC) and murine glioma cells (GL26) as a function of the concentration of type (D-POH)<sub>10</sub>K<sub>20</sub> (green) and (D-POH)<sub>10</sub>R<sub>20</sub> (blue) nanosponge in serum-containing medium (10% FBS, 5% horse serum) after 24h of exposure. The red line is showing the results of the control experiment (only PBS was added). The black line is a second control that was introduced by adding  $5 \times 10^{-9}$  M of active recombinant caspase-6 (Enzo Lifesciences) to (D-POH)<sub>10</sub>R<sub>20</sub>.

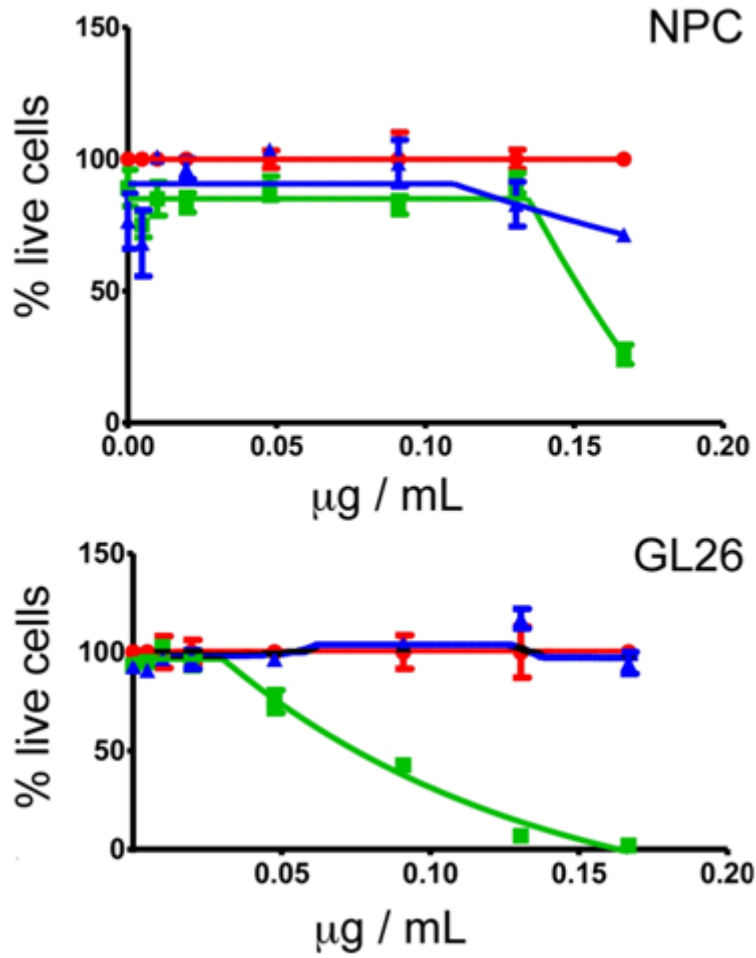


Figure 3.9 Cell viabilities of neural progenitor cells (NPC) and murine glioma cells (GL26) as a function of the concentration of type (D-POH)<sub>10</sub>K<sub>20</sub> (green) and (D-POH)<sub>10</sub>R<sub>20</sub> (blue) nanosponge in serum-containing medium (10% FBS, 5% horse serum) after 48h of exposure. The red line is showing the results of the control experiment (only PBS was added).

	<b>(D-POH)<sub>10</sub>K<sub>20</sub></b>			<b>(D-POH)<sub>10</sub>R<sub>20</sub></b>		
	<b>LC50 µg/ml</b>	<b>LC50 nmol/L</b>	<b>95% confidence interval µg/ml</b>	<b>LC50 µg/ml</b>	<b>LC50 nmol/L</b>	<b>95% confidence interval µg/ml</b>
	<b>24h, serum free medium</b>					
<b>GL26</b>	0.0233	1.29	0.01456 to 0.05832	1.40	0.0276	0.01674 to 0.07868
<b>NPC</b>	---	---		---	---	
	<b>48h, serum free medium</b>					
<b>GL26</b>	0.0303	1.68	0.01684 to 0.1559	1.53	0.0301	0.01918 to 0.07123
<b>NPC</b>	0.0478	2.65	0.02598 to 0.3156	---	---	
	<b>24h, serum containing medium</b>					
<b>GL26</b>	0.0801	4.44	0.02831 to 0.09468	---	---	
<b>NPC</b>	---	---		---	---	
	<b>48h, serum containing medium</b>					
<b>GL26</b>	0.0747	4.14	0.056632 to 0.05126	---	---	
<b>NPC</b>	0.152	32.10	0.12632 to 0.98804	---	---	

**Table 3.2 LC50 values of type (D-POH)<sub>10</sub>K<sub>20</sub> and (D-POH)<sub>10</sub>R<sub>20</sub> nanosponges (in µg/ml and nmol/l) for GL26 and NPC cell lines. Experiments were conducted in serum free and serum containing media.**

### 3.5 Discussion

Two types of nanosponges, (D-POH)<sub>10</sub>K<sub>20</sub> and (D-POH)<sub>10</sub>R<sub>20</sub> were developed as nanoshuttles to transport the anticancer agent, perillyl alcohol into glioma tumor cells, and for rapid uptake by neural progenitor cells, which can potentially serve as transport cells in future cytotherapies of glioblastoma. The peptide nanosponges contain a trigonal maleimide linker and three branches. Their major difference is the presence of either a K<sub>20</sub> or a R<sub>20</sub> block in (D-POH)<sub>10</sub>K<sub>20</sub> and (D-POH)<sub>10</sub>R<sub>20</sub>. Both contain the DEVDGC consensus sequence for caspase cleavage and a terminal D<sub>10</sub> unit to which 10 perillyl alcohol molecules are bound via ester functions. The latter can be easily hydrolyzed by numerous proteases and esterases, which are overexpressed in gliomas. Figure 3.10 shows the different regions of each branch in the trigonal building blocks for the nanosponges. Whereas D<sub>10</sub> is responsible for the reversible binding of perillyl alcohol, K<sub>20</sub> and R<sub>20</sub> are designed to enhance cellular uptake, either by endocytosis or transport through the membrane. The consensus sequence can be cleaved by all effector caspases (e.g. caspase -2, -3, -6, -7), which are overexpressed in virtually all solid tumors. Caspases -3 and -6 are taken up by cells and are, therefore, suitable to cleave the consensus sequences of nanosponges that have been taken up by transport cells, thus triggering their release by means of apoptotic processes, which enhance the porosity of the transport cells and then dissect them into apoptotic bodies.

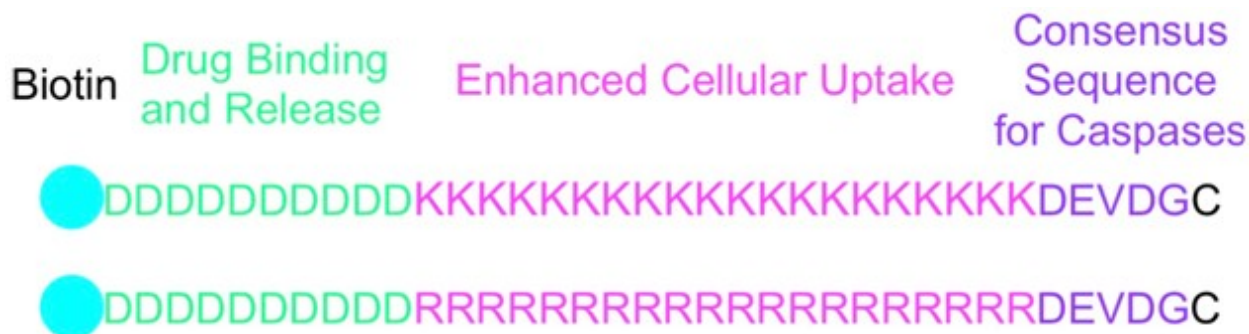


**Figure 3.10 Functions of the different regions of each peptide branch in (D-POH)<sub>10</sub>K<sub>20</sub> and (D-POH)<sub>10</sub>R<sub>20</sub>. Biotin is added to enhanced water-solubility and to facilitate enhanced uptake.**

From the control experiment shown in Figure 3.8 and summarized in Table 3.2, it is apparent that the presence of caspase-6 does not enable efficient cell killing by (D-POH)<sub>10</sub>R<sub>20</sub>, whereas (D-POH)<sub>10</sub>K<sub>20</sub> is able to kill GL26 glioma cells in low nanomolecular concentrations, even in the presence of serum. Since it is known that caspase-6 can be taken up by cells, it is our conclusion that the uptake, not the enzymatic activation of the perillyl-containing nanosponge is the critical step in killing the cells. This is in agreement with the control experiment (see Appendix C.13), in which perillyl alcohol in the absence of nanosponges, but in the same concentration than bound to the nanosponges, was added to both, GL26 and NPC cell cultures. In both cases, perillyl alcohol was virtually not toxic to the cells, because it is not taken up efficiently at that low concentrations. Since the overall metabolism of GL26 cells is higher than of NPC cells, the killing efficacy of (D-POH)<sub>10</sub>K<sub>20</sub> nanosponges is higher in the cancer cells at both, 24h and 48h. It is our conclusion that K<sub>20</sub> is far more efficient than R<sub>20</sub> in facilitating cellular uptake of the nanosponges. Furthermore, the presence of biotin at the N-terminal end of the peptide branches does not enable fast receptor-mediated uptake of the nanosponges, at least not in the presence of serum when biotin is not a limiting nutrient. The LC50 for (D-POH)<sub>10</sub>K<sub>20</sub> nanosponges in the

presence of serum for GL26 increased by 320% (24h) and 265% (48h), but remained in the nano-molar region.

### 3.6 Summary

Based on the experiments discussed here, one of the two trigonal nanosponges, type (D-POH)<sub>10</sub>K<sub>20</sub> is a promising candidate for delivering perillyl alcohol to glioblastomas. The second candidate, type (D-POH)<sub>10</sub>R<sub>20</sub>, fails to kill murine glioma cells (GL26) in the presence of serum. Both, type (D-POH)<sub>10</sub>K<sub>20</sub> and (D-POH)<sub>10</sub>R<sub>20</sub> are taken up by neuronal progenitor cells and show either no or low toxicity, as determined in cell viability experiments. We attribute the different biological effects that are caused by the two types of nanosponges to their different structures, which are indicated by significant differences in nanosponge sizes (according to DLS and, to a lesser degree, also AFM) and zeta potentials.

### 3.7 References

1. Nabors, L. B.; Portnow, J.; Ammirati, M.; Baehring, J.; Brem, H.; Brown, P.; Butowski, N.; Chamberlain, M. C.; Fenstermaker, R. A.; Friedman, A.; Gilbert, M. R.; Hattangadi-Gluth, J.; Holdhoff, M.; Junck, L.; Kaley, T.; Lawson, R.; Loeffler, J. S.; Lovely, M. P.; Moots, P. L.; Mrugala, M. M.; Newton, H. B.; Parney, I.; Raizer, J. J.; Recht, L.; Shonka, N.; Shrieve, D. C.; Sills, A. K., Jr.; Swinnen, L. J.; Tran, D.; Tran, N.; Vrionis, F. D.; Weiss, S.; Wen, P. Y.; McMillian, N.; Eng, A. M., Central nervous system cancers, version 1.2015. *J. Natl. Compr. Cancer Network* **2015**, *13* (10), 1191-1202.
2. Louis, D. N.; Perry, A.; Reifenberger, G.; von Deimling, A.; Figarella-Branger, D.; Cavenee, W. K.; Ohgaki, H.; Wiestler, O. D.; Kleihues, P.; Ellison, D. W., The 2016 World Health Organization Classification of Tumors of the Central Nervous System: a summary. *Acta Neuropathologica* **2016**, *131* (6), 803-820.
3. Bleeker, F. E.; Molenaar, R. J.; Leenstra, S., Recent advances in the molecular understanding of glioblastoma. *J Neuro-Oncol* **2012**, *108* (1), 11-27.
4. da Fonseca, C. O.; Landeiro, J. A.; Clark, S. S.; Quirico-Santos, T.; Carvalho, M. D. D.; Gattass, C. R., Recent advances in the molecular genetics of malignant gliomas disclose targets for antitumor agent perillyl alcohol. *Surg Neurol* **2006**, *65*, S2-S9.
5. Holland, E. C., Glioblastoma multiforme: The terminator. *Proc. Natl. Acad. Sci. U. S. A.* **2000**, *97* (12), 6242-6244.
6. Huse, J. T.; Holland, E.; DeAngelis, L. M., Glioblastoma: Molecular Analysis and Clinical Implications. *Annu Rev Med* **2013**, *64*, 59-70.
7. Glioblastoma and Malignant Astrocytoma. *Glioblastoma and Malignant Astrocytoma, American Brain Tumor Association.*
8. Lawson, H. C.; Sampath, P.; Bohan, E.; Park, M. C.; Hussain, N.; Olivi, A.; Weingart, J.; Kleinberg, L.; Brem, H., Interstitial chemotherapy for malignant gliomas: the Johns Hopkins experience. *J Neuro-Oncol* **2007**, *83* (1), 61-70.
9. Brain tumor information. *Brain tumor information, American Brain Tumor Association.*
10. Holland, E. C.; Celestino, J.; Dai, C. K.; Schaefer, L.; Sawaya, R. E.; Fuller, G. N., Combined activation of Ras and Akt in neural progenitors induces glioblastoma formation in mice. *Nat Genet* **2000**, *25* (1), 55-57.
11. Rajasekhar, V. K.; Viale, A.; Socci, N. D.; Wiedmann, M.; Hu, X. Y.; Holland, E. C., Oncogenic Ras and Akt signaling contribute to glioblastoma formation by differential recruitment of existing mRNAs to Polysomes. *Mol Cell* **2003**, *12* (4), 889-901.

12. Da Fonseca, C. O.; Teixeira, R. M.; Silva, J. C. T.; Fischer, J. D. D.; Meirelles, O. C.; Landeiro, J. A.; Quirico-Santos, T., Long-term Outcome in Patients with Recurrent Malignant Glioma Treated with Perillyl Alcohol Inhalation. *Anticancer Res* **2013**, *33* (12), 5625-5631.
13. da Fonseca, C. O.; Linden, R.; Futuro, D.; Gattass, C. R.; Quirico-Santos, T., Ras pathway activation in gliomas: a strategic target for intranasal administration of perillyl alcohol. *Arch Immunol Ther Exp (Warsz)* **2008**, *56* (4), 267-76.
14. Fresno Vara, J. A.; Casado, E.; de Castro, J.; Cejas, P.; Belda-Iniesta, C.; Gonzalez-Baron, M., PI3K/Akt signalling pathway and cancer. *Cancer Treat Rev* **2004**, *30* (2), 193-204.
15. Szerlip, N. J.; Pedraza, A.; Chakravarty, D.; Azim, M.; McGuire, J.; Fang, Y. Q.; Ozawa, T.; Holland, E. C.; Huse, J. T.; Jhanwar, S.; Leversha, M. A.; Mikkelsen, T.; Brennan, C. W., Intratumoral heterogeneity of receptor tyrosine kinases EGFR and PDGFRA amplification in glioblastoma defines subpopulations with distinct growth factor response. *Proc. Natl. Acad. Sci. U. S. A.* **2012**, *109* (8), 3041-3046.
16. Inder, K. L.; Lau, C.; Loo, D.; Chaudhary, N.; Goodall, A.; Martin, S.; Jones, A.; van der Hoeven, D.; Parton, R. G.; Hill, M. M.; Hancock, J. F., Nucleophosmin and nucleolin regulate K-Ras plasma membrane interactions and MAPK signal transduction. *J Biol Chem* **2009**, *284* (41), 28410-9.
17. Afshordel, S.; Kern, B.; Clasohm, J.; Konig, H.; Priester, M.; Weissenberger, J.; Kogel, D.; Eckert, G. P., Lovastatin and perillyl alcohol inhibit glioma cell invasion, migration, and proliferation - Impact of Ras-/Rho-prenylation. *Pharmacol Res* **2015**, *91*, 69-77.
18. Fernandes, J.; da Fonseca, C. O.; Teixeira, A.; Gattass, C. R., Perillyl alcohol induces apoptosis in human glioblastoma multiforme cells. *Oncol Rep* **2005**, *13* (5), 943-7.
19. Teruszkin Balassiano, I.; Alves de Paulo, S.; Henriques Silva, N.; Curie Cabral, M.; Gibaldi, D.; Bozza, M.; Orlando da Fonseca, C.; Da Gloria da Costa Carvalho, M., Effects of perillyl alcohol in glial C6 cell line in vitro and anti-metastatic activity in chorioallantoic membrane model. *Int J Mol Med* **2002**, *10* (6), 785-8.
20. Azzoli, C. G.; Miller, V. A.; Ng, K. K.; Krug, L. M.; Spriggs, D. R.; Tong, W. P.; Riedel, E. R.; Kris, M. G., A phase I trial of perillyl alcohol in patients with advanced solid tumors. *Cancer Chemother Pharmacol* **2003**, *51* (6), 493-8.
21. Cho, H. Y.; Wang, W. J.; Jhaveri, N.; Torres, S.; Tseng, J.; Leong, M. N.; Lee, D. J.; Goldkorn, A.; Xu, T.; Petasis, N. A.; Louie, S. G.; Schonthal, A. H.; Hofman, F. M.; Chen, T. C., Perillyl Alcohol for the Treatment of Temozolomide-Resistant Gliomas. *Mol Cancer Ther* **2012**, *11* (11), 2462-2472.
22. Bailey, H. H.; Levy, D.; Harris, L. S.; Schink, J. C.; Foss, F.; Beatty, P.; Wadler, S., A phase II trial of daily perillyl alcohol in patients with advanced ovarian cancer: Eastern Cooperative Oncology Group study E2E96. *Gynecol Oncol* **2002**, *85* (3), 464-468.

23. Hudes, G. R.; Szarka, C. E.; Adams, A.; Ranganathan, S.; McCauley, R. A.; Weiner, L. M.; Langer, C. J.; Litwin, S.; Yeslow, G.; Halber, T.; Qian, M.; Gallo, J. M., Phase I pharmacokinetic trial of perillyl alcohol (NSC 641066) in patients with refractory solid malignancies. *Clin Cancer Res* **2000**, *6* (8), 3071-80.
24. Wang, H.; Yapa, A. S.; Kariyawasam, N.; Shrestha, T. B.; Wendel, S. O.; Yu, J.; Pyle, M.; Basel, M. T.; Malalasekera, A. P.; Toledo, Y.; Ortega, R.; Thapa, P. S.; Huang, H.; Sun, S. X.; Smith, P. E.; Troyer, D. L.; Bossmann, S. H., Rationally Designed Peptide Nanosponges for Cell-Based Cancer Therapy. *Nanomedicine NBM* **2017**, *submitted*.
25. Yapa, A. S.; Wang, H.; Wendel, S. O.; Shrestha, T. B.; Kariyawasam, N.; Perera, A.; Pyle, M.; Basel, M. T.; Malalasekera, A. P.; Manawadu, H.; Yu, J.; Toledo, Y.; Ortega, R.; Thapa, P. S.; Smith, P. E.; Troyer, D. L.; Bossmann, S. H., Peptide Nanosponges Designed for Rapid Uptake by Stem Cells and Leukocytes. *ACS Nano* **2017**, *submitted*.
26. Cui, H.; Webber, M. J.; Stupp, S. I., Self-assembly of peptide amphiphiles: from molecules to nanostructures to biomaterials. *Biopolymers* **2010**, *94* (1), 1-18.
27. Gudlur, S.; Sukthankar, P.; Gao, J.; Avila, L. A.; Hiromasa, Y.; Chen, J.; Iwamoto, T.; Tomich, J. M., Peptide nanovesicles formed by the self-assembly of branched amphiphilic peptides. *PLoS One* **2012**, *7* (9), e45374.
28. Mohamed, A. S., K.; Chaves, E. P. , The Mevalonate Pathway in Alzheimer's Disease — Cholesterol and Non-Sterol Isoprenoids. In *Alzheimer's Disease - Challenges for the Future*, Zerr, I., Ed. 2015.
29. Takemoto, M.; Liao, J. K., Pleiotropic effects of 3-hydroxy-3-methylglutaryl coenzyme A reductase inhibitors. *Arterioscl Throm Vas* **2001**, *21* (11), 1712-1719.
30. Rogers, T. L.; Holen, I., Tumour macrophages as potential targets of bisphosphonates. *J Transl Med* **2011**, *9*.
31. Buhaescu, I.; Izzedine, H., Mevalonate pathway: A review of clinical and therapeutical implications. *Clin Biochem* **2007**, *40* (9-10), 575-584.
32. Commons, C. Mevalonate pathway.  
[https://upload.wikimedia.org/wikipedia/commons/b/b4/Mevalonate\\_pathway.svg](https://upload.wikimedia.org/wikipedia/commons/b/b4/Mevalonate_pathway.svg)  
(accessed 03/07/2017).
33. Linder, M.; Tschernig, T., Vasculogenic mimicry: Possible role of effector caspase-3, caspase-6 and caspase-7. *Ann Anat* **2016**, *204*, 114-7.
34. Fontaine, S. D.; Reid, R.; Robinson, L.; Ashley, G. W.; Santi, D. V., Long-Term Stabilization of Maleimide-Thiol Conjugates. *Bioconjugate Chem.* **2015**, *26* (1), 145-152.
35. Holowka, E. P.; Pochan, D. J.; Deming, T. J., Charged polypeptide vesicles with controllable diameter. *J Am Chem Soc* **2005**, *127* (35), 12423-12428.

36. Sukthankar, P.; Gudlur, S.; Avila, L. A.; Whitaker, S. K.; Katz, B. B.; Hiromasa, Y.; Gao, J.; Thapa, P.; Moore, D.; Iwamoto, T.; Chen, J. H.; Tomich, J. M., Branched Oligopeptides Form Nanocapsules with Lipid Vesicle Characteristics. *Langmuir* **2013**, *29* (47), 14648-14654.
37. Taheri, A.; Dinarvand, R.; Atyabi, F.; Nouri, F.; Ahadi, F.; Ghahremani, M. H.; Ostad, S. N.; Borougeni, A. T.; Mansoori, P., Targeted delivery of methotrexate to tumor cells using biotin functionalized methotrexate-human serum albumin conjugated nanoparticles. *J. Biomed. Nanotechnol.* **2011**, *7* (6), 743-753.
38. Najbauer, J.; Danks, M. K.; Schmidt, N.-O.; Kim, S. U.; Aboody, K. S. In *Neural stem cell-mediated therapy of primary and metastatic solid tumors*, World Scientific Publishing Co. Pte. Ltd.: 2008; pp 335-372.
39. Croy, S. R.; Kwon, G. S., Polymeric micelles for drug delivery. *Curr. Pharm. Des.* **2006**, *12* (36), 4669-4684.
40. Amblard, M.; Fehrentz, J. A.; Martinez, J.; Subra, G., Methods and Protocols of modern solid phase peptide synthesis. *Mol Biotechnol* **2006**, *33* (3), 239-254.
41. Perera, A. S.; Wang, H.; Basel, M. T.; Pokhrel, M. R.; Gamage, P. S.; Kalita, M.; Wendel, S.; Sears, B.; Welideniya, D.; Liu, Y.; Turro, C.; Troyer, D. L.; Bossmann, S. H., Channel Blocking of MspA Revisited. *Langmuir* **2013**, *29* (1), 308-315.
42. Stockert, J. C.; Blazquez-Castro, A.; Canete, M.; Horobin, R. W.; Villanueva, A., MTT assay for cell viability: Intracellular localization of the formazan product is in lipid droplets. *Acta Histochem.* **2012**, *114* (8), 785-796.
43. Rachakatla, R. S.; Balivada, S.; Seo, G.-M.; Myers, C. B.; Wang, H.; Samarakoon, T. N.; Dani, R.; Pyle, M.; Kroh, F. O.; Walker, B.; Leaym, X.; Koper, O. B.; Chikan, V.; Bossmann, S. H.; Tamura, M.; Troyer, D. L., Attenuation of Mouse Melanoma by A/C Magnetic Field after Delivery of Bi-Magnetic Nanoparticles by Neural Progenitor Cells. *ACS Nano* **2010**, *4* (12), 7093-7104.
44. Ourednik, J.; Ourednik, V.; Lynch, W. P.; Schachner, M.; Snyder, E. Y., Neural stem cells display an inherent mechanism for rescuing dysfunctional neurons. *Nat. Biotechnol.* **2002**, *20* (11), 1103-1110.
45. Oh, T.; Fakurnejad, S.; Sayegh, E. T.; Clark, A. J.; Ivan, M. E.; Sun, M. Z.; Safaee, M.; Bloch, O.; James, C. D.; Parsa, A. T., Immunocompetent murine models for the study of glioblastoma immunotherapy. *J. Transl. Med.* **2014**, *12*, 107/1-107/10, 10.
46. Welch, B. L., The Generalization of Students Problem When Several Different Population Variances Are Involved. *Biometrika* **1947**, *34* (1-2), 28-35.
47. Duban, M. E.; Bures, M. G.; DeLazzer, J.; Martin, Y. C. In *Virtual screening of molecular properties: A comparison of log P calculators*, Verlag Helvetica Chimica Acta: 2001; pp 485-497.

48. Schneider, H.-J. In *Ionic interactions in supramolecular complexes*, John Wiley & Sons, Inc.: 2012; pp 35-47.
49. <https://www.graphpad.com/scientific-software/prism/>.

## Appendix A - For Chapter 1

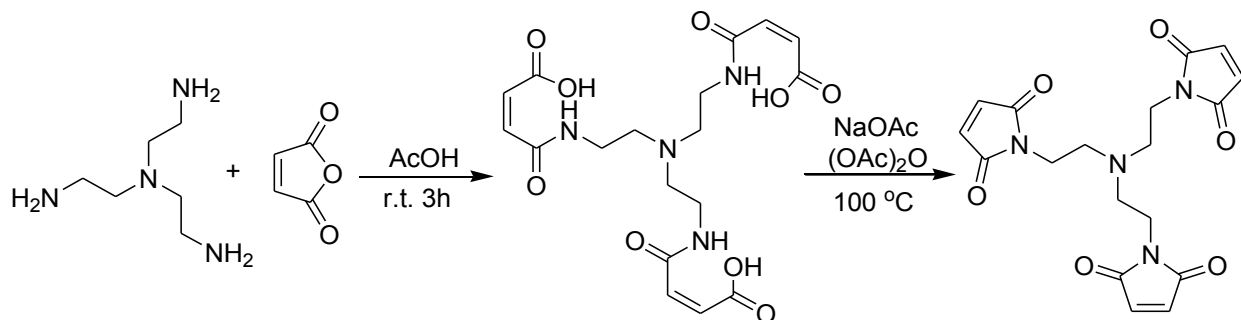


**Figure A.1** Synthesis of a tri-maleimide scaffold with trigonal symmetry

Tris(2-aminoethyl)amine (1.46 g, 10 mmol) and maleic anhydride (3.23 g, 33 mmol) were suspended in 30 mL of acetic acid and allowed to react for 3 h at RT. The resulting white precipitate was collected by filtration, washed with cold water and dried. 4.10 g trimaleimic acid adduct was obtained. (93% yield).

Ring closure was achieved by the following procedure. Trimaleimic acid adduct (220 mg, 0.5 mmol) and sodium acetate (410 mg, 5 mmol) were suspended in 10 mL acetic anhydride, and allowed to react at 100 °C for 3 h. After cooling to RT, 5 mL of water was added, and the mixture were stirred at RT for 10 min. Solvents were removed by rotavap, and the solid residue was dissolved in 15 mL ethyl acetate, washed with water (5mL, 2 times), saturated NaHCO<sub>3</sub> (5mL 2 times), and brine (5mL 1 time). The organic phase was further dried with anhydrous MgSO<sub>4</sub>, and concentrated to dryness. 186 mg pure product was obtained. (96% yield) <sup>1</sup>H NMR (CDCl<sub>3</sub>) δ: 2.67 (t, 6H); 3.52 (t, 6H); 6.65 (s, 6H). <sup>13</sup>C NMR (CDCl<sub>3</sub>) δ: 36.2, 52.0, 135.0, 171.5.

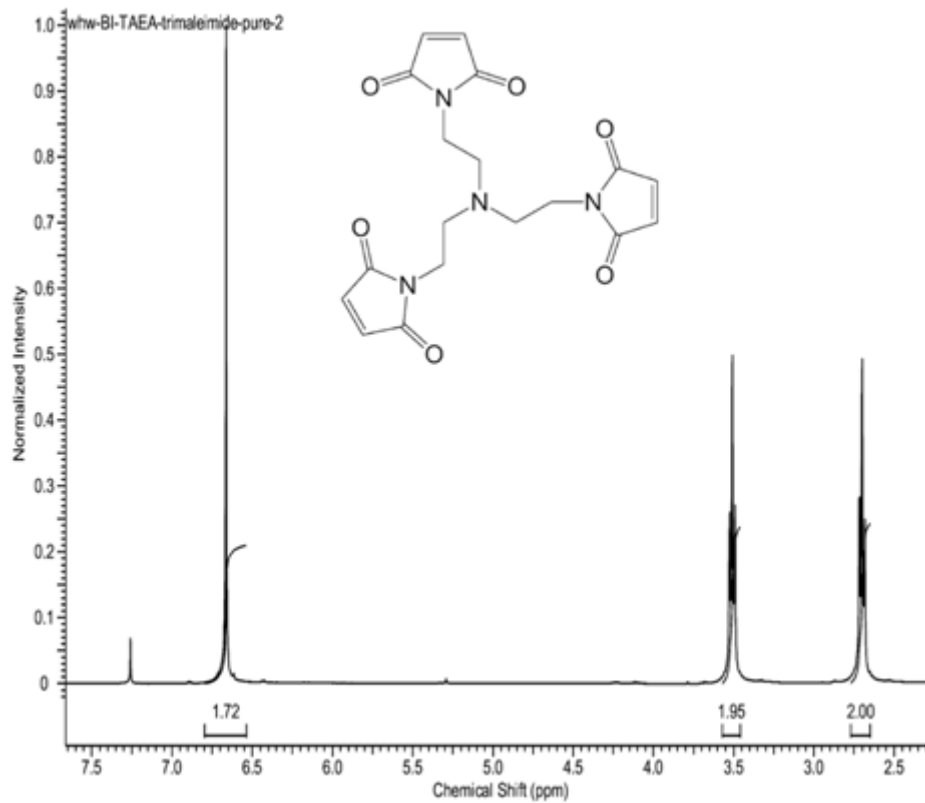
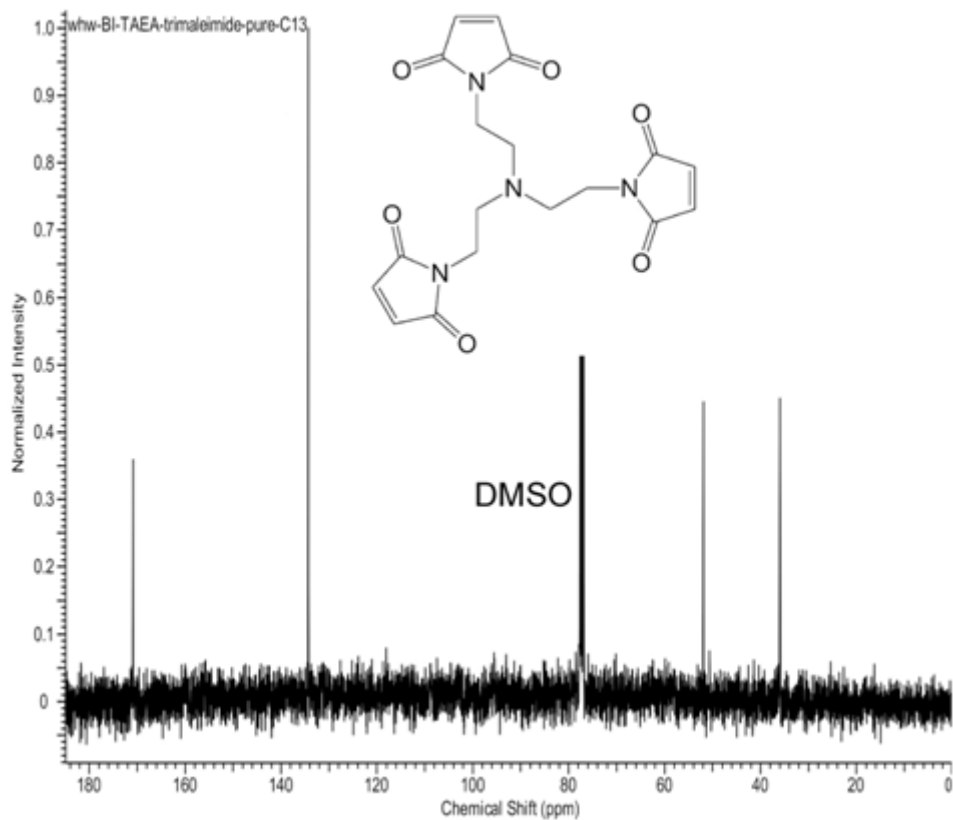
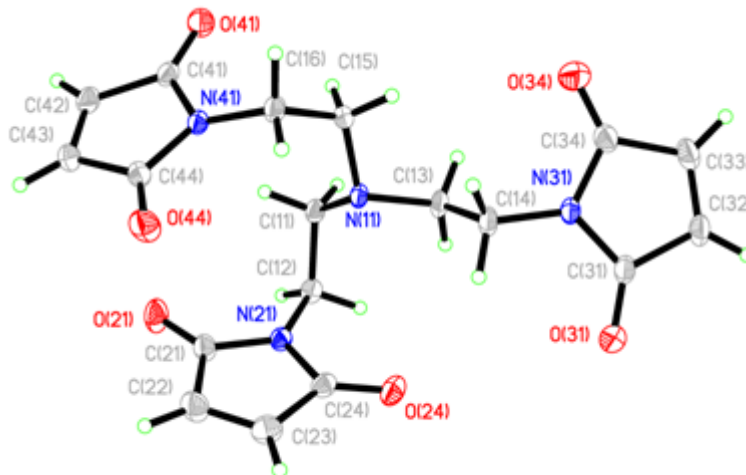


Figure A.2  $^1\text{H-NMR}$  spectrum of the maleimide scaffold (Varian, 400 MHz).



**Figure A.3**  $^{13}\text{C}$ -NMR spectrum of the maleimide scaffold (Varian, 400 MHz).

Single crystals of the maleimide scaffold were obtained in saturated ethyl acetate solution. Because of the two methylene bridges between the center nitrogen atom and the maleimide moieties, the structure is flexible.



**Figure A.4 Crystal structure of tri-maleimide**

### **Peptide Synthesis and Cholesterol-(K)<sub>n</sub>DEVDC, Cholesterol-(D)<sub>n</sub>DEVDC Synthesis**

Different lengths of poly K and D (n=5, 10, 15, 20, 25) peptides were synthesized by standard solid phase peptide synthesis method. Cholesterol was introduced to the peptide by CDI (carbonyl-bis-minidazol) activation of the OH of cholesterol first, and then further reacting with the NH<sub>2</sub> group of the terminal amino acid. After cleavage from the solid phase, product obtained were further purified by conducting reversed-phase HPLC, using a preparative C18 column, eluting with a linear gradient of 0.05% formic acid in CH<sub>3</sub>CN and 0.1% formic acid in water (5/95 to 95/5 over 60 min.)

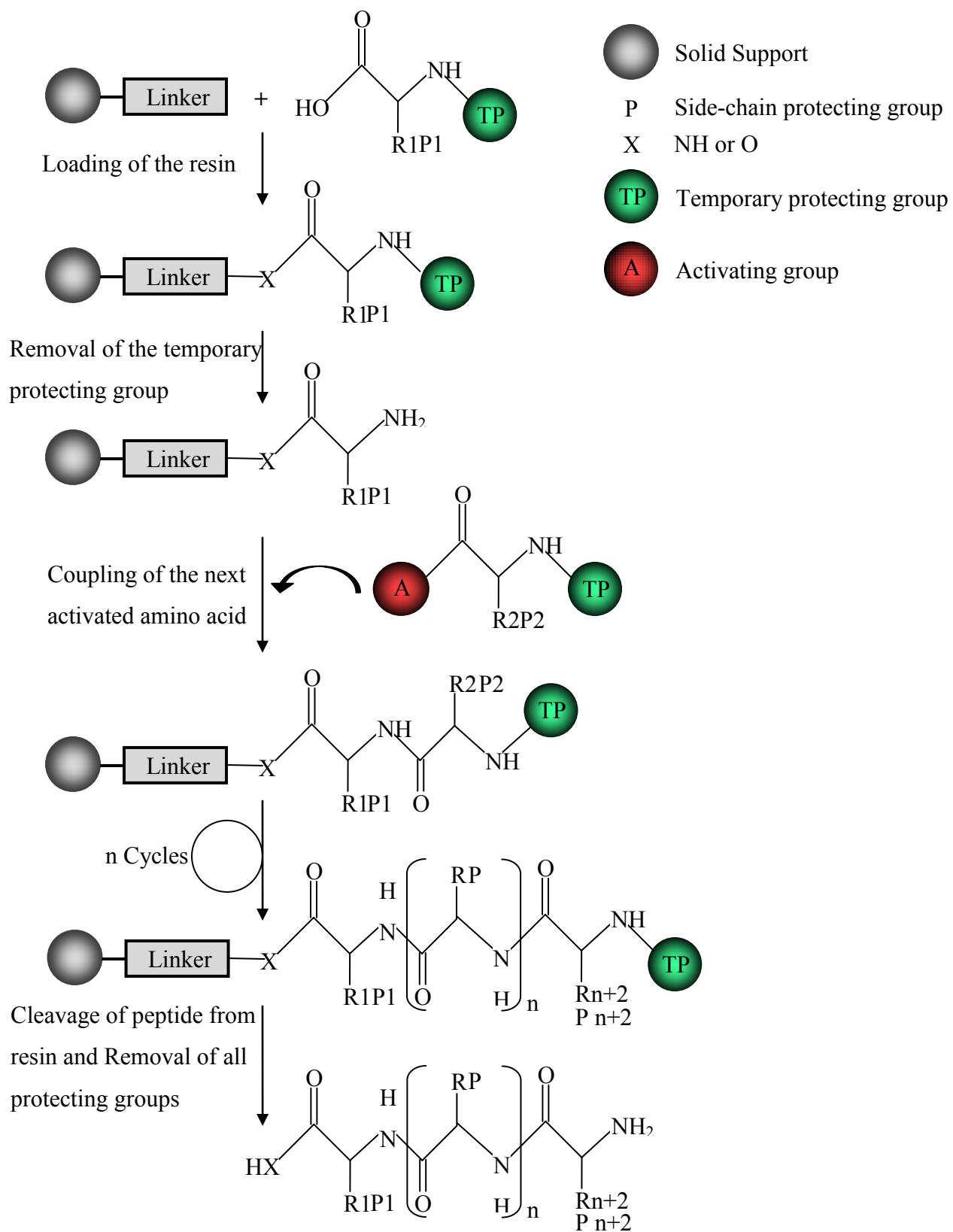


**Figure A.5 Main steps of solid phase peptide synthesis<sup>1</sup>**

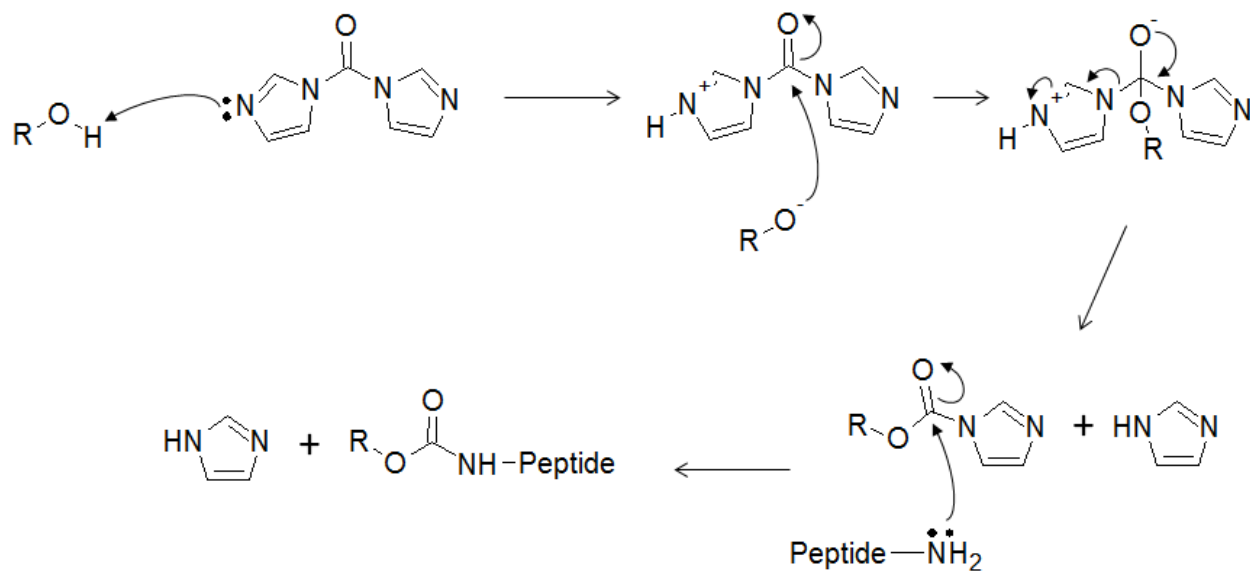


Figure A.6 CDI activated cholesterol coupling to peptide chains

### Structures of Resin and Amino Acids Used for Nanosponge Synthesis

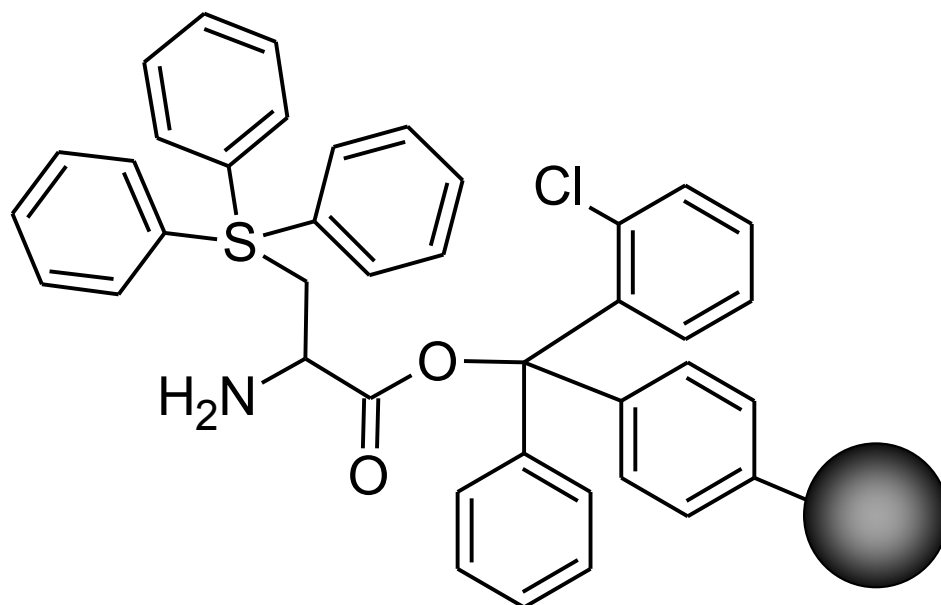


Figure A.7 H-Cys(Trt)-2-ClTrt resin

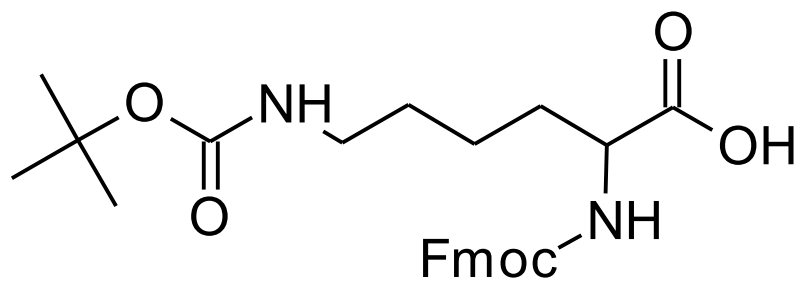


Figure A.8 Fmoc-Lys(Boc)-OH (K)

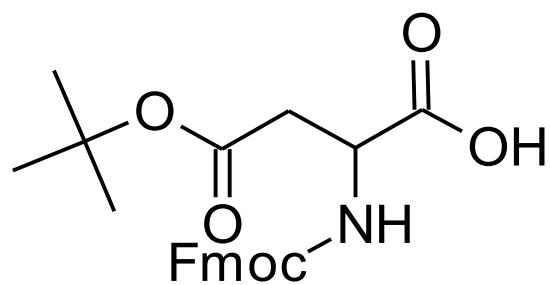


Figure A.9 Fmoc-Asp(OtBu)-OH (D)

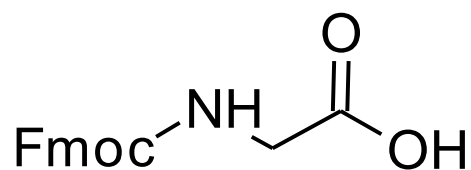


Figure A.10 Fmoc-Gly-OH (G)

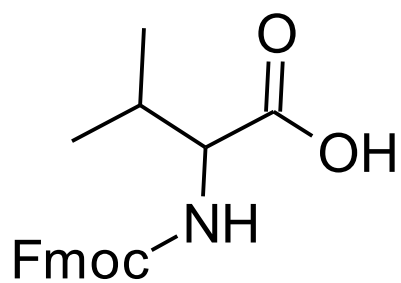


Figure A.11 Fmoc-L-valine (V)

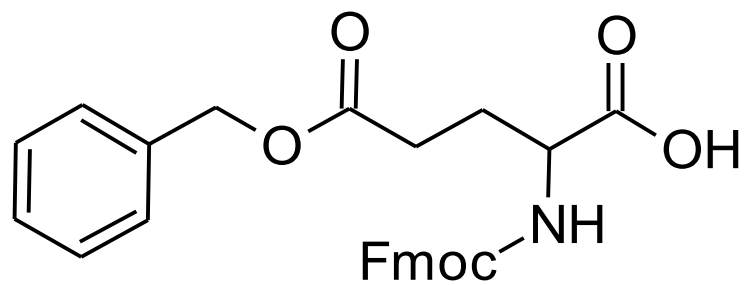


Figure A.12 Fmoc-Glu(OBzl)-OH (E)

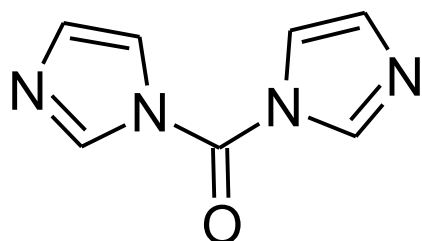


Figure A.13 CDI: 1,1'-Carbonyldiimidazole

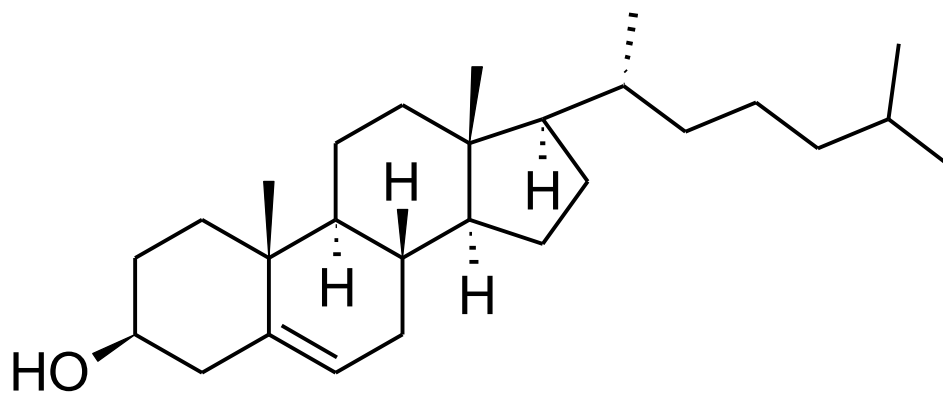


Figure A.14 Cholesterol

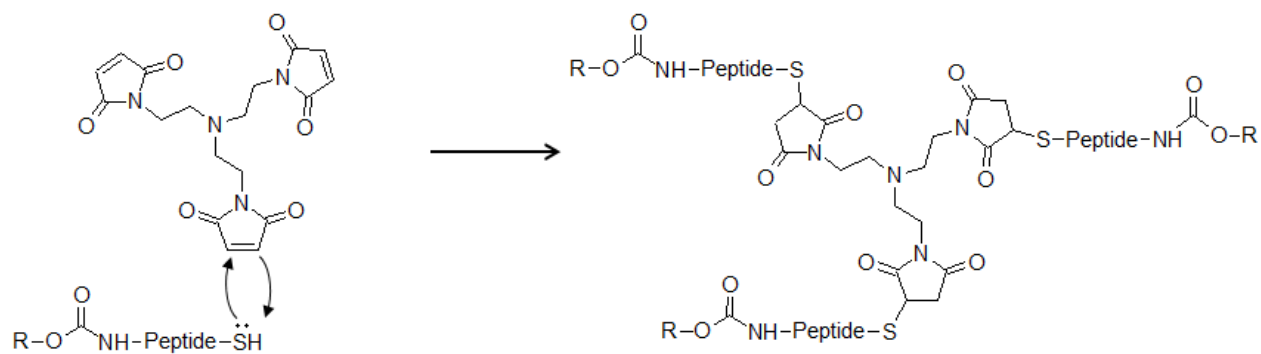
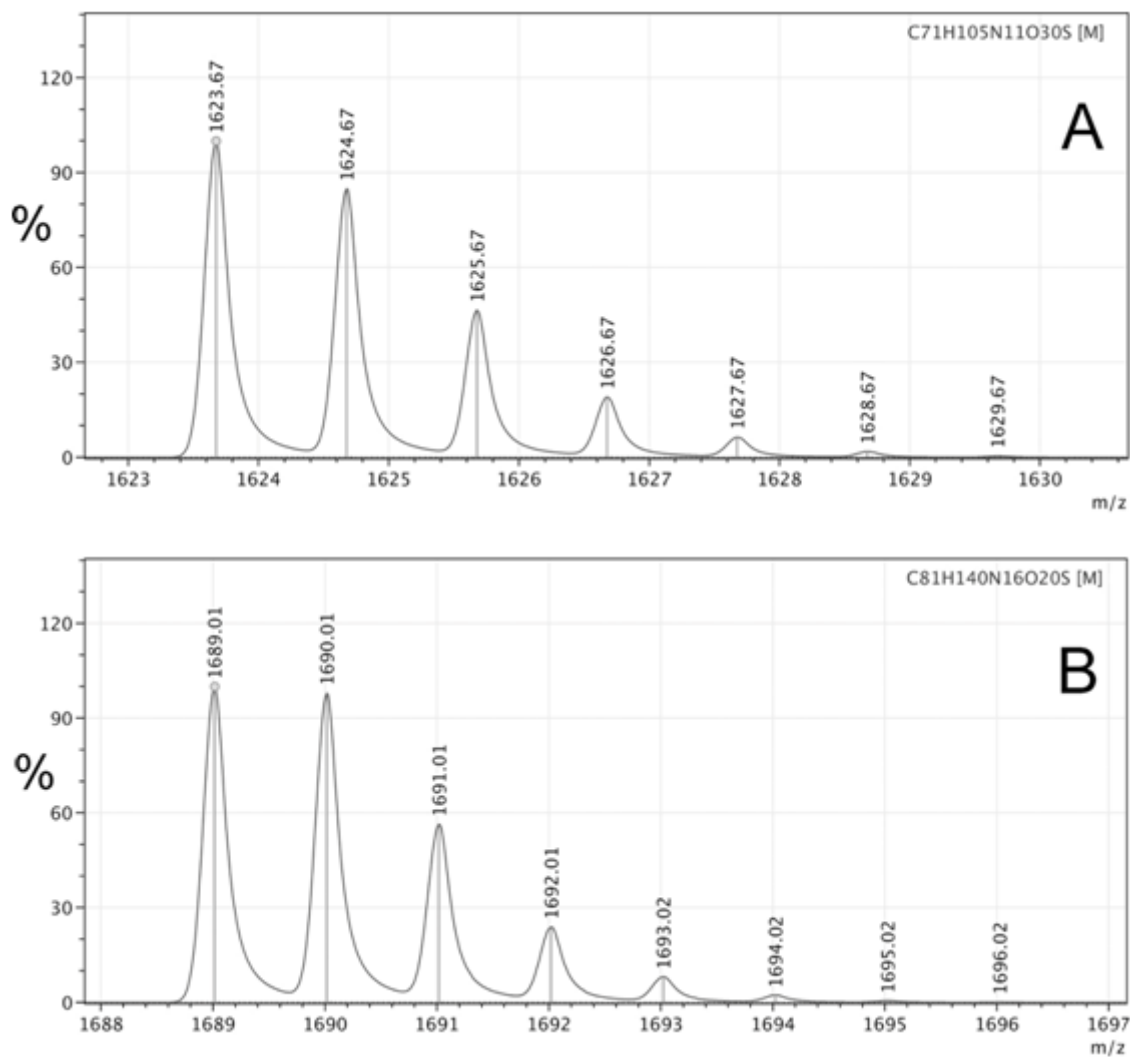
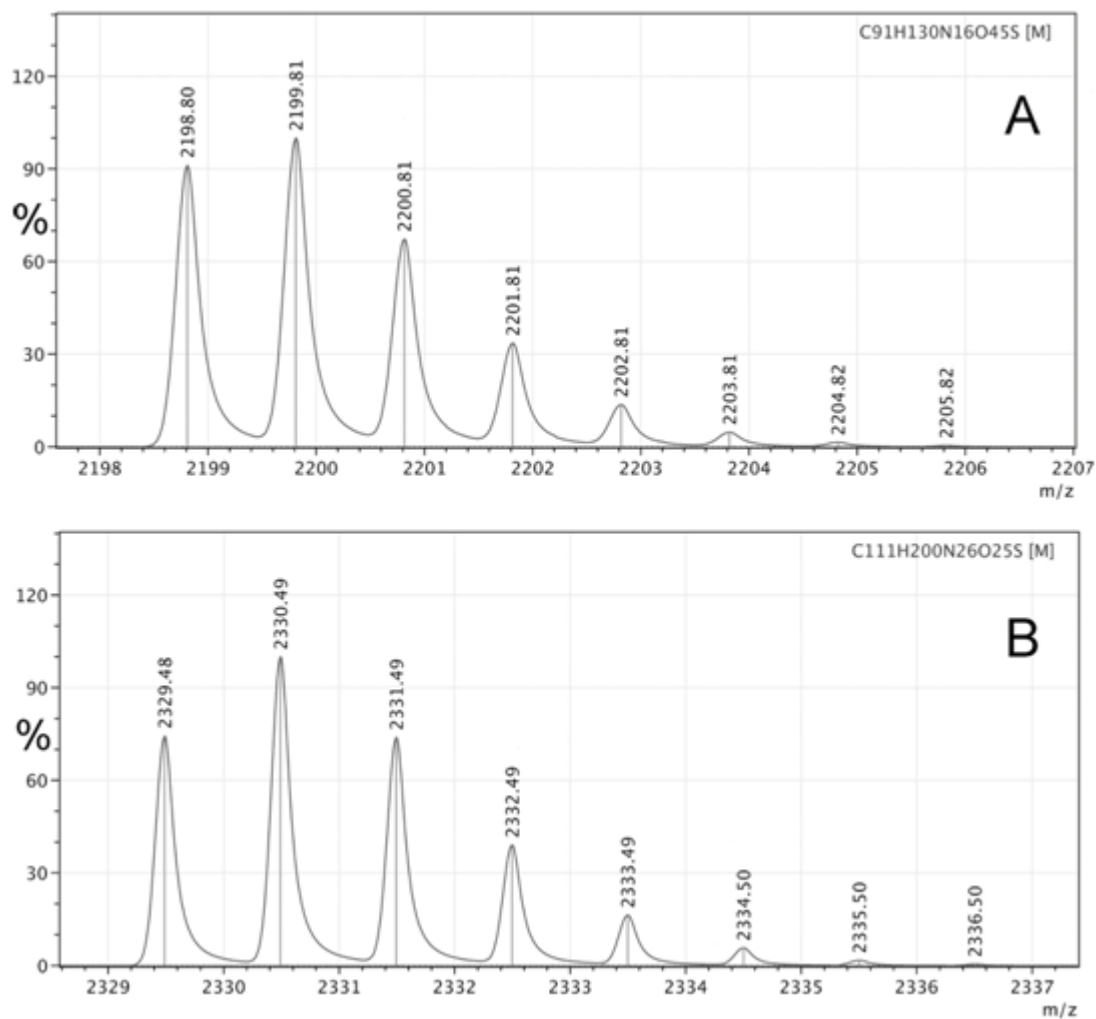
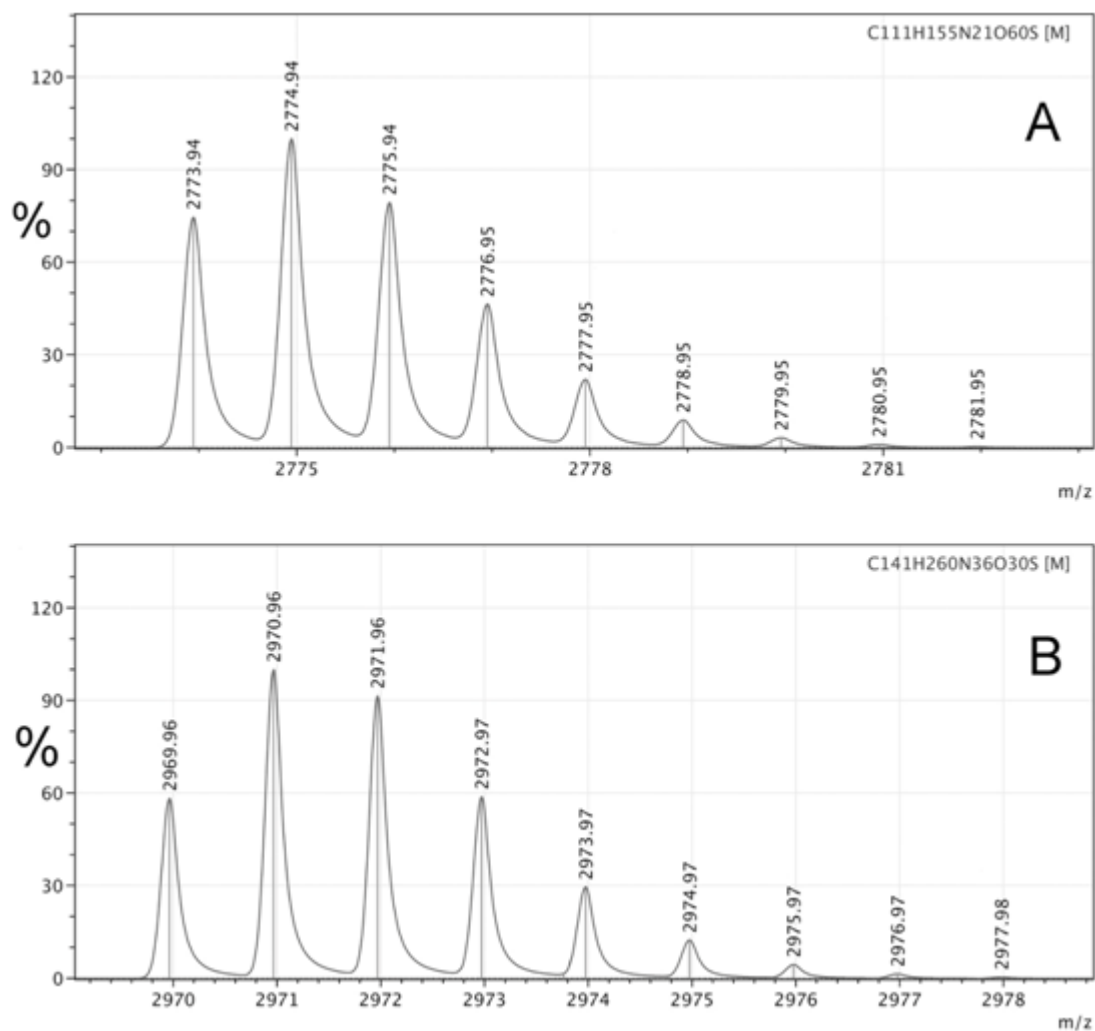


Figure A.15 Cholesterol-Peptide-Trimaleimide Adduct Formation



**Figure A.16 MALDI-TOF (Voyager DE STRT) of A: Cholesterol-(D)<sub>5</sub>DEVDC, the isotope distribution is consistent with the chemical formula C<sub>71</sub>H<sub>105</sub>N<sub>11</sub>O<sub>30</sub>S; B: Cholesterol-(K)<sub>5</sub>DEVDC, the isotope distribution is consistent with the chemical formula C<sub>81</sub>H<sub>140</sub>N<sub>16</sub>O<sub>20</sub>S.**





**Figure A.18 MALDI-TOF ((Voyager DE STRT) of A: Cholesterol-(D)<sub>15</sub>DEVDC, the isotope distribution is consistent with the chemical formula C<sub>111</sub>H<sub>155</sub>N<sub>21</sub>O<sub>60</sub>S; B: Cholesterol-(K)<sub>15</sub>DEVDC, the isotope distribution is consistent with the chemical formula C<sub>141</sub>H<sub>260</sub>N<sub>36</sub>O<sub>30</sub>S.**

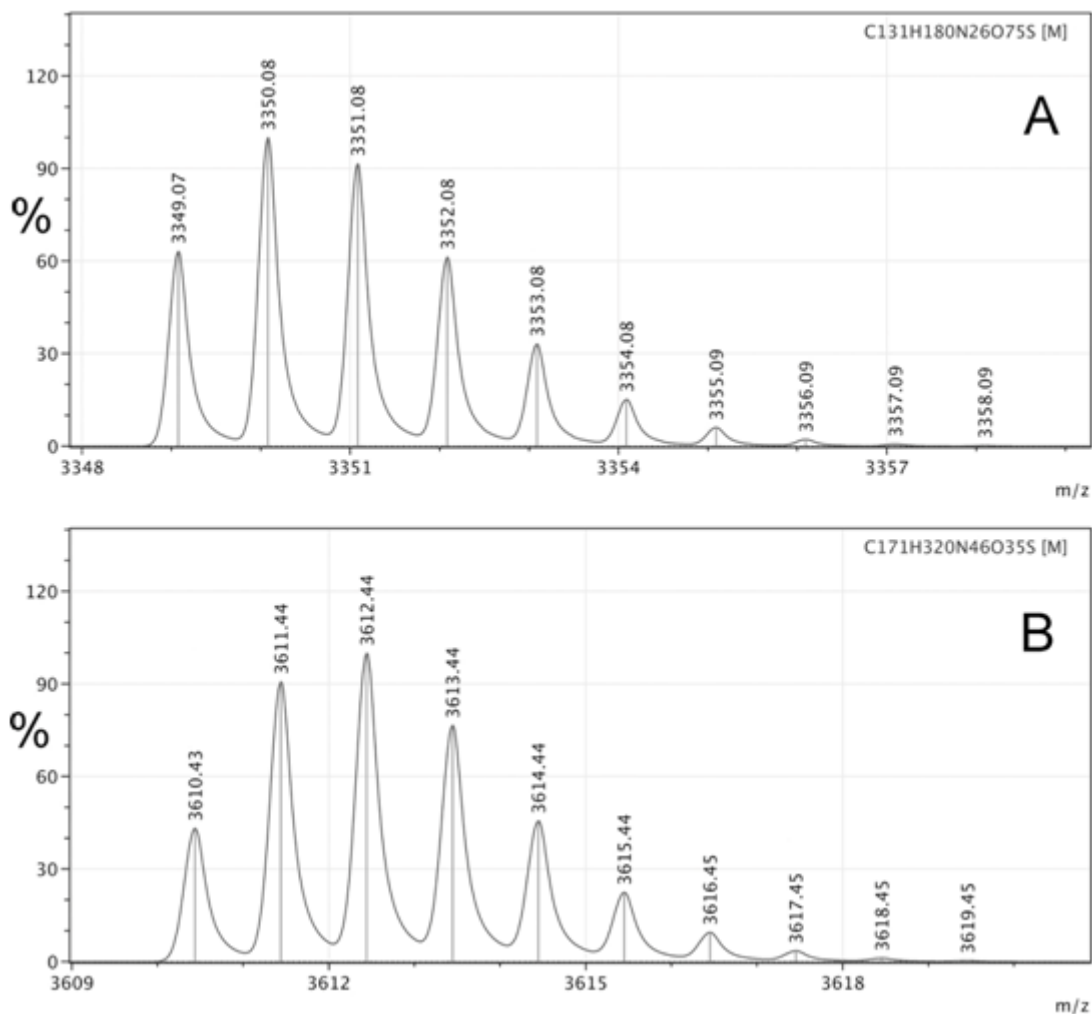


**Figure A.19 MALDI-TOF ((Voyager DE STRT) of A: Cholesterol-(D)<sub>20</sub>DEVDC, the isotope distribution is consistent with the chemical formula C<sub>131</sub>H<sub>180</sub>N<sub>26</sub>O<sub>75</sub>S; B: Cholesterol-(K)<sub>20</sub>DEVDC, the isotope distribution is consistent with the chemical formula C<sub>171</sub>H<sub>320</sub>N<sub>46</sub>O<sub>35</sub>S.**

### Dynamic Light Scattering (DLS)

Correlation curves and number-averaged size distributions for (cholesterol-(K)<sub>n</sub>DEVDC)<sub>3</sub>-trialeimide + (cholesterol-(D)<sub>n</sub>DEVDC)<sub>3</sub>-trialeimide nanosponges (0.050 mM of each component in PBS) are shown in Figures A.19 (n=15) and A.20 (n=20).

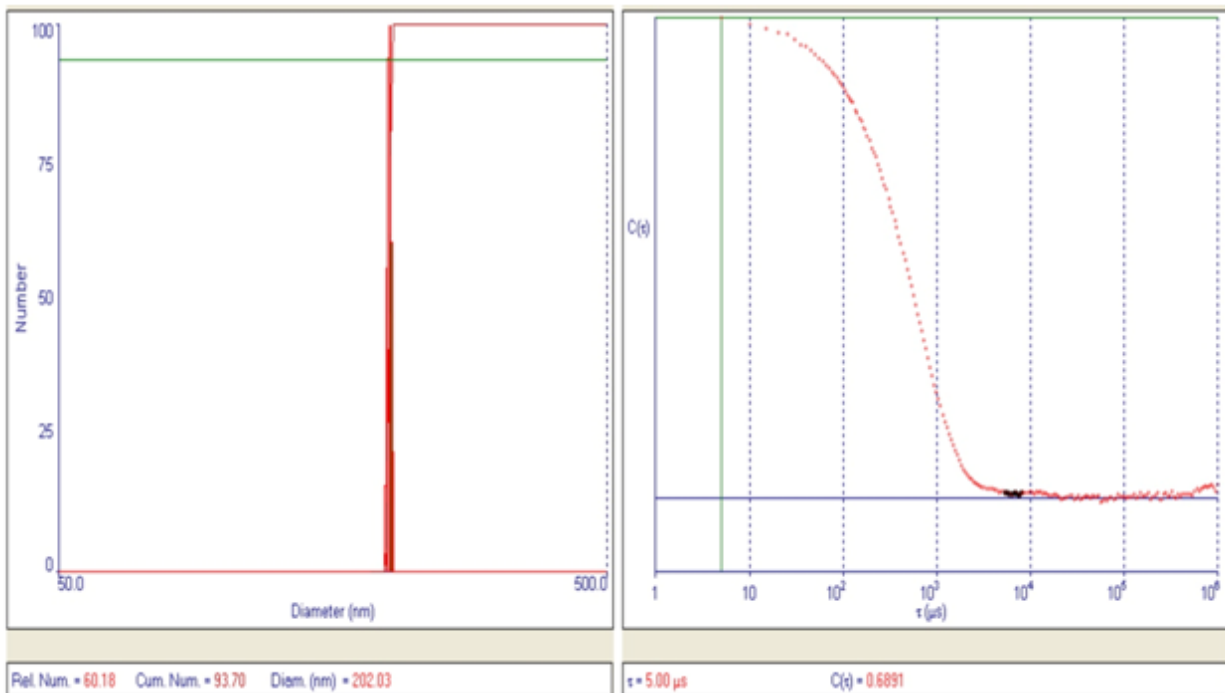


Figure A.20 Number-averaged size distributions and correlation curve for n=15.

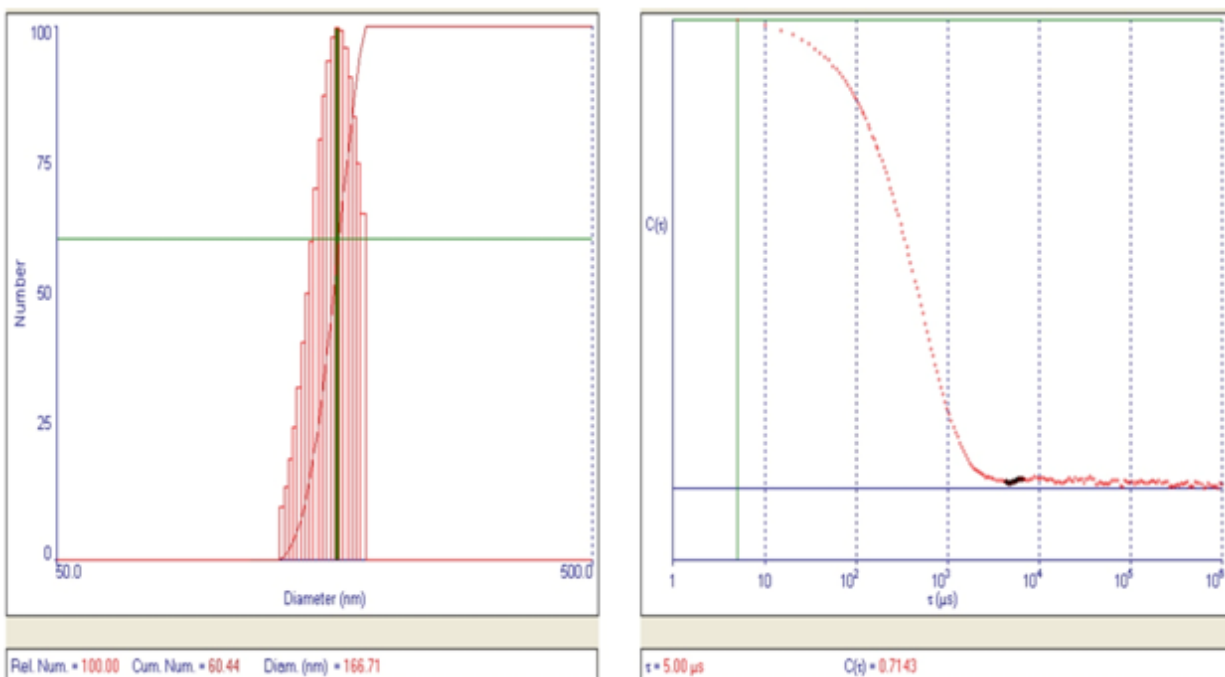
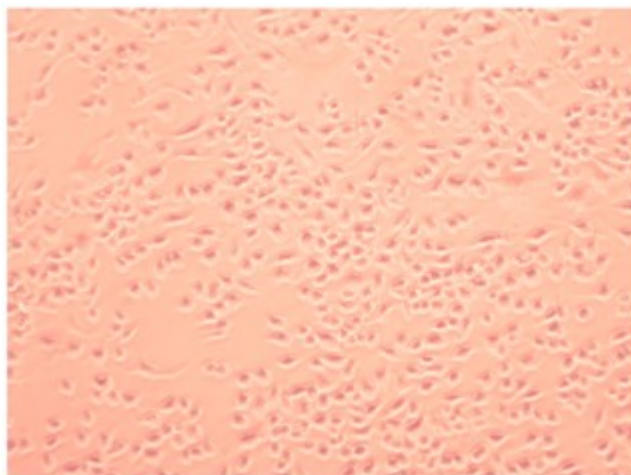


Figure A.21 Number-averaged size distributions and correlation curve for n=20.

## Simulation Details

Classical molecular dynamics were performed using the gromacs software.<sup>2</sup> Simulations using the united atom Gromos FF were performed in the NpT ensemble at 300 K and 1 bar using the v-rescale and Berendsen temperature and pressure algorithms,<sup>3-4</sup> respectively. Electrostatic interactions were evaluated using the particle mesh Ewald approach,<sup>5</sup> while van der Waals interactions were truncated at 1.5 nm. The timestep was 2 fs and all solute bonds were constrained using Lincs,<sup>6</sup> while all solvent bonds (and angles) were constrained using Settle.<sup>7</sup> The CG simulations were also performed in the NpT ensemble at 310 K and 1 bar using the v-rescale and Parrinello-Rahman temperature and pressure algorithms,<sup>3, 8</sup> respectively, as suggested by the MARTINI FF developers (<http://www.cgmartini.nl/>). Electrostatic and van der Waals interactions were evaluated using shifted potentials with a relative permittivity of 15.<sup>9</sup> The timestep was 25 fs and all solute bonds were constrained using Lincs. The CG simulations were checked to ensure there was no freezing of water beads by calculating the diffusion constants of water periodically during the simulations. A variety of system sizes were simulated with the largest involving 108 tri-Lys and 108 tri-Asp molecules, 2376 sodium ions, and 776763 water beads in a 45nm cube box for 4  $\mu$ s.

## Cell Experiments



**Figure A.22** RAW264.7 cells after 2h of incubation with PKH26 ( $1 \times 10^{-5} \text{M}$ ), as described in the Experimental Section. Homogeneous staining is clearly observed, in contrast to staining via nanosponge uptake (see Figure 1.7).

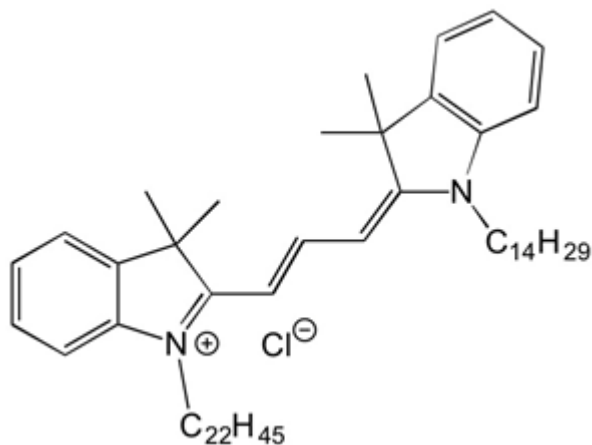


**Figure A.23** Chemical structure of PKH26, which is – technically – a Cyanine 3.0 dye.

## Appendix B - For Chapter 2

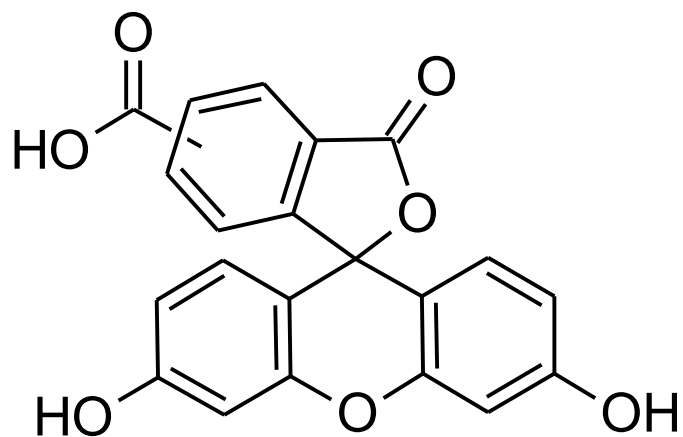


Figure B.1 5(6)-Carboxyfluorescein

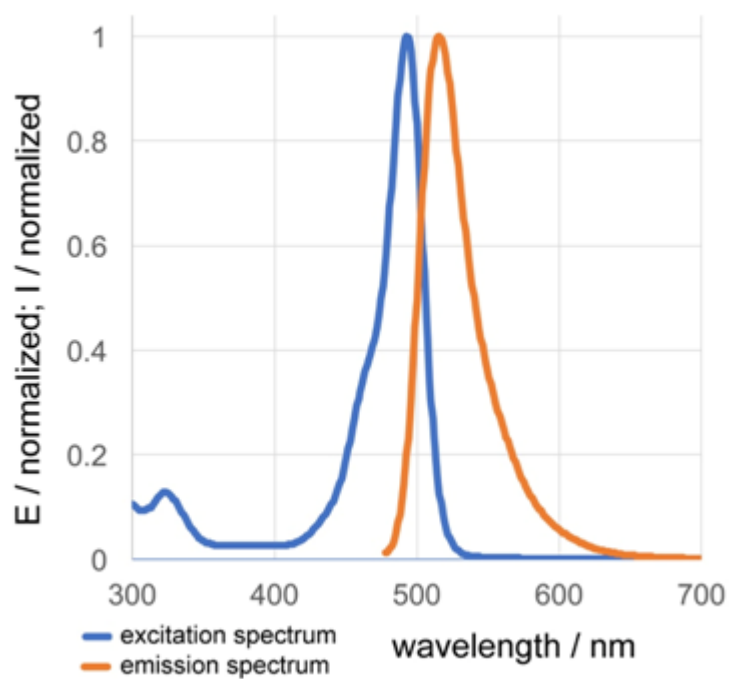


Figure B.2 Excitation and emission spectrum of 5(6)-carboxyfluorescein in PBS (pH = 7.4).

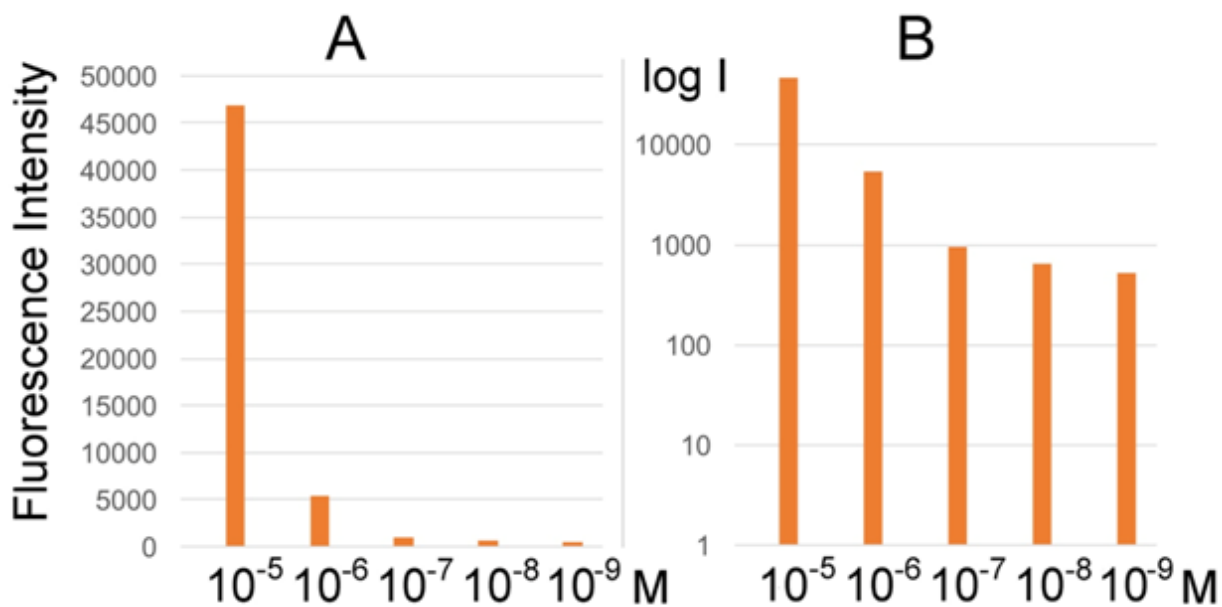


Figure B.3 Concentration dependence of the emission of 5(6)-carboxyfluorescein fluorescence in PBS, BioTek Synergy H1,  $\lambda_{EX} = 482$ ,  $\lambda_{EM} = 525$  nm.

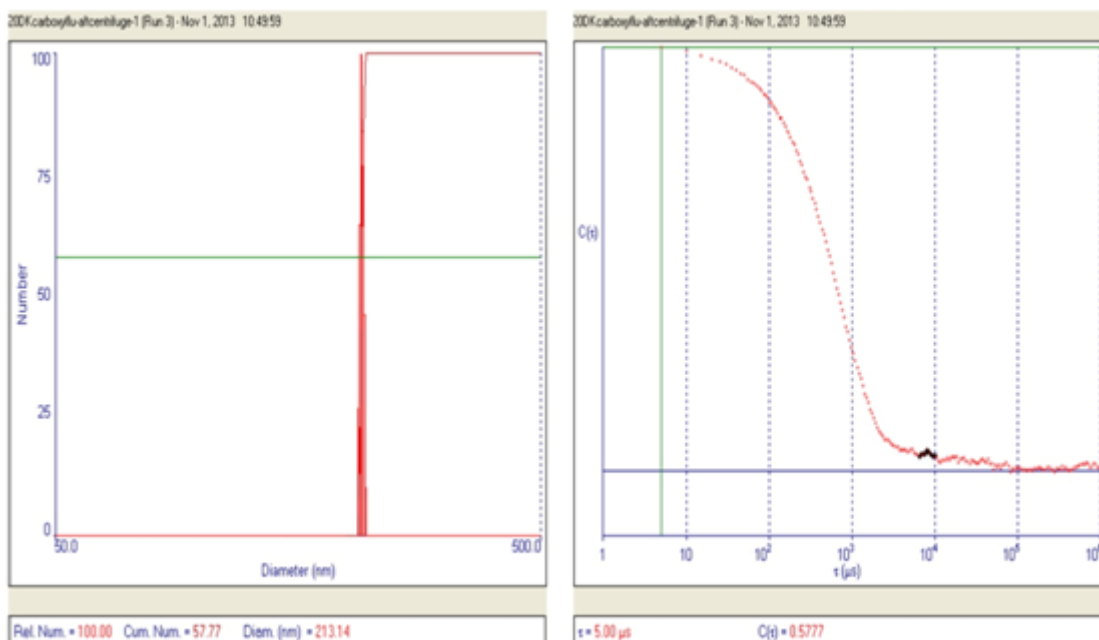


Figure B.4 DLS of 5(6)-Carboxyfluorescein-loaded type DK 20 nanosponges. The average diameter of the peptide nanovesicles formed is  $213 \pm 25$  nm. The nanovesicles remained stable during 24h.

## Appendix C - For Chapter 3

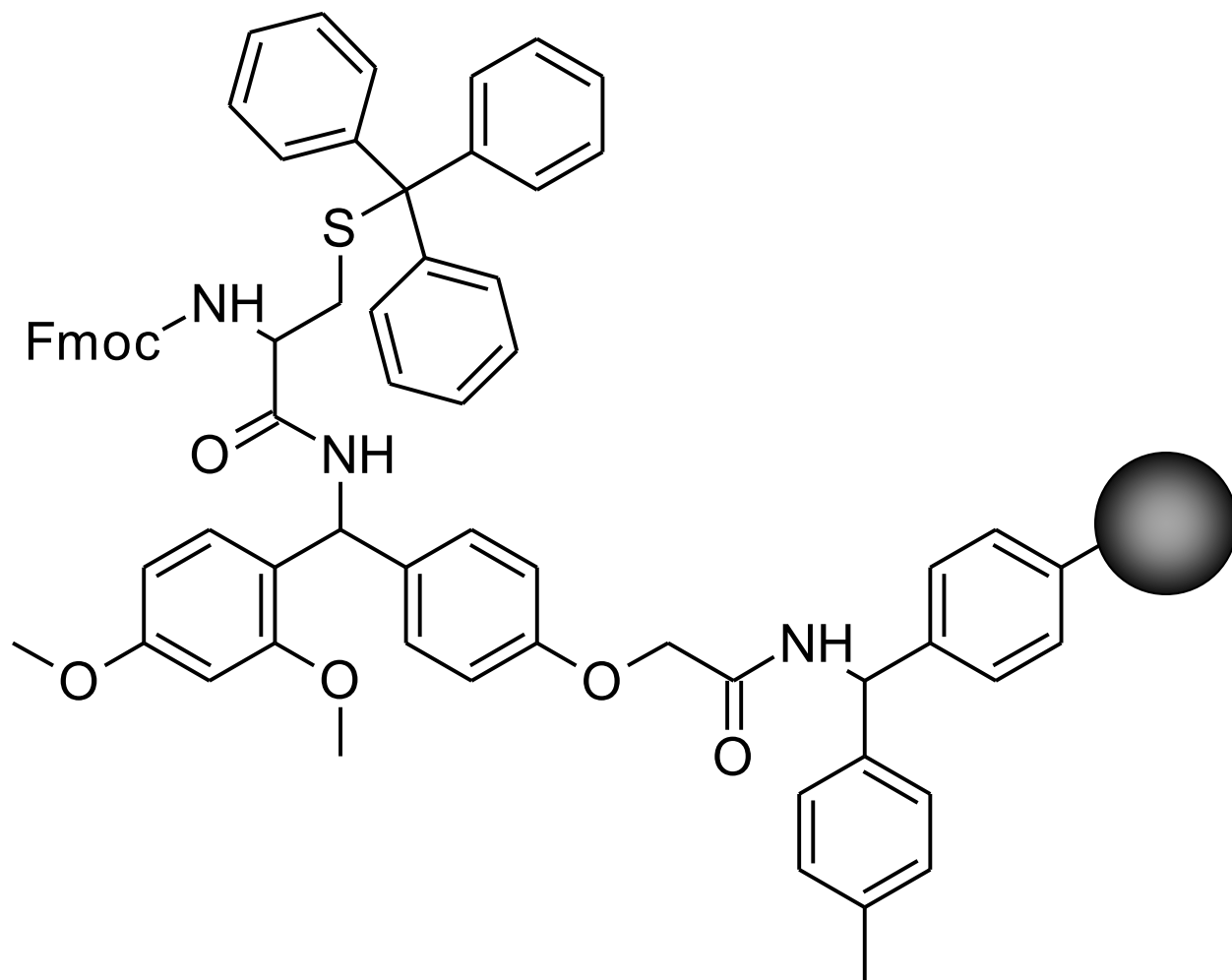


Figure C.1 Fmoc-Cys(Trt)-Rink Amide MBHA resin

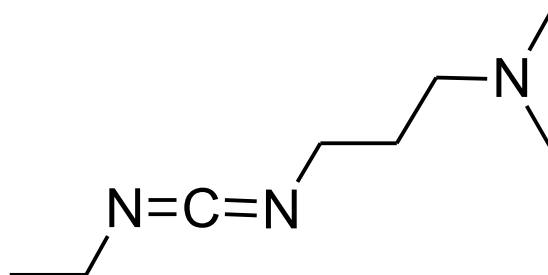


Figure C.2 EDC: 1-Ethyl-3-(3-dimethylaminopropyl)carbodiimide

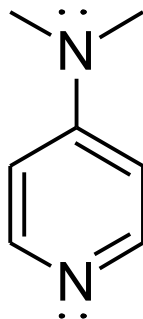


Figure C.3 DMAP: 4-Dimethylaminopyridine

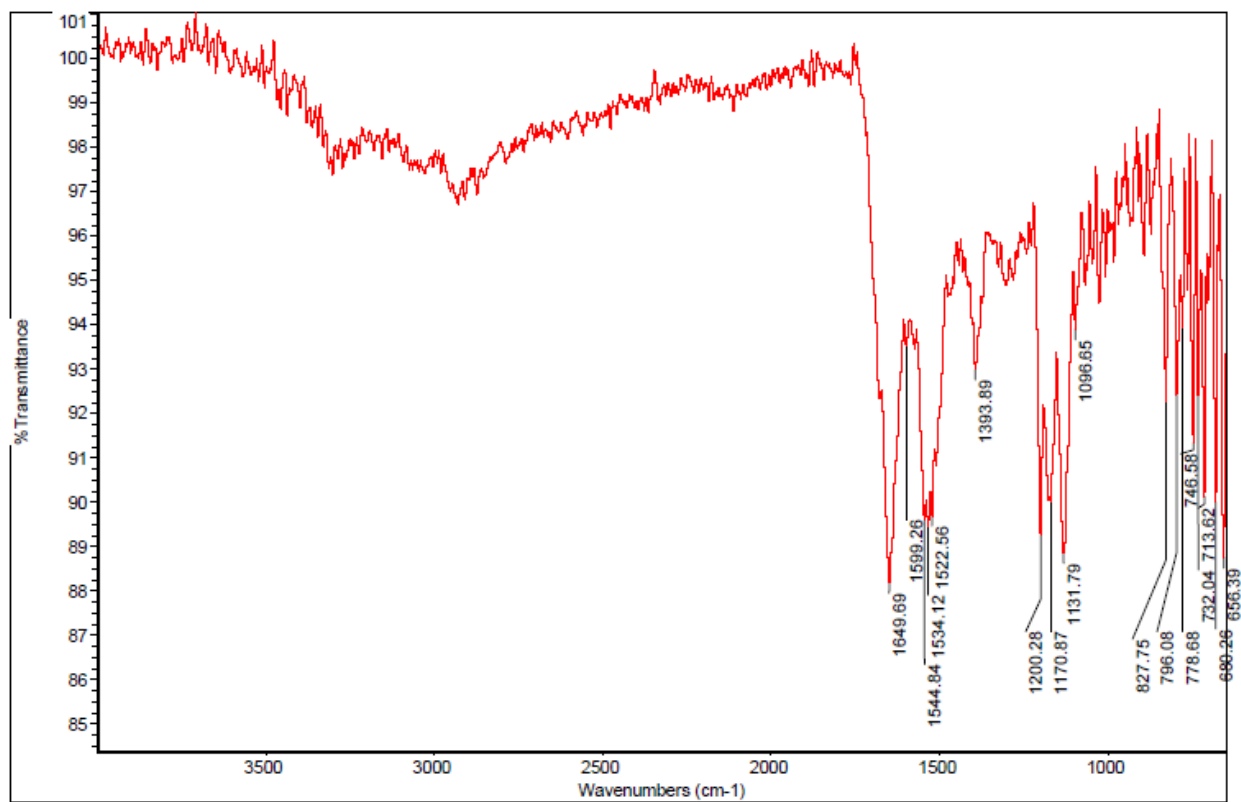


Figure C.4 FTIR of type D10K20 nanosponge before POH loading

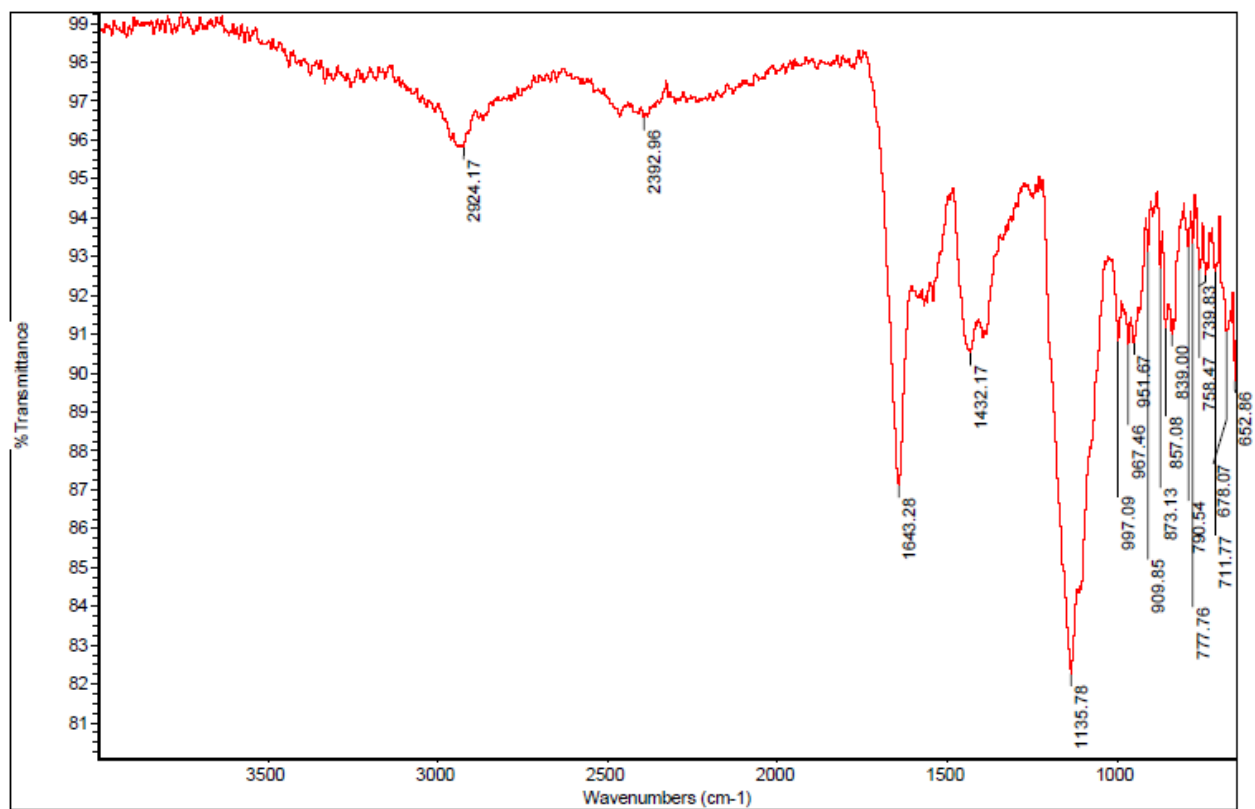


Figure C.5 FTIR of type D10K20 nanosponge after POH loading.

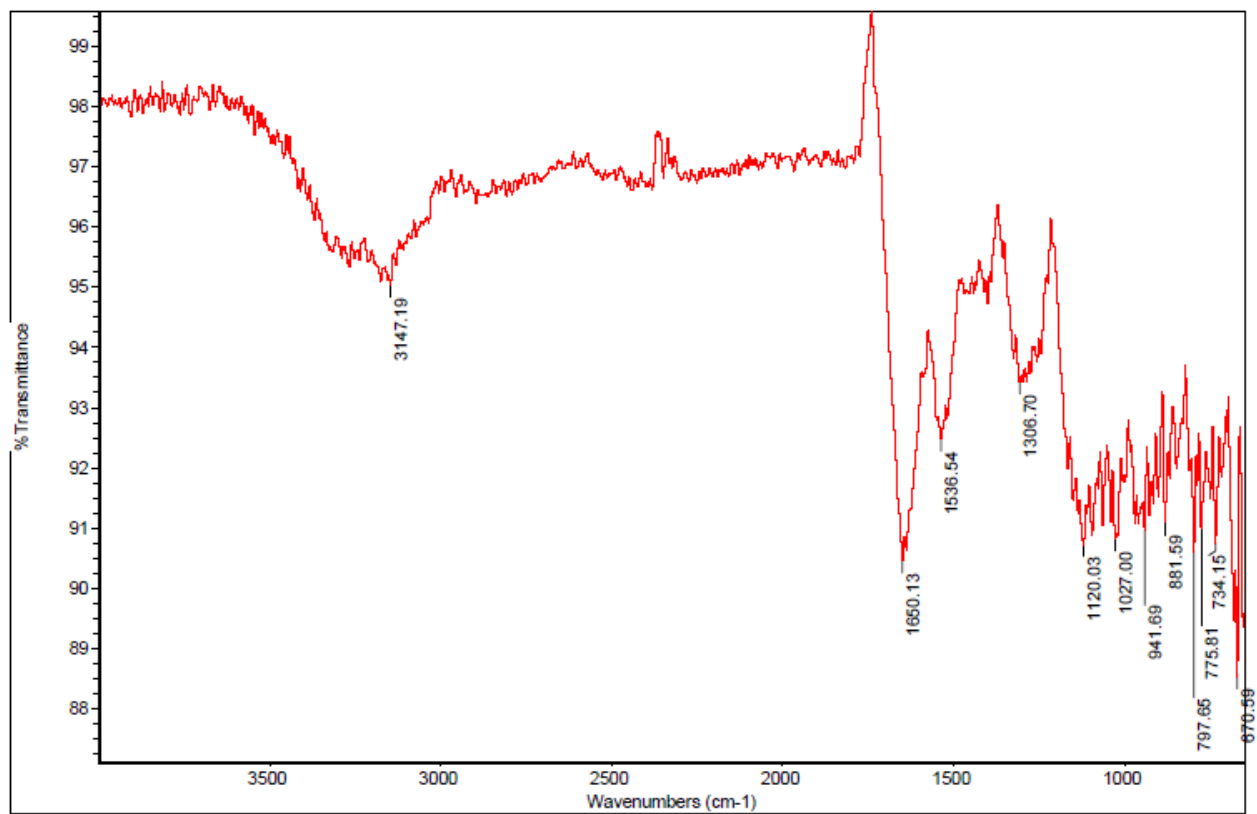


Figure C.6 FTIR of type D10R20 nanosponge before POH loading.

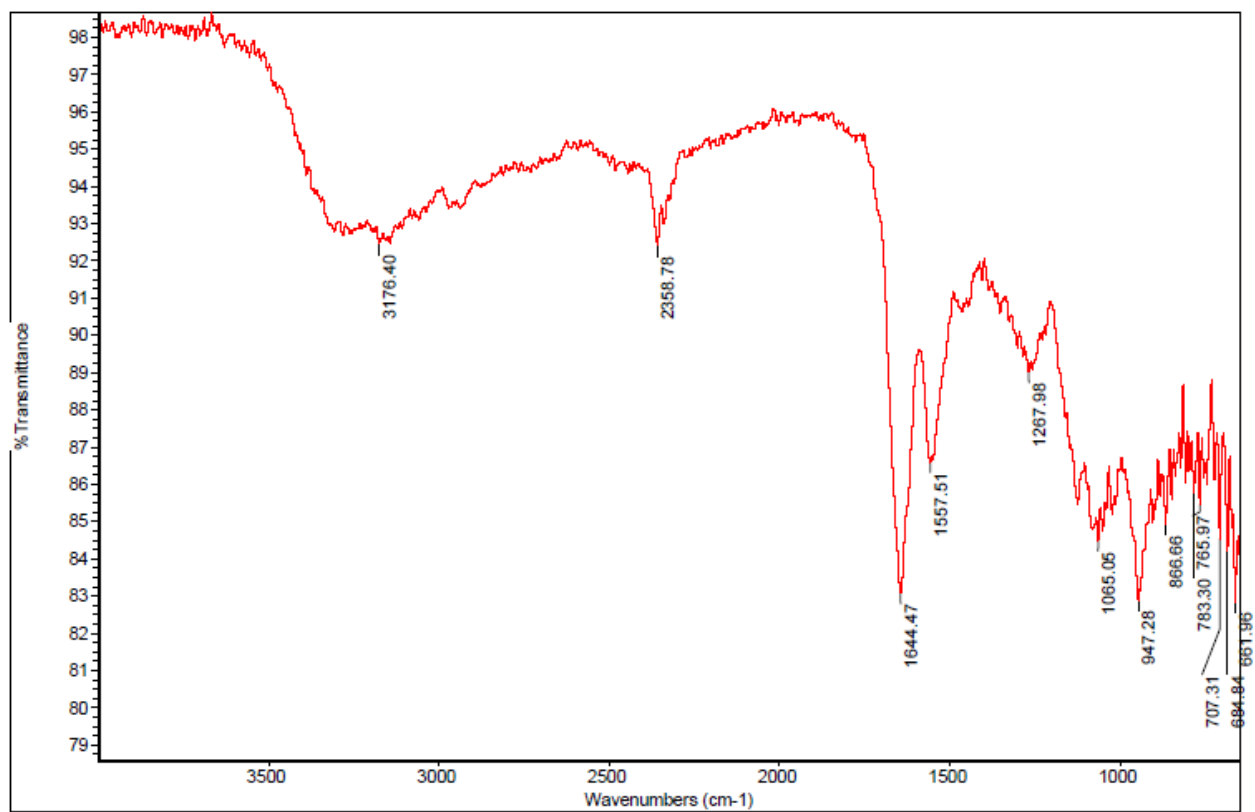


Figure C.7 FTIR of type D10R20 nanosponge after POH loading.

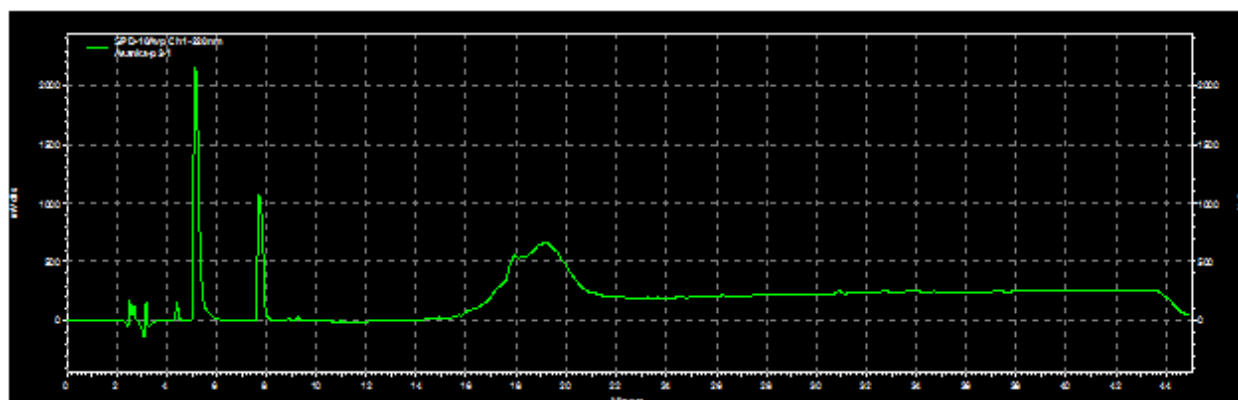
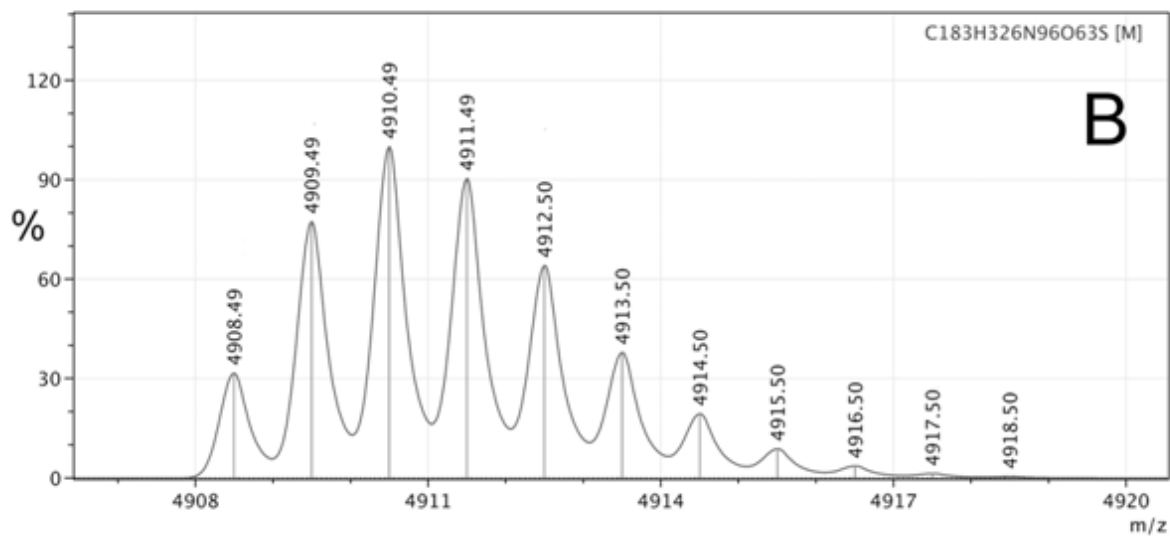
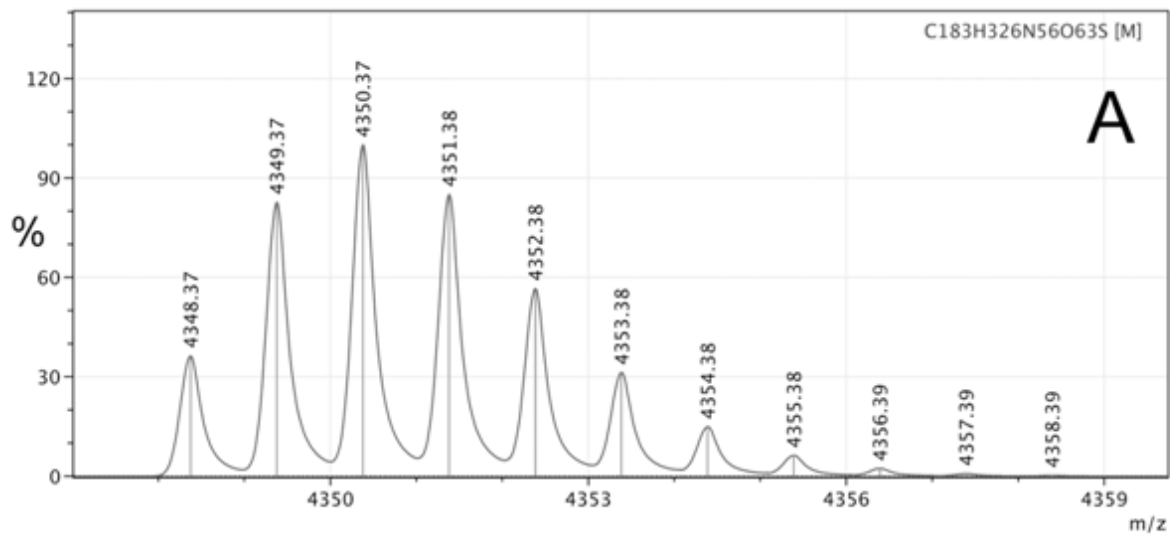
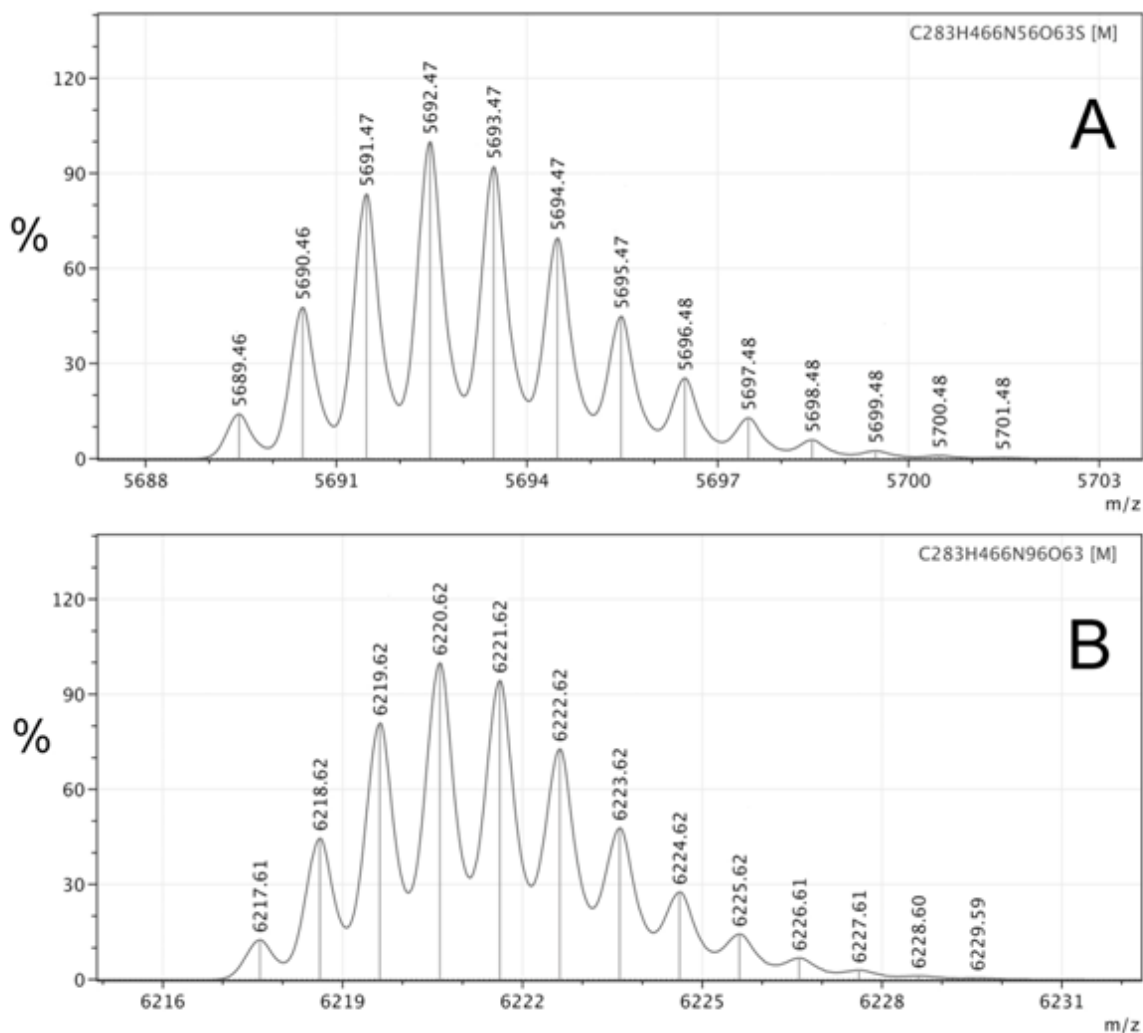


Figure C.8 HPLC of type D10K20 nanosponge



**Figure C.9 MALDI-TOF (Voyager DE STRT) of A: D<sub>10</sub>K<sub>20</sub>DEV DGC, the isotope distribution is consistent with the chemical formula C<sub>183</sub>H<sub>326</sub>N<sub>56</sub>O<sub>63</sub>S; B: D<sub>10</sub>R<sub>20</sub>DEV DGC the isotope distribution is consistent with the chemical formula C<sub>183</sub>H<sub>326</sub>N<sub>96</sub>O<sub>63</sub>S.**



**Figure C.10 MALDI-TOF (Voyager DE STRT) of A: (D-perillyl alcohol)<sub>10</sub>K<sub>20</sub>DEVDGC, the isotope distribution is consistent with the chemical formula C<sub>283</sub>H<sub>466</sub>N<sub>56</sub>O<sub>63</sub>S; B: (D-perillyl alcohol)<sub>10</sub>R<sub>20</sub>DEVDGC the isotope distribution is consistent with the chemical formula C<sub>183</sub>H<sub>466</sub>N<sub>96</sub>O<sub>63</sub>S. Note that MALDI-TOF does not indicate, to which of the 12 aspartic acid units the 10 perillyl alcohols are bound.**

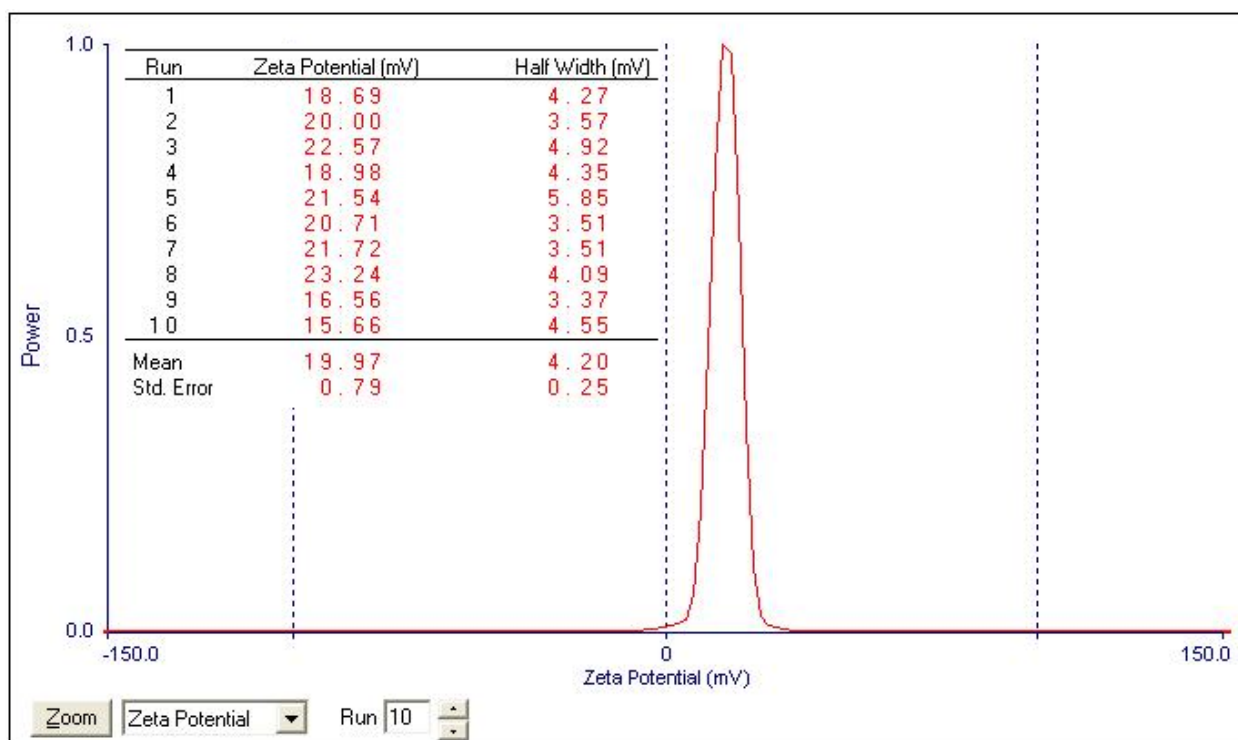


Figure C.11 Zeta potential of type (D-POH)<sub>10</sub>K<sub>20</sub> nanosponges in PBS

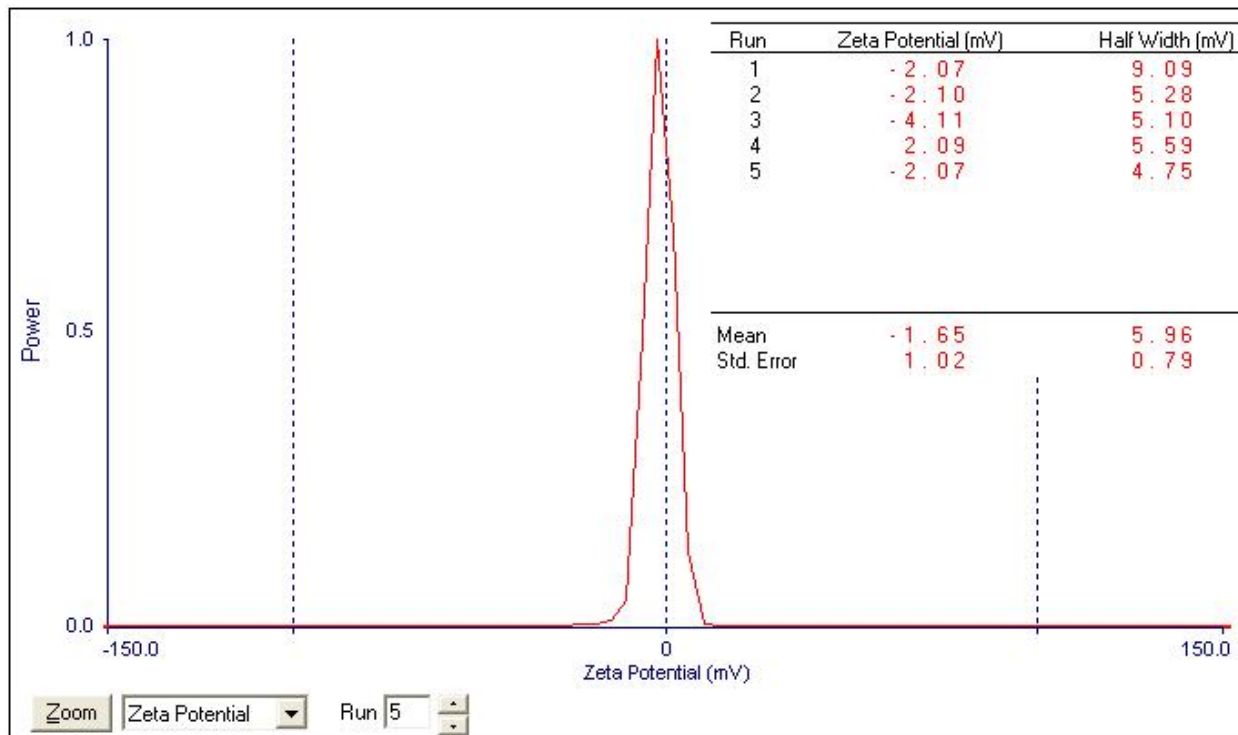


Figure C.12 Zeta potentials of type (D-POH)<sub>10</sub>R<sub>20</sub> nanosponges in PBS

### Procedure for Critical Micellar Concentration (CMC) Detection of (D-POH)<sub>10</sub>K<sub>20</sub>

Stock solution of 0.55 mM solution was prepared and 1.0  $\mu$ l from that solution was added into 1 ml of 1X PBS solution in a glass cuvette. Solution was incubated for 10 min at 37 °C and DLS was measured. Similarly 1 $\mu$ l aliquots of stock solution were added stepwise and DLS were recorded after 10 min incubation at 37 °C.

(D-POH) <sub>10</sub> K <sub>20</sub> volume added (0.55 mM, $\mu$ l)	Final volume (ml)	Final [(D-POH) <sub>10</sub> K <sub>20</sub> ] mM
1	1.001	0.000549451
2	1.002	0.001097804
3	1.003	0.001645065
4	1.004	0.002191235
5	1.005	0.002736318
6	1.006	0.003280318
7	1.007	0.003823237

**Table C.1 Volumes and concentrations of (D-POH)<sub>10</sub>K<sub>20</sub> nanosponge used for CMC detection**

### Procedure for Critical Micellar Concentration (CMC) Detection of (D-POH)<sub>10</sub>R<sub>20</sub>

Stock solution of 0.55 mM solution was prepared and 1.0  $\mu$ l from that solution was added into 1 ml of 1X PBS solution in a glass cuvette. Solution was incubated for 10 min at 37 °C and DLS was measured. Similarly 1 $\mu$ l aliquots of stock solution were added stepwise and DLS were recorded after 10 min incubation at 37 °C.

(D-POH) <sub>10</sub> R <sub>20</sub> volume added (2 mM, μl)	Final volume (ml)	Final [(D-POH) <sub>10</sub> R <sub>20</sub> ] mM
5	1.005	0.00995
10	1.01	0.019802
15	1.015	0.029557
20	1.02	0.039216
25	1.025	0.04878
30	1.03	0.058252
35	1.035	0.067633
40	1.04	0.076923
50	1.05	0.095238

**Table C.2 Volumes and concentrations of (D-POH)<sub>10</sub>R<sub>20</sub> nanosponge used for CMC detection**

**Control Experiment: Toxicity of Perillyl Alcohol, Type D10K20 Nanosponges, and Type D10R20 Nanosponges**

Result (as shown in Figure C.13): There is virtually no cytotoxicity of perillyl alcohol or nanosponges in the observed concentration range on GL26 cells. We have tested the highest concentrations of perillyl alcohol and nanosponges on NPCs as well. Again, there was virtually no effect (data not shown). Cell viability was measured by using the MTT assay, which is sensitive to cell proliferation.<sup>10</sup>

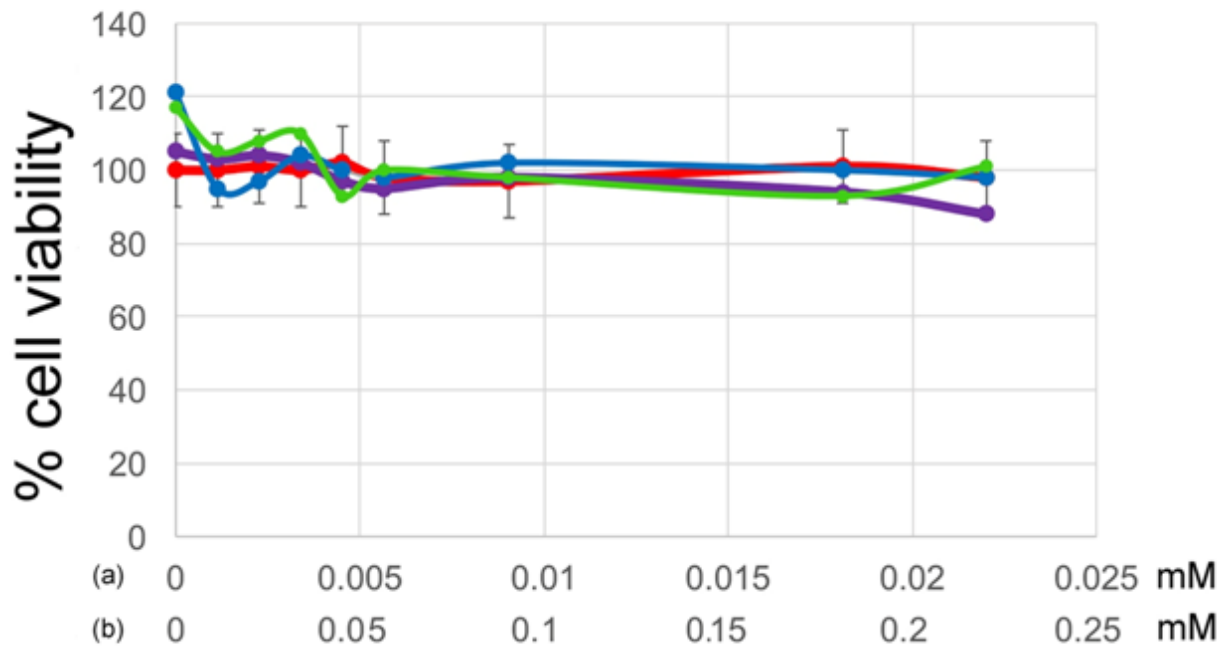


**Figure C.13 Control experiments: Cell viability of GL26 cells (cultured without serum) as a function of added perillyl alcohol (concentrations: a), type D10K20 nanosponge (concentrations: b), type D10R20 nanosponge (concentrations: b), and PBS control (concentrations: b)).**

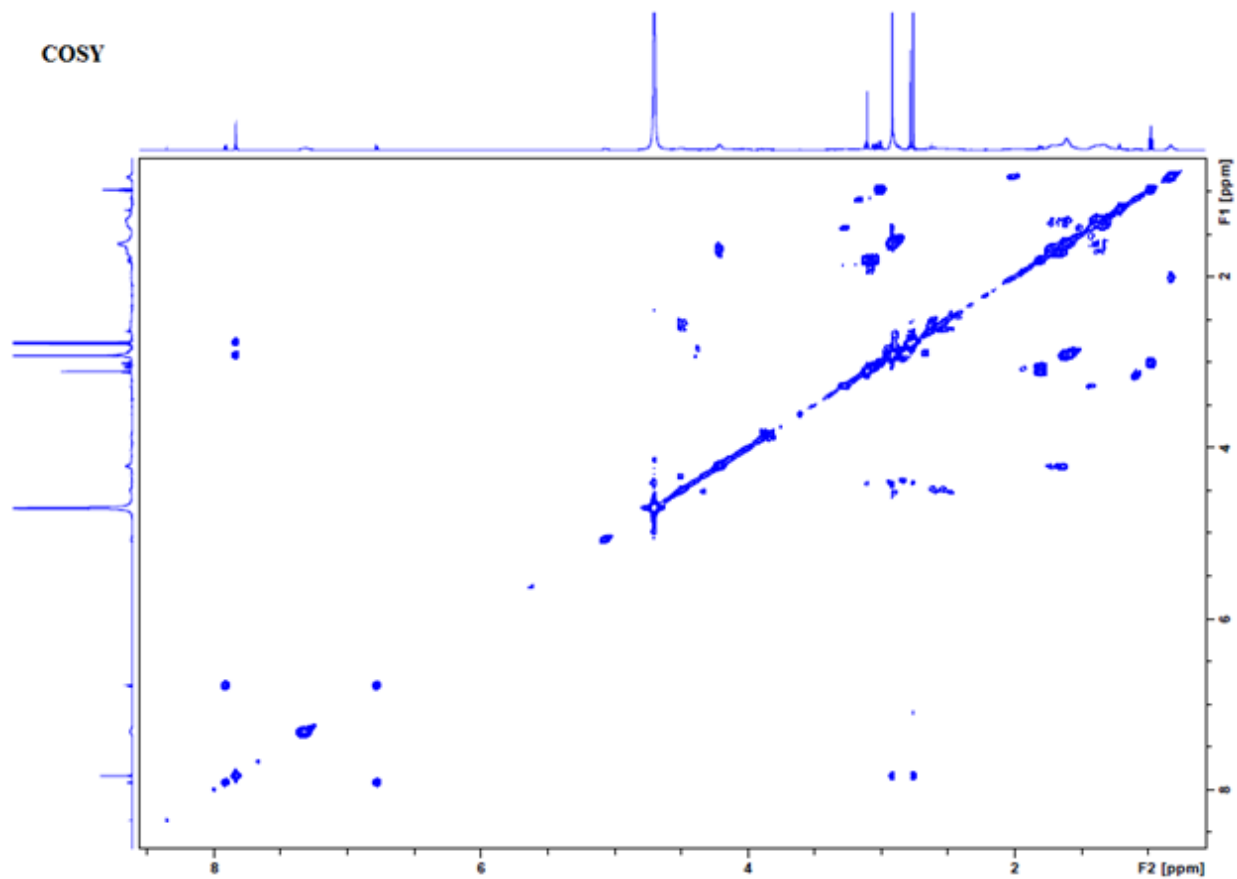


**Figure C.14** COSY (1H-1H correlated spectroscopy) of type (D-POH)<sub>10</sub>K<sub>20</sub> nanosponge (0.10 ml in D<sub>2</sub>O)

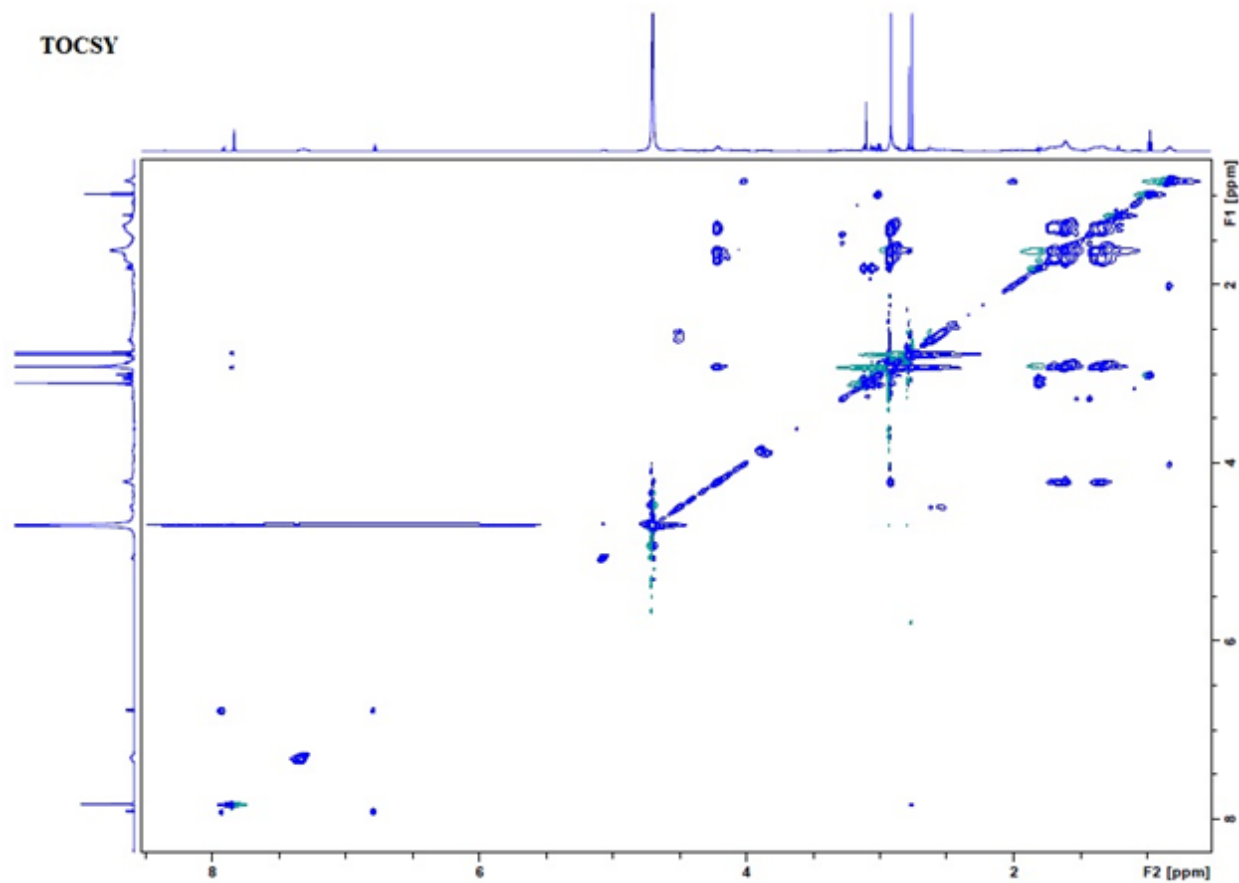


**Figure C.15** TOCSY (total correlated spectroscopy) of type (D-POH)<sub>10</sub>K<sub>20</sub> nanosponge (0.10 ml in D<sub>2</sub>O)

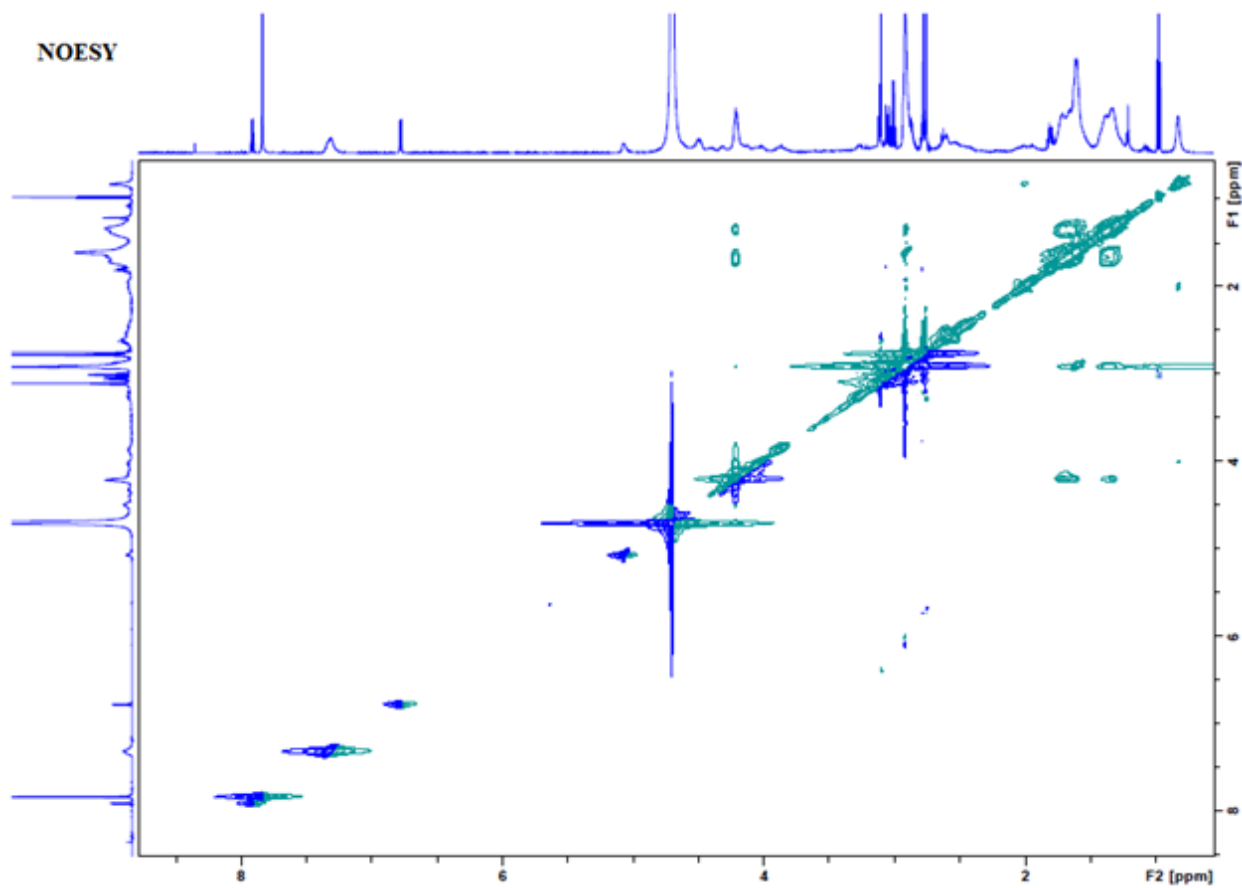


**Figure C.16** NOESY (2D Nuclear Overhauser spectroscopy) of type (D-POH)<sub>10</sub>K<sub>20</sub> nanosponge (0.10 ml in D<sub>2</sub>O)

## References

1. Amblard, M.; Fehrentz, J. A.; Martinez, J.; Subra, G., Methods and Protocols of modern solid phase peptide synthesis. *Mol Biotechnol* **2006**, *33* (3), 239-254.
2. Pronk, S.; Pall, S.; Schulz, R.; Larsson, P.; Bjelkmar, P.; Apostolov, R.; Shirts, M. R.; Smith, J. C.; Kasson, P. M.; van der Spoel, D.; Hess, B.; Lindahl, E., GROMACS 4.5: a high-throughput and highly parallel open source molecular simulation toolkit. *Bioinformatics* **2013**, *29* (7), 845-54.
3. Bussi, G.; Donadio, D.; Parrinello, M., Canonical sampling through velocity rescaling. *The Journal of Chemical Physics* **2007**, *126* (1), 014101.
4. Berendsen, H. J. C.; Postma, J. P. M.; van Gunsteren, W. F.; DiNola, A.; Haak, J. R., Molecular dynamics with coupling to an external bath. *The Journal of Chemical Physics* **1984**, *81* (8), 3684-3690.
5. Darden, T.; York, D.; Pedersen, L., Particle mesh Ewald: An N.log(N) method for Ewald sums in large systems. *J. Chem. Phys.* **1993**, *98* (12), 10089-10092.
6. Hess, B.; Bekker, H.; Berendsen, H. J. C.; Fraaije, J. G. E. M., LINCS: A linear constraint solver for molecular simulations. *J. Comput. Chem.* **1997**, *18* (12), 1463-1472.
7. Miyamoto, S.; Kollman, P. A., Settle: An analytical version of the SHAKE and RATTLE algorithm for rigid water models. *J. Comput. Chem.* **1992**, *13* (8), 952-962.
8. Parrinello, M.; Rahman, A., Polymorphic transitions in single crystals: A new molecular dynamics method. *Journal of Applied Physics* **1981**, *52* (12), 7182-7190.
9. Monticelli, L.; Kandasamy, S. K.; Periole, X.; Larson, R. G.; Tieleman, D. P.; Marrink, S.-J., The MARTINI Coarse-Grained Force Field: Extension to Proteins. *Journal of Chemical Theory and Computation* **2008**, *4* (5), 819-834.
10. Stockert, J. C.; Blazquez-Castro, A.; Canete, M.; Horobin, R. W.; Villanueva, A., MTT assay for cell viability: Intracellular localization of the formazan product is in lipid droplets. *Acta Histochem.* **2012**, *114* (8), 785-796.